Laser Brazing of Magnesium to Steel Sheet

by

Ali Mohamad Nasiri

A thesis
presented to the University of Waterloo
in fulfillment of the
thesis requirement for the degree of
Doctor of Philosophy
in
Mechanical Engineering

Waterloo, Ontario, Canada, 2013

AUTHOR'S DECLARATION

I hereby declare that I am the sole author of this thesis. This is a true copy of the thesis, including any required final revisions, as accepted by my examiners. I understand that my thesis may be made electronically available to the public.

Ali Mohamad Nasiri

ABSTRACT

The ability to effectively join magnesium alloys to steel will facilitate increased application and use of Mg alloys in the automotive and aerospace industries where joining Mg alloys to steel in order to achieve light weight, versatile and tailored properties in one composite part is highly desirable. The current thesis details (*i*) the development of a laser brazing technology for joining Mg alloy-interlayer-steel dissimilar metal combinations, (*ii*) thermochemical analysis of phases formed at the interface of a Mg alloy-steel joint during laser brazing, (*iii*) the bonding mechanisms in the Mg alloy-interlayer-steel joints using Al-12Si, Ni, and Sn interlayers, and (*iv*) the mechanism responsible for wetting of steel by molten Mg alloy during the laser brazing.

Firstly, a diode laser brazing procedure has been developed for joining AZ31B-H24 Mg alloy sheet to aluminum coated steel sheet using a AZ92 Mg alloy filler wire. The results of this study suggest that feasibility of this process depends strongly on the pre-existing Al-12Si coating layer on the steel sheet that promotes wetting of the AZ92 Mg alloy filler alloy as well as formation of a layer of θ-Fe$(Al,Si)_3$ interetallic compound along the fusion zone-steel interface. The average joint efficiency was 29% with respect to the AZ31B-H24 Mg alloy base metal. Failure occurred when cracks propagated along the intermetallic layer.

Secondly, to predict early stage phase formation in the Mg alloy-interlayer-steel system during the laser brazing process, the thermodynamic stability of precipitated phases at the Mg alloy-Ni-steel interface during laser brazing has been evaluated using FactSage thermochemical software. Assuming local chemical equilibrium at the interface, the chemical activity-temperature-composition relationships of intermetallic compounds that might form in the AZ92 magnesium alloy-Ni-steel system in the temperature range of 600-1100 °C were estimated. The addition of a Ni interlayer between the steel and the Mg brazing alloy was predicted to result in the formation of the AlNi, Mg_2Ni, and Al_3Ni_2 intermetallic compounds at the interface depending on the local maximum temperature. This was confirmed experimentally by laser brazing of AZ31B-H24 magnesium alloy and steel sheet with a micro-layer of electro-deposited Ni using AZ92 magnesium alloy filler wire. Bonding

between the magnesium alloy and the steel was facilitated by the formation of a transition layer composed of a solid solution of Ni in Fe on the steel followed by a layer of α-Mg + Mg_2Ni eutectic. A band of AlNi with different morphologies also formed along the fusion zone-steel interface, but was not directly responsible for bonding. The average joint efficiency was 56.5% with respect to the AZ31B-H24 Mg alloy base metal and 94.8% higher than that of laser brazed joint using Al-12Si interlayer.

Thirdly, to study a low melting point temperature interlayer element, the brazeability of AZ31B-H24 magnesium alloy sheet to Sn-coated steel sheet has been investigated. All tensile-shear specimens fractured in the steel base metal well away from the brazed joint. The results showed that while the Sn coating promoted good wetting between the molten filler alloy and the steel sheet, it did not play a role in forming the final bond. Its primary function appeared to be in maintaining a clean, oxide-free steel surface until the molten Mg filler alloy could come in direct contact with the steel surface. Bonding between the magnesium alloy and the steel was facilitated by the formation of two nano-scale transition layers composed of Fe(Al) solid solution on the steel followed by a layer of Al_8Mn_5 phase on top of Fe(Al) in the fusion zone along the interface. High resolution-TEM analysis showed that an orientation relationships (OR) with low angle of rotation of the matching planes and low interplanar mismatch existed at the Fe(Al)-$Al_8(Mn,Fe)_5$ interface. This was found to be responsible for the low interfacial energy density, good wetting and strong interfacial bond observed in this complex dissimilar metal system.

Finally, wetting has been characterized by measuring the contact angles of AZ92 Mg alloy on Ni electro-plated steel as a function of measured peak temperature reached during laser heating. Reactions between molten Mg and Ni led to a contact angle of about 86º in the peak temperature range of 618-750 ºC (denoted as Mode I) and a dramatic decrease to about 46º in the temperature range of 824-1020 ºC (denoted as Mode II). Scanning and transmission electron microscopy (SEM and TEM) indicated that AlNi + Mg_2Ni reaction products were produced between Mg and steel (Mg-AlNi-Mg_2Ni-Ni-Fe) in Mode I, and just AlNi between Mg and steel (Mg-AlNi-Fe) in Mode II. From high resolution TEM analysis, the measured interplanar mismatches for different formed interfaces in Modes I and II were

17% $_{\{Mg\text{-}AlNi\}}$-104% $_{\{AlNi\text{-}Mg2Ni\}}$-114% $_{\{Mg2Ni\text{-}Ni\}}$ and 18% $_{\{Mg\text{-}AlNi\}}$-5% $_{\{AlNi\text{-}Fe\}}$, respectively. Therefore, it is suggested that the poor wettability in Mode I was caused by the existence of Mg_2Ni since AlNi was the immediate layer contacting molten Mg in both Modes I and II and the presence of Mg_2Ni increases the interfacial strain energy of the system. This study has clearly demonstrated that the lattice mismatching at the interfaces between reaction product(s) and substrate, which are not in direct contact with the liquid, can greatly influence the wetting of the liquid.

ACKNOWLEDGEMENTS

I would like to sincerely thank my supervisors, Profs. Norman Zhou, David Weckman and Patrice Chartrand. I would also like to thank my friends who have supported me throughout the years, especially the members of the Centre for Advanced Materials Joining (CAMJ).

This work has been supported by the American Welding Society (AWS) Graduate Fellowship program and Magnesium Network of Canada (MagNET) supported by the Natural Sciences and Engineering Research Council of Canada (NSERC).

DEDICATION

To My Loving Wife Parisa

&

My Wonderful and Loving family

TABLE OF CONTENTS

LIST OF FIGURES

LIST OF TABLES

Chapter 1
INTRODUCTION

1.1 Background

Automotive manufacturers are coming under increasing regulatory pressure to improve the overall fleet mileage of their automobiles. This has created a need to develop and assess new advanced materials and manufacturing technologies that will allow fabrication of lighter weight automotive bodies and structural components thereby increasing fuel efficiencies and lowering environmental impact of vehicles. While magnesium alloys, with their combination of low density and high specific tensile strengths, could potentially be used to advantage to reduce the overall weight of a vehicle [1,2,3], sheet steels remain the most commonly used material in the automotive industry, due to their consistent properties, excellent ductility, and their lower material and fabrication costs [4]. Thus, the ability to make hybrid structures of magnesium alloy and steel sheet would facilitate the increased use of magnesium alloys and light-weighting of automotive structures. This will require the development of new techniques and processes that can be used to make reliable and low cost dissimilar metal joints between magnesium alloy and steel sheet [5,6,7,8].

It is difficult to join magnesium alloys directly to steel by conventional fusion welding technologies due to the large difference in their melting temperatures and the nearly zero solubility of magnesium and iron [7,8]. The melting point of steel (≈ 1550 °C) is well above the boiling point of magnesium (1107 °C), and this can cause catastrophic vaporization of the molten magnesium during a fusion welding process. In addition, the maximum solid solubility of Fe in Mg is 0.00041 at.% Fe [7]. There is also clear evidence that magnesium and steel do not react with each other and do not mix in the liquid state at ambient pressure [8]. Thus, metallurgical bonding between these two metals will only be possible provided another element that can interact and bond with both of them can be applied between the Mg and Fe as an intermediate interlayer element or alloy.

The existence of intermetallic phases or solid solutions between Mg and the interlayer and also the interlayer and Fe is an indication that metallurgical bonding between Mg and Fe

using the interlayer may be possible. Intermetallic compounds are solid phases containing two or more metallic elements, with one or more non-metallic elements, whose crystal structure differs from that of the other constituents. They are generally hard and brittle [9]. Formation of thick, brittle intermetallic compounds along the interface between Mg and steel can cause significant deterioration of mechanical properties. Therefore, when choosing the joining process that will be used, minimization of the thickness of any brittle intermetallic compounds that might form along the interfaces of the Mg alloy-interlayer-steel joint and also minimization of intermixing between the Mg and Fe in the liquid-state are the main factors that must be considered. If melting of the steel and intermixing with liquid Mg occur during the welding process, weld cracking and porosity formation are inevitable at the interface due to the rapid vaporization of the magnesium and lack of solubility of magnesium and steel [9].

Brazing of metals differs from fusion welding in that brazing temperatures are generally lower than the melting points of the base metals. For this reason, brazing can be a superior choice in joining dissimilar metals, such as magnesium and steel. In addition, very fast heating and cooling rates can be applied during the brazing process to minimize the thickness of intermetallic compounds that might form along the interfaces [10].

The benefits of using laser brazing and laser welding-brazing technologies for joining dissimilar materials are becoming increasingly recognized due to the combined attributes of furnace brazing and laser welding [11]. With a more localized energy input and more precise control of the laser beam energy, high joining speeds and accompanying high cooling rates can be realized with minimal heating of the parts. Also, laser brazing and laser welding-brazing can prevent or minimize excessive formation of detrimental intermetallic phases. If intermetallic layers can be limited to thicknesses below 10 μm, acceptable joint strengths and mechanical properties may be obtained [9,12].

The CO_2 laser and Nd:YAG laser have been widely used for welding and cutting, but high power diode lasers are normally used for metal brazing due to their short wavelength, high absorptivity in metals, and uniform beam intensity [9]. The lower intensity diode laser beam can be used to provide controlled heating without melting the steel [9]. In this process,

the filler wire and surface of the Mg alloy base material are melted simultaneously by the high power diode laser, while the steel remains unmelted.

As there is a desire in the automotive and aerospace industries to join Mg alloy to steel in order to achieve lighter weight, versatile and tailored properties in one composite part, development of a laser brazing technology for joining of steel-interlayer-Mg alloy combinations with a strong metallurgical bond between the steel and Mg alloy will expedite increased application and use of Mg alloys in these industries.

1.2 Objectives

The aim of the current work is to conduct an experimental and theoretical study of the brazeability of magnesium-steel dissimilar metal joints using the laser brazing process. The main objectives of this research are as follows:

1. To develop a laser brazing technology for joining Mg alloy-interlayer-steel dissimilar metal combinations.
2. To predict early stage phase formation in the Mg alloy-interlayer-steel system during the laser brazing process. Formation of any phases along the interface between the magnesium alloy and steel can affect not only the wettability of the steel by molten magnesium, but also bonding between these two metals.
3. To study bonding mechanisms in the Mg alloy-interlayer-steel joints and identify the key factors responsible for formation of a metallurgical bond between the magnesium and steel.
4. To understand the fundamental mechanisms and reaction characteristics at play during the reactive wetting of steels by molten magnesium alloys.

1.3 Organization of the Thesis

This thesis is subdivided into eight chapters. Chapter 2 provides some background information on the motivation for joining Mg alloys to steels based on the properties of the Mg alloys and also previously used joining processes for Mg alloy-steel dissimilar metal

combination. In particular, the factors affecting the joint strength are detailed. It also provides the reader with some fundamental understanding of the wetting in metallic-metallic systems.

Chapter 3 provides details on experimental methods and conditions used throughout this study including materials, test equipment and procedures.

Chapter 4 reports the microstructure and mechanical properties of laser brazed AZ31B Mg alloy to steel using an Al-12Si interlayer. It shows the microstructural analysis results of the fusion zone, steel-fusion zone interface, and also the mechanical performance of the joints.

Chapter 5 describes thermochemical analysis of phases formed at the interface of a Mg alloy-Ni plated steel joint during laser brazing. The results provided better understanding of the phases that might form at the interface of the dissimilar metal joints during the laser brazing process. This chapter also documents investigations on the interfacial microstructure and mechanical properties of diode laser brazed AZ31B magnesium to steel sheet using a Nickel interlayer. More specifically, the macro- and microstructure, element distribution, and interfacial phases of the joints were studied by optical microscopy (OM), scanning electron microscopy (SEM), transmission electron microscopy (TEM), and X-ray diffraction (XRD). The results enabled a correlation between the thermochemical (temperature and composition) properties of the system and the observed interfacial microstructure of the Mg alloy-Ni plated steel joint.

Chapter 6 contains the study on the interfacial microstructure and mechanical properties of the diode laser brazed AZ31B magnesium to steel sheet, when a Sn interlayer was used.

Chapter 7 describes the mechanism responsible for wetting of the Ni-plated steel by molten magnesium alloy. In particular, the effects of interfacial reaction products and lattice mismatching on wettability are discussed.

Finally, Chapter 8 lists the conclusions and provides recommendations for future research.

Chapter 2
LITERATURE REVIEW

2.1 Motivation

In order to achieve further reductions in the weight of the automotive body, efforts are being made in the field of car design to replace structural elements with magnesium components [13]. The increased integration of Mg components into vehicle structures will be facilitated by development of new techniques for joining Mg alloys and dissimilar metal combinations, such as Mg to steel. Figure 2-1 shows a few examples from the past where magnesium sheet has been used successfully for complex structural applications in different fields of transportation, *e.g.*, cars, trucks, aeroplanes, or satellites [14]. As early as the late 1930s, a small-series bus completely constructed out of magnesium extrusions and sheet metal of Mg-Mn alloy was reported [15]. Car body applications have demonstrated the outstanding design potential of magnesium sheet. For example, the ultra-light magnesium sheet metal construction of an early French sports car weighted only 64 kg [14]. Mercedes also used body components for their competition racing cars in the 1950s [13]. Another premier application has been deep drawn Samsonite suitcase sides formed from 1.0 mm AZ31B magnesium alloy sheet [13].

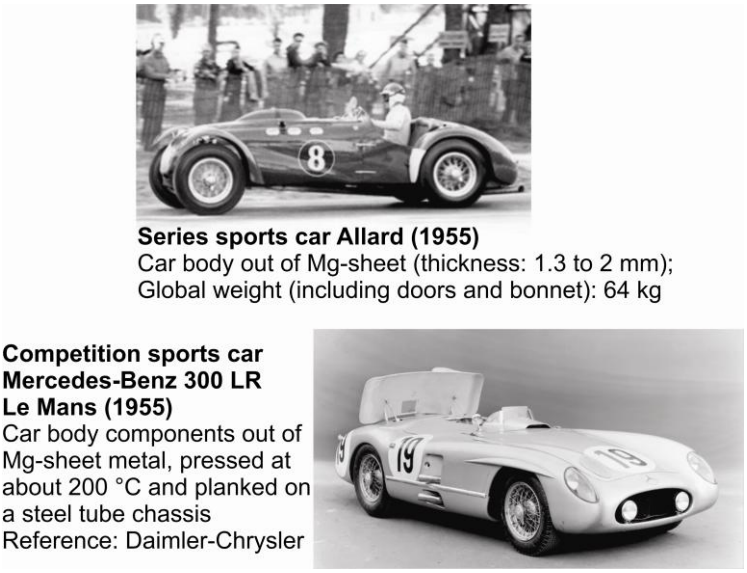

Figure 2-1: Structural applications of Mg-sheet for transportation [14].

Potential applications of magnesium alloys in an automobile are shown in Figure 2-2. These include the interior (*e.g.*, bracket carrier, seat components); the body (large hang-on parts like doors, roof, bonnets, as well as body-in-white and front end parts); the drive system (cylinder head cover, oil pan), as well as the chassis (*e.g.*, wheels) [14]. It is expected that development of new technologies for joining of Mg alloy-steel combinations with a strong metallurgical bond between them will facilitate increased application and use of Mg alloys in the automotive industry.

Figure 2-2: Magnesium sheet has been used in the VW-Lupo for automotive lightweight construction [14].

2.2 Weldability of Magnesium Alloys

Magnesium puts high demands on the welding process because of its physical properties. Magnesium alloys can have a relatively large freezing range of about 420 to 620 °C. Thus, there is considerable risk of hot-cracking during any fusion welding process [15]. A comparison between the physical properties of pure magnesium, aluminum and iron is shown in Table 2-1 [16,17,18,19]. Magnesium alloys show inherent characteristics, such as strong tendency to oxidize, low absorptivity of laser beams, high thermal conductivities, high coefficients of thermal expansion, low melting and boiling temperatures, wide solidification

temperature ranges, high solidification shrinkage, a tendency to form low melting-point constituents, low viscosity, low surface tensions, high solubility for hydrogen in the liquid state, and absence of a color change at the melting point temperature [15].

Table 2-1: Properties of pure magnesium, aluminum, and iron (taken from [16-19]).

Properties	Magnesium	Aluminum	Iron
Ionization energy (eV)	7.6	6	7.8
Specific heat ($Jkg^{-1}K^{-1}$)	1360	1080	795
Specific heat of fusion (J/kg)	3.7×10^{5}	4×10^{5}	2.7×10^{5}
Melting point (˚C)	650	660	1536
Boiling point (˚C)	1090	2520	2860
Viscosity ($kgm^{-1}s^{-1}$)	0.00125	0.0013	0.0055
Surface tension (Nm^{-1})	0.559	0.914	1.872
Thermal conductivity ($Wm^{-1}k^{-1}$)	78	94.03	38
Thermal diffusivity ($m^{2}s^{-1}$)	3.73×10^{-5}	3.65×10^{-5}	6.80×10^{-5}
Coefficient of thermal expansion (K^{-1})	25×10^{-6}	24×10^{-6}	10×10^{-6}
Density (kgm^{-3})	1590	2385	7015
Elastic modulus (N/m^{3})	4.47×10^{10}	7.06×10^{10}	21×10^{10}
Electrical resistivity (μΩm)	0.274	0.2425	1.386
Vapour pressure (Pa)	360	10^{-6}	2.3

Compared with aluminum alloys, some important differences exist so that it is not always possible to transfer procedures for welding aluminum alloys directly to the welding of magnesium alloys. For example, magnesium only requires 60% of the energy needed to melt the same volume of aluminum [15]. The energy required for welding is reduced to 1/3 because of the lower thermal conductivity of magnesium. Furthermore, magnesium alloys have only half the vaporization temperature of aluminum, that is, about 1100 °C [15]. The vapour pressure of Mg in the relevant temperature interval for welding is 3 to 4 orders of magnitude higher than that of aluminum [15]. The low vaporization temperature and very high vapour pressure of magnesium compared with aluminum can result in excessive vaporization rates and spatter formation when welding Mg alloys [17].

As a consequence of the high thermal expansion coefficient (25×10^{-6} K^{-1}) of Mg, which is more than twice that of mild steel and still 10% higher than that of aluminum alloys, one

has to consider high welding distortion and clamping forces [15]. The electrical conductivity is similar to mild steel and so the use of resistance welding for magnesium alloys is possible [14].

2.3 Brazing of Magnesium Alloys

The increased use of magnesium alloys in the 1990s caused new interest in brazing magnesium and its alloys. Before that, furnace, torch and dip brazing processes have been used successfully without significant changes [10]. Increased production of magnesium and its applications in the last few decades, especially for new high-performance magnesium alloys, have created technical and scientific challenges for the brazing community [10].

High temperature brazing processes reduce the properties of work-hardened magnesium alloys to the annealed levels. As an example, the extruded and tempered AZ31B -F magnesium alloy after brazing at 595 ˚C for 1-2 min, loses about 8% tensile strength, 22% yield strength, and its elongation increases 35% [16]. This reduction of strength during torch brazing happens locally in areas heated for brazing, whereas furnace and dip brazing cause the reduction of properties of the entire brazement. This significant loss of properties during conventional brazing processes is the main motivation for developing new brazing processes with localized energy input and very fast heating and cooling, and also low-melting temperature brazing filler metals.

2.3.1 Filler Metals

Commercially available filler wires for brazing magnesium alloys are: BMg-1 (AZ92A), BMg-2a (AZ125), and MC3 alloy [20]. All of these alloys can be used for torch, furnace and dip brazing [20]. Table 2-2 shows the nominal composition and physical properties of these alloys. The standard filler metal MC3 is more commonly used in Japan and has a composition close to BMg-1 [20].

Table 2-2: Composition and physical properties of commercial brazing filler metals [21].

Designation		Nominal Composition (wt.%) (Balance Mg)				Temperatures (ºC)		
AWS	A5.8 ASTM	Al	Zn	Mn	Cu	Solidus	Liquidus	Brazing Range (Recommended)
B-Mg1	AZ92A	8.3-9.7	1.7-2.3	0.15-0.5	0.05	443	599	502-616
B-Mg-2a	AZ125A	11-13	4.5-5.5	---	---	410	565	570-595
MC3	---	8.3-9.7	1.6-2.4	0-0.1	0-0.25	443	599	605-615

Alloying elements, such as Al, Zn, Mn, Be, Si, Zr, Ca, Ag, Th, Y, and rare earth elements are used in magnesium filler metals. Aluminum enhances room temperature strength and hardness and also fluidity of the alloy, but excessive aluminum causes increased formation of brittle intermetallic phases in the fusion zone and as a result, ductility of the joint decreases [21]. Also, the solidification range of the alloy increases with increasing Al content of the filler metal [21]. This increases the propensity for solidification cracking [21].

Zn improves fluidity and increases strength of magnesium alloys due to solid-solution strengthening. Corrosion caused by Fe or Ni impurities in magnesium alloys can be prevented by adding Zn. However, when the content of Zn in the filler metal is more than 2 wt.%, hot cracking can occur [21]. Zinc may not cause hot cracking problems in combination with aluminum and manganese. For example, the cast alloy AZ88, which contains 8 wt.% Al, 8 wt.% Zn, and 0.2 wt.% Mn exhibits good resistance to hot cracking [22]. Low manganese content (< 0.2 wt.%) increases corrosion resistance of magnesium alloys, especially in saltwater, but it does not affect mechanical properties [21]. Beryllium is added to magnesium alloys in amounts < 0.002 wt.% in order to decrease excessive oxidation of molten metal and to reduce the risk of ignition during torch brazing [10].

Masuda *et al*. [23] studied simple binary Mg-Zn and Al-Zn systems as brazing filler metals for AZ91A cast magnesium alloy in argon. All binary Mg-Zn filler metals showed poor spreading behaviour along the base metal surface for brazing times from 0 to 110 min and a brazing temperature range of 300-550 ˚C. The strength of these brazed joints was not

reported. It is doubtful Mg-Zn binary systems are suitable as brazing filler metals for magnesium alloys due to susceptibility of Mg-Zn alloys to hot cracking.

Silicon not only improves fluidity of magnesium alloys, but also increases the creep strength due to formation of the Mg_2Si phase in some alloys, such as AS21 and AS41 [24]. However, corrosion resistance of magnesium alloys decreases by adding silicon in the presence of iron impurities [24].

Silver improves the strength for both cast and wrought magnesium alloys due to age hardening [21]. Addition of rare-earth metal elements produces stable grain boundary precipitates and the result is improvement of creep resistance [21]. Zirconium is also an effective grain refiner for magnesium alloy, but it should not be used in alloys containing both Al and Mn, because they form an intermetallic with Zr and remove it from solid solution [21].

The elements Si, Ge, Pb, Sb, and Bi from IVA and VA element groups form stable intermetallic phases with magnesium [24]. These elements can be added to Mg-Al based filler metals for precipitation strengthening.

Erosion of the base metal during brazing occurs for all of the Mg alloy filler metals, especially those with aluminum content more than 9 wt.%. Therefore, those filler metals are not suitable for joining thin-wall structures [21].

Based on the previous discussion, the BMg-1 filler metal alloy is most likely to be a good candidate for a filler metal for laser brazing of AZ31B-Mg alloy sheet to steel sheet. With 9 wt.% Al, it has improved strength, hardness, and fluidity of the Mg alloy without excessive erosion of the base metals, the 2 wt.% Zn provides solid-solution strengthening without risk of hot cracking and the 0.2 wt.% Mn increases the corrosion resistance of the Mg alloy.

2.3.2 Fluxes

Fluxes promote formation of brazed joints. They may be used to surround the work, exclude reactants, and provide active or inert protective atmospheres, thus preventing undesirable

reactions during brazing. For some materials, such as Mg alloys, fluxes may also reduce oxides that are present. Flux must be capable of dissolving any oxide remaining on the base metal after it has been cleaned, and any oxide films on the liquid filler metal [25].

Fluxes are classified according to their performance on certain groups of base metals in rather specific temperature ranges. For successful use, a flux must be chemically compatible with all base metals and filler metals involved in the brazement. It must be active across the entire brazing temperature range and throughout the time at brazing temperature [25].

Fluxes for brazing of magnesium alloys are normally based on halide salts of alkali- and alkali-earth metals with LiCl and/or NaF as active components [20,26]. Type FB2-A (ANSI/AWS A5.31-92) is used for brazing of magnesium alloys [20]. These fluxes are corrosive, which is why complete removal of the flux after brazing is vital to achieve good corrosion resistance of the brazed parts [20,26]. Also, these fluxes must be completely dried before the brazing process in order to prevent formation of magnesium hydroxide on the brazed surface. Therefore, these fluxes must be used in the form of a paste with an alcohol binder for torch brazing or dry powder form for furnace brazing [20].

2.3.3 Surface Preparation before Brazing

The Mg components to be brazed should be completely clean and free from oil, dirt, oxide layer and chromate coating [20]. Alkaline cleaning baths can be used for degreasing of specimens and surface films, such as oxide or chromate conversion coating, should be removed by mechanical or chemical cleaning prior to the brazing process [21].

Abrading with aluminum oxide cloth or steel wool or stainless steel wire brushing can be used for mechanical cleaning. Chemical cleaning involves a 5-10 min. dip in a hot alkaline cleaner followed by a 2 min. dip in a ferric nitrate bright pickle solution [20,21].

2.4 Joining Steel to Magnesium

Review of the literature reveals that a successful joint between Mg and Fe may be made by inserting a third metal at the interface. Different joining processes have been used to joint Mg

alloys to steel sheets [27-29,33-39], but the key factor for getting a metallurgical bond between Mg and steel in all of those studies was the use of an interlayer. In this section, different joining processes used for Mg-steel dissimilar joints are discussed.

2.4.1 Friction Stir Welding (FSW)

Friction stir welding (FSW) has been shown to have the ability to join Mg alloys to steel [27,28,29]. FSW is a solid-state welding technique invented by Thomas *et al*. [30] at The Welding Institute (TWI). FSW has the added advantage of minimal oxidation because of the solid-state nature of the process.

Chen and Nakata [27,28] studied the effect of tool geometry on microstructure and mechanical properties of friction stir lap-welded AZ31 Mg alloy and steel. A schematic of the FSW process is shown in Figure 2-3 [27]. The magnesium alloy sheet was put on the steel sheet and a rotating tool with a 1.5 mm long probe was inserted into the magnesium and steel sheets moving along the joint line. Based on their results, the AZ31/zinc coated steel joints showed higher failure loads than the AZ31/brushed finished steel joints, which suggested that the presence of the zinc coating significantly improved the weldability of magnesium alloy and steel [28]. However, poor mechanical properties of the joints were observed due to oxidation of the interfacial zone between the steel and magnesium alloy sheets and also formation of brittle intermetallic compounds, such as Fe_4Al_3, along the interface [27]. Fracture of tensile shear test specimens was reported to occur always along the Mg alloy-steel interface, not in the stir zone (SZ) [27].

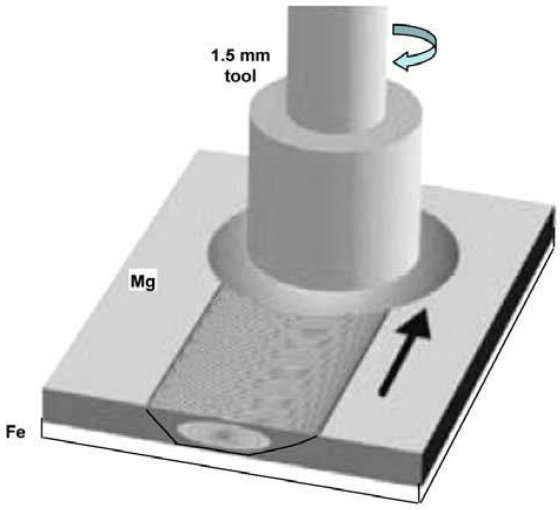

Figure 2-3: A schematic of the FSW process (taken from Chen and Nakata [27]).

A similar study of FSW of AZ31 Mg alloy to steel in a lap configuration was carried out by Jana *et al*. [29] based on the idea that a successful joint between Mg and Fe may be made by keeping a third metal such as Zn at the interface. They used two types of steel sheets, *e.g.*, hot-dipped galvanized (HDG) high strength steel and electro-galvanized mild steel [29]. However, neither the original Zn layer nor any new phases were observed along the bulk of the joint interface [29]. In general, the absence of any new Zn-Mg phase along the Mg-steel interface indicated that the top Zn layer did not act as a brazing material [29]. Also, failure of all joints was reported to occur through interfacial separation and all the joints were found to be mechanical in nature, since the Mg-steel bonded interface was mostly free from any new phases [29]. Therefore, even with the existence of a third metal as the interlayer, such as Zn in the form of zinc coated steel, keeping the interlayer at the interface between steel and magnesium alloy is very difficult during FSW, due to the stirring action of the pin and material flow with high plasticity along the interface.

2.4.2 Diffusion Brazing

Diffusion brazing methods have been used to join advanced alloys [31,32], and can offer an alternative method for joining Mg alloys-steel dissimilar metals. Elthalabawy and Khan [33]

studied the effect of bonding parameters on microstructural developments and joint strength properties of diffusion-brazed AZ31 magnesium alloy to austenitic stainless steel using a nickel interlayer. They reported that the shear strength of the joints reached a maximum value of 46 MPa for a bonding time of 20 min. at 510 ºC [33]. However, joint strengths decreased with an increase in bonding time to 60 min. due to the formation of intermetallics within the joint during isothermal solidification [33]. The long thermal cycle of diffusion welding/brazing process promotes formation of brittle intermetallic compounds along the interface of dissimilar joints. This process is not classified as a mass production process [32, 33].

2.4.3 Laser-GTA (Gas Tungsten Arc) Hybrid Welding

Laser-GTA hybrid welding process, which is a modern welding technique with high efficiency, can be used for Mg alloys-steel dissimilar joints. The high energy beam facilitates high speed welding with full penetration in materials; however, the absorption of laser energy in some materials is rather low causing high consumption of electric power [7]. After an electric arc is incorporated into the laser welding process in an appropriate way, the efficiency of the laser beam is enhanced and the arc and laser together cause improvement of laser welding characteristics [7]. The high energy intensity of lasers makes the steel and magnesium alloy melt simultaneously [34]. In this process, molten magnesium and steel should be completely mixed due to fast stir action in the molten pool [7].

Liu *et al*. [7,34,35,36,37] have used the laser-GTA hybrid welding for Mg alloy-steel joints without and with using an interlayer element between them. More details of these studies are discussed in this section.

Laser-GTA hybrid welding of steel and magnesium alloy without an interlayer

Liu *et al*. [7] have studied the welding of AZ31B magnesium alloy and 304 steel in a lap joint design. The main focus of this study was on the interface of Mg-Fe joints to determine the weldability of Mg-Fe lap joints by laser-GTA hybrid welding [7].

A schematic diagram of their laser-GTA hybrid set-up was shown in Figure 2-4 [7]. The steel sheet was not placed on top, because it needs more power to melt and this may cause the magnesium to vaporize resulting in formation of large pores in the fusion zone [7,34].

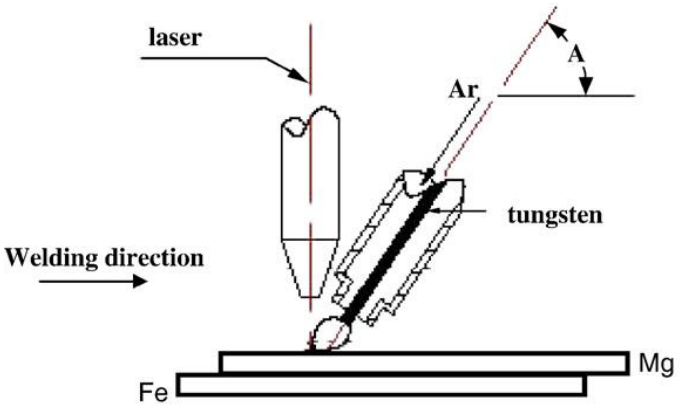

Figure 2-4: Schematic of laser-GTA hybrid welding (taken from Liu and Zhao [7]).

As there is no interaction between Mg and Fe, the interfaces of the Mg alloy and steel were reported to be clear without a transitional zone [7]. A series of discrete gaps were produced at the interface of Mg alloy and steel, suggesting that the bonding between Mg alloy and steel had not formed [7].

The problem with the laser-GTA hybrid welding of steel and magnesium alloy is the high temperature at the interface of the Fe matrix that causes the liquid magnesium alloy to evaporate [7]. In addition, the oxidation of unprotected steel occurs. In a lap welding process, the interface between Mg and Fe is difficult to protect. The result was heavy oxidation of the interface and all the joints were fractured along the Mg-Fe interface [7].

Laser-GTA hybrid welding of steel and magnesium alloy with use of an interlayer

Steel and magnesium do not interact with each other. Therefore, to obtain a reliable joint between these two metals, an intermediate element that can interact with both Mg and Fe should be inserted. Liu and Qi [34] studied GTA hybrid welding of AZ31B magnesium alloy

to mild steel Q235 in the lap joint configuration with the addition of a copper interlayer, in a form of 0.1 mm thick 99.9 wt.% Cu sheet. The schematic of the process was similar to Figure 2-4 [34]. It was found that the addition of Cu improved the wettability of molten magnesium alloy on steel and facilitated its nucleation on steel [34]. However, no detailed study on wettability of molten magnesium on the steel was reported. It was also reported that the addition of a Cu interlayer not only allowed joining between the Mg alloy and steel, but also contributed to the improvement of strength and effectively led to a metallurgical bond [34]. The tensile shear strength of the joint was reported to be 170 MPa. The same behaviour was observed using a Ni interlayer. In further study by Qi and Song [36], 0.1 mm thick Ni sheet was used as an intermediate element between the steel and AZ31B Mg alloy during the hybrid laser-GTA welding process. It was reported that the interaction of Ni with both Mg and Fe facilitated joining of the AZ31B Mg alloy and steel [36] and the result was formation of a joint with 166 MPa tensile shear strength. Compared with the Cu interlayer, the strengthening effect of joints was similar [36]. The reason for these similarities between microstructure, mechanical properties, and wetting properties of the laser-GTA hybrid welded Mg alloy-steel joints using Cu and Ni interlayers was not reported and further studies are required.

Using the same hybrid process, Liu *et al*. [35] have investigated joining of AZ31B Mg alloy to Q235 steel with the addition of a 0.3 mm thick Sn interlayer. The main reason for choosing Sn in this study was based on examination of binary phase diagrams of Mg-Sn and Sn-Fe that show Sn can interact with both Mg and Fe. Formation of intermetallic phases between Mg and Sn and solid solubility of Sn into Fe were observed in their binary systems [35]. It was found that the addition of Sn eliminated the gaps distributed along the fusion zone-steel interfaces, because the Sn improves the wettability of the Mg to the steel. However, no detailed studies on the fusion zone-steel interface and wetting mechanism between the steel and fusion zone were reported. Further investigation is needed to find the real bonding mechanism when Sn is used as an interlayer between magnesium alloy and steel.

2.4.4 Laser Welding

The laser lap welding of 3 mm thick AZ31B magnesium alloy to 1.2 mm thick Zn-coated steel was recently studied by Wahba and Katayama [38]. An unstable welding process was reported due to the difference in the physical properties between the two materials (particularly in a keyhole mode when the laser beam penetrated into the steel specimen) [38].

The fracture strength of 6000 N was reported for a 25 mm wide specimen and the joint failed in the AZ31B fusion zone [38]. Formation of brittle Mg-Zn eutectic phase in the fusion zone degraded mechanical properties of the joint and caused the fracture to occur in the fusion zone rather than the steel-Mg alloy interface [38]. Formation of a 450 nm thick layer of Fe_3Al intermetallic compound on the steel surface was also observed as a result of the interaction between Al from the AZ31B alloy and Fe [38].

2.4.5 Resistance Spot Welding (RSW)

Liu *et al*. [39] studied the resistance spot welding (RSW) of AZ31B magnesium alloy to DP600 steel using Zn interlayer in the form of Zn coated steel sheet. They found that a pre-existing transition layer of Fe_2Al_5 between the Zn coating and the steel improved wetting and bonding between the steel and the magnesium alloy [39].

The main limitation of this technique is the inherent limitation of the RSW process. It can create only localized joints, which may not be particularly strong. In addition, if the steel surface is covered by high melting temperature oxide layers, such as Al_2O_3 for Al-coated steels, NiO for Ni-plated steels, Cr_2O_3 for stainless steels, breaking the oxide layer and providing the conditions for wetting of the oxide free steel surface by molten Mg alloy and as a result formation of a metallurgical bond between the steel and Mg alloy would not be possible, since the lap joint configuration of this process limits the effectiveness of the flux.

2.5 Factors Affecting the Joint Strength

The strength of the Mg alloy-steel dissimilar metal joint is mainly affected by the following factors:

2.5.1 Intermetallic Compounds

Formation of intermetallic compounds (IMCs) in joints is closely related to the elements present in the base metals, filler metal, and interlayer. These IMCs may form along the steel-fusion zone interface, the Mg alloy-fusion zone interface, or within the fusion zone. Liu *et al*. [34] reported that with the Cu interlayer added, the grains in the fusion zone became very fine as a new phase was generated along the grain boundaries as shown in Figure 2-5b and d [37]. This IMC (Mg_2Cu) with thin rod-like morphology could block movement of intergranular cracks during tensile testing [34]. This IMC phase was found to play a key role in strengthening the Mg alloy-steel joint [34].

In a similar study, Liu *et al*. [35], reported formation of Mg_2Sn IMC homogenously distributed in the fusion zone of AZ31B Mg alloy-steel joint when using a Sn interlayer. It was found that the formation of Mg_2Sn provided nucleating sites for the molten Mg alloy [35]. As a result, the grains of the Mg alloy were refined by these nucleating sites accompanying the rapid cooling. Therefore, the mechanical strength of the joints are closely related to the morphology and distribution of microconstituents [34-37], especially to those of intermediate phases formed in the FZ of the joint, such as Mg_2Cu, Mg_2Ni and Mg_2Sn.

In some cases, formation of IMCs can be detrimental for mechanical properties of the joints. For instance, it was reported that the formation of a Mg-Ni-Al intermetallic compound along the interface of AZ31B-Ni-316L steel during a diffusion brazing process detrimentally affected the mechanical properties of the final joints due to the brittle nature of this IMC [33]. In an other study, Wahba and Katayama [38] reported formation of a brittle Mg-Zn phase in the fusion zone of the laser welded AZ31B Mg alloy to Zn-coated steel joint, which degraded the mechanical properties of the joint.

Formation of an IMC of Fe_4Al_{13} at the lap interface of FSWed AZ31B Mg alloy sheet to low carbon steel sheet was reported to be the key factor for bonding of Mg alloy to the steel [27,28]. In laser welding of AZ31B Mg alloy to Zn-coated steel sheets, formation of a 450 nm thick layer of Fe_3Al IMC on the steel surface was also observed as a result of the interaction between Al from the AZ31B alloy and Fe [38].

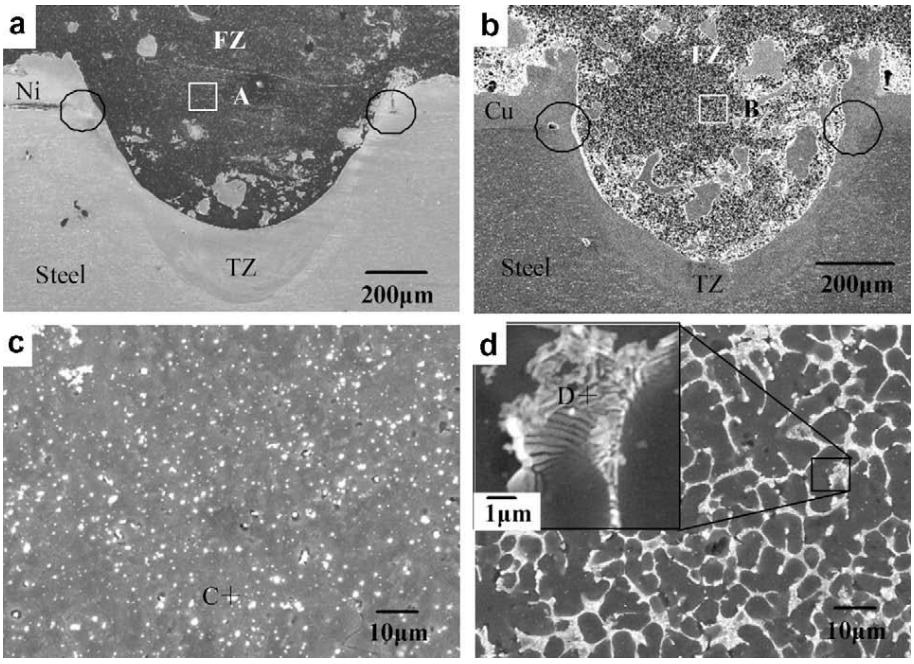

Figure 2-5: SEM images of transverse sections of the joints and the FZ: (a) Ni-added joint, (b) Cu-added joints, (c) from region A of (a), (d) from region B of (b) (taken from Liu *et al.* [37]).

From the above studies, it was concluded that the formation of intermediate phases in joints is related to the materials selection for the joining process, mainly filler metal and interlayer compositions. Formation of these IMCs along the steel-Mg alloy interface can facilitate metallurgical bonding between the Mg alloy and steel, but they can also be detrimental for mechanical performance of the joints.

2.5.2 Transitional Zone

Formation of a transitional zone mostly composed of a solid solution of an interlayer element in Fe along the Mg-steel interface is the key for bonding of the interlayer to the steel from one side and to the Mg from the other side. Liu *et al.* [34] reported formation of a transitional zone (TZ) composed of a solid solution of Cu in Fe at the interface of Mg-Cu interlayer-steel (see Figure 2-5b). The formation of a TZ in the form of Ni solid solution in Fe along the edge

of the weld pool on the steel side was also reported for AZ31B Mg alloy-Ni interlayer-steel joints as shown in Figure 2-5a [37]. Specially, the part of the TZ in circled regions shown in Figure 2-5a and b was reported to wrap around the FZ and prevent it suffering from external load directly during tensile shear test. This was reported to significantly increase the joint shear strength [37].

In a study of diffusion brazing of austenitic stainless steel alloy 316L to magnesium alloy AZ31B using a pure nickel interlayer by Elthalabawy and Khan [33], the increase in joint strength was attributed to the formation of a solid-state Ni-Fe reaction layer at the 316L steel-Ni interface.

2.5.3 Interfacial Strength

In dissimilar metal combinations, the strength of the interface between two solid phases, where the lattice planes of each phase meet each other, is critical in terms of bond strength. As mentioned in previous sections, formation of a reaction product (in the form of solid solution or intermetallic compound) along the interface between the Mg and steel is responsible for formation of a metallurgical bond between them. The formation of the reaction product(s) is associated with the formation of new interfaces. The formed bond strength is not just dependent on the properties of the reaction products and the base metals, such as their elastic modulus or brittleness, but also the reliability of the formed solid-solid interface itself is vital.

The solid-solid interfaces are classified as coherent interfaces, semicoherent interfaces, and incoherent interfaces [40]. In coherent interfaces two crystals match perfectly at the interface plane [40]. Disregarding the chemical species, coherent matching can be achieved when the interfacial planes from both sides have the same atomic configuration (crystal structure), orientation, and interplanar distance [40]. A slight difference in the lattice constants along the interface can cause a deviation from the perfect coherence and deformation of the lattice, which results in a reduction in work of adhesion and bond strength [40].

When there is no perfect match between two crystals lattices (semicoherent interfaces), due to different lattice parameters between the substrate and the reaction product or the reaction product and the solidified region, an intrinsic strain in the reaction product arises (see Figure 2-6). This strain (mismatch strain) can cause fracture of the interface during tensile loading [41,42]. The magnitude of this extensional strain is proportional to the lattice mismatch between the reaction product and the substrate ($\varepsilon_0 = \frac{d_S - d_R}{d_S}$, where d_S and d_R are the lattice parameters of the substrate and reaction product, respectively, as shown in Figure 2-6). Schematic shown in Figure 2-6 has been made by the author.

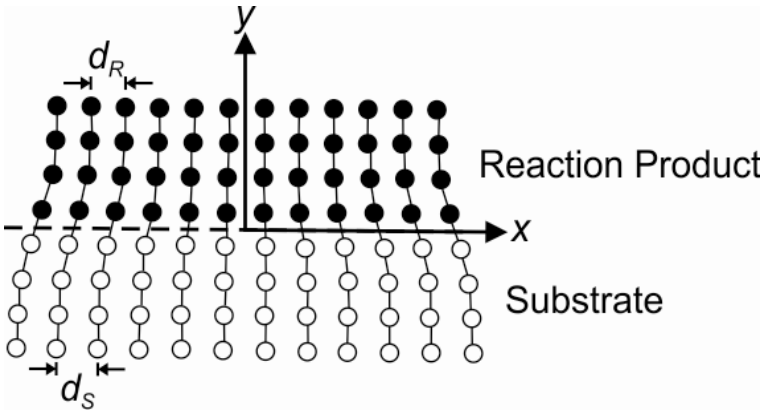

Figure 2-6: Mismatch strain along the substrate-reaction product interface in their adjoining lattices.

The free (strain) energy density, E_ε, associated with isothermal linear-elastic straining of a crystalline reaction product (as given by Hooke's law) is [43]:

$$E_\varepsilon = \frac{G}{1-\nu}\varepsilon_0^2 f^2(y) \tag{2.1}$$

where G and ν are shear modulus and Poisson's ratio of the reaction product, respectively, and $f(y)$ is the unit step function. Therefore, the strain energy is always positive, and proportional to the square of the strain. The strain, in turn, is proportional to the lattice mismatch between the substrate and the reaction product. This strain energy will increase the total interfacial energy [40].

Unless the mismatch between the interplaner spacings is small, the mismatch strain would develop between the substrate and the reaction product [43], thereby decreasing the strength of the interface and degrading the total fracture strength of the bond. Liu *et al*. [44] reported formation of semicoherent interfaces and a good bond with less than 5 % interplanar mismatch between the Fe_2Al_5 (reaction product) and the steel and Mg. Thus, lattice matching at the interface between the two dissimilar phases is one of the major factors governing the characteristics of interfacial strength. Zhang *et al*. [45] used an edge-to-edge matching crystallographic model to predict all the orientation relationships between crystals that have simple hexagonal close packed (HCP) and body-centered cubic (BCC) structures and they found that the lattice mismatching of HCP (Mg) and BCC (Fe) is very large. This causes immiscibility between Fe and Mg that results in an atomically or compositionally sharp interface, without any intermixing or transition layer. Thus, poor wetting and weak bonding will occur when the lattice mismatching of the two immiscible elements or compounds is large [44].

2.6 Wetting

A comprehensive study of the factors responsible for the wetting of a solid by a liquid metal is not only of scientific interest, but also of significant technological importance. This information is particularly valuable for many metallurgical processes, for instance, fabrication of metal-ceramic composites, thin film materials, hot dip metallic coating of steel, soldering in microelectronics, and brazing processes [46]. The basic process of brazing or soldering depends on wetting for the formation of braze- or solder-to-base metal contact. Solidification of molten braze or solder after wetting results in a permanent bond. Therefore, the brazeable/solderable surfaces must allow the molten braze to wet and spread within the available time [47].

Wetting or spreading can be broadly classified into two categories, viz., non-reactive wetting and reactive wetting [48]. A liquid spreading on a substrate with no reaction/absorption of the liquid by the substrate material is known as non-reactive or inert wetting [48]. Spreading of molten magnesium on steel is an example of non-reactive wetting,

which has been reported to be very poor [7]. On the other hand, the wetting process influenced by a reaction between the spreading liquid and substrate material is known as reactive wetting [48]. Using an appropriate interlayer between Mg alloy and steel can provide the conditions for reactive wetting and improvement of wettability. Alteration of the interface and formation of intermetallic compounds are the important features of reactive wetting [48].

In reactive wetting, the wetting is followed by material transport at the solid/liquid interface. A chemical reaction generally occurs between the mating surfaces and the resultant chemical bonds are responsible for wetting. Hence, according to conventional thermodynamics, reactive wetting should be possible and occur spontaneously whenever the change in free energy for the interfacial reaction, ΔG_r, is negative [48].

Eustathopoulos and co-workers [49,50,51,52,53] carried out extensive work in the field of reactive wetting. They studied wetting behaviour using the sessile drop technique in a number of reactive systems including systems with good wetting as well as non-wetting behaviour in order to analyze the mechanism of wetting. The following equation was proposed for the smallest contact angle in a reactive system with limited/moderate reactivity:

$$\cos\theta_{\min} = \cos\theta_0 - \frac{\Delta\gamma_r}{\gamma_{LV}} - \frac{\Delta G_r}{\gamma_{LV}} \qquad (2.2)$$

where $\theta_{\min}$ is the smallest contact angle in a reactive system, γ_{LV} is the surface tension of the liquid, θ_0 is the contact angle on the substrate in the absence of any reaction, $\Delta\gamma_r$ represents the change in interfacial energy due to interfacial reaction and ΔG_r is the change in free energy per unit area released by the reaction of the material contained in the immediate vicinity of the metal/substrate interface [52]. Therefore, the interfacial energy change affected by interfacial reactions could be a major cause for enhanced wetting in reactive systems [52].

Eustathopoulos [50] proposed a reaction product control (RPC) model to explain the reactive wetting behaviour (see Figure 2-7). According to this model, the final degree of wetting and contact angle, θ_F, and the spreading kinetics are controlled by the new compound formed at the interface and not by the parent base metal [53].

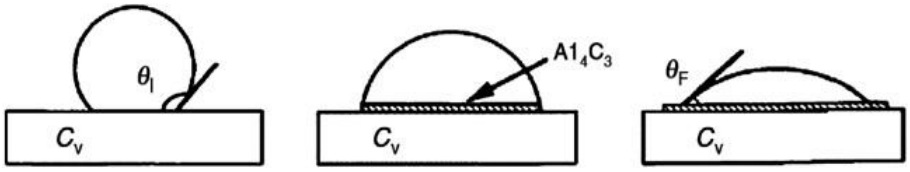

Figure 2-7: RPC model for reactive wetting (stages of reactive wetting of liquid aluminium on vitreous carbon substrates) (taken from Eustathopoulos [53]).

In reactive systems, the steady contact angle between solid and liquid is nearly equal to the contact angle of the liquid on the reaction product itself; the generally accepted reactive wetting mechanism in metallic-metallic systems [50]. As a result, the final contact angle is given by applying Young's equation to the liquid-reaction product-vapour system instead of liquid-solid substrate-vapour [50]. Therefore, it has been accepted that the liquid-reaction product interfacial energy has a dominant effect on wetting. The effects of other factors, such as the reaction product-substrate interfacial energy or other reaction products which are not in direct contact with the liquid phase have not yet been studied. An example which highlights weakness of the reactive wetting mechanism proposed above is the wetting of Sn-3Ag-xBi solders on Fe-42Ni alloy substrate studied by Saiz *et al*. [54]. Their results showed different contact angles of 57º and 77º when the temperature was 250 ºC and 450 ºC, respectively. Moreover, they showed different reaction product(s), which was Fe (substrate)-$FeSn_2$ (reaction product)-Sn (solder) at 250 ºC and Fe-FeSn-$FeSn_2$-Sn at 450 ˚C. However, the underlying mechanism behind varying contact angles was not provided and cannot be simply explained using the proposed mechanism for reactive wetting in metallic-metallic systems, since the immediate reaction product in contact with Sn solder was $FeSn_2$ in both cases.

As mentioned in the previous section, the mismatch strain energy along the substrate-reaction product interface, which is proportional to the square of the strain, will increase the total interfacial energy [40]. This energy will increase the total free energy needed to overcome the wetting barrier. Thus, the interfacial energy and wetting can be dependent on the crystallographic dis-registry and lattice matching in between the reaction product(s) and

the substrate. However, no detailed study on the effect of the lattice matching on wettability in multi-component metallic systems has been reported.

2.7 Summary and Concluding Remarks

Review of the literature reveals that joining Mg to steel by conventional fusion welding technologies is impossible. Also, using solid-state joining techniques, such as FSW, resulted in formation of a mechanical bonding between the Mg and steel with low joint strength, since no metallurgical bonding forms between these two elements. Therefore, in order to keep the steel in the solid-state and avoid evaporation of the magnesium, the remaining option to join Mg to Fe will be the brazing technique provided another element that can interact and bond with both of them can be applied between the Mg and Fe and act as an intermediate interlayer element or alloy. The product of this interaction is either the formation of a solid solution or a layer of an intermetallic compound. The formation of thick, brittle intermetallic compounds is not favourable due to degradation of mechanical properties of the joint as failure of the joint will occur at relatively low loads due to fast fracture of the brittle intermetallic layer. Laser beams with high localized energy input and precise control of the beam energy can provide high joining speeds and accompanying high cooling rates. The resulting limited reaction time minimizes the formation of unfavourable intermetallic compounds at the joint interface. Therefore, using a laser beam for joining magnesium alloys to steel is recommended. Since there was no study available in the literature on the brazing of Mg alloys to steel sheet, the feasibility of laser brazing of Mg alloy to steel sheet has been studied in this work.

Using Ni, Cu, and Sn as an interlayer between Mg and steel were suggested during laser-GTA hybrid welding of steel to Mg alloy sheets. However, more fundamental studies are needed to find the strengthening mechanism of these interlayers. In addition, the strengthening mechanism of these interlayers might be different in the laser brazing process relative to the laser-GTA hybrid welding, since steel stays in solid-state in the laser brazing process, but Mg alloy and steel are melted simultaneously in the laser-GTA hybrid welding.

Further investigations are required to understand the fundamental metallurgical phenomena responsible for bonding between Mg and steel and to study strengthening mechanisms associated with using an interlayer between Mg and steel during the laser brazing process.

Selection of the best type of the interlayer to use between Mg and steel will be another issue that must be considered during a study of the feasibility of using the laser brazing process to join these two metals. As an alloying element, Al improves fluidity, room temperature strength and hardness of the Mg alloy. As an interlayer between Mg and Fe, Al with FCC (face-centered cubic) structure is more favoured than having a BCC phase along the interface [45]. It is also worth noting that formation of an intermetallic compound along the interface can be helpful for formation of a metallurgical bond between Mg and Fe. It has been reported that Fe-Al IMCs/Fe interface has a low interfacial energy with good match of lattice sites [55]. A recent study by Liu *et al*. [44], showed that a nano-layer of Fe_2Al_5 on steel can be a transition layer to bond Fe to Mg due to the low energy interfaces and good matching of lattice sites between Fe and Fe_2Al_5 as well as Mg and Fe_2Al_5. Therefore, Al is expected to act well as an interlayer alloy between Mg alloy and steel during laser brazing process.

Another possible interlayer element is Ni. With a FCC crystal structure, unlimited solid solubility with Fe at the laser brazing temperatures, and having the same valence as Mg and Fe, Ni is a good candidate to be applied and studied between Mg alloy and Fe during the laser brazing process. Having the same crystal structure (FCC), very close electronegativity (1.91 and 1.90 for Ni and Cu, respectively), the same atomic radius (135 pm), and the same valence (two) can cause similar behaviour for Ni and Cu as an interlayer between steel and magnesium alloy during joining processes, such as laser-GTA hybrid welding [37] or the laser brazing process. As a result of these similarities in the Mg-Cu-Fe and Mg-Ni-Fe systems, both Cu and Ni react with Mg via a eutectic reaction and the products of these reactions are Mg_2Cu and Mg_2Ni, respectively [37]. Therefore, from a microstructure and mechanical strength point of view, using Cu and Ni showed the same behaviours as an interlayer between magnesium alloy and steel [37]. Sn was also reported to react well as an interlayer between Mg and steel during laser-GTA hybrid welding. However, no detailed

studies on the steel-fusion zone interface were reported. Therefore, using Al, Ni, and Sn interlayers between Mg and steel in the laser brazing process and also studying the strengthening mechanisms of the joints were proposed and investigated in this work.

Identifying and evaluating an appropriate interlayer between steel and Mg alloys experimentally can be costly and time consuming. This process can be shortened with the use of computational thermodynamics, which provides a convenient way for predicting the phases most likely to form in complex multi-element alloy systems at the interface as a function of alloy composition and temperature with greater accuracy than is possible using the binary or ternary phase diagrams of the constituent elements. Prior knowledge of these phases can be beneficial as they can affect the mechanical properties, the temperature of the joint interface, the wettability of the steel by the magnesium alloy and the overal brazeability of the joint.

In the last decade, several different commercial thermochemical codes have become available for the calculation of the phase stability in multi-component systems [56-59]. These codes can be used to predict the free energy of competing phases as a function of temperature, pressure and composition, and the phases and their compositions that lead to the minimum free energy, *i.e.*, phase equilibrium. The key to all of these computational tools is the database that contains all relevant thermodynamic model parameters required to describe the functional behaviour of the Gibbs free energy of all phases, including solutions. The unique feature of these computational thermodynamics tools is that phase equilibrium and thermodynamic properties of multi-component systems corresponding to real commercial alloys with ten or more components can be readily modelled and assessed with reasonable accuracy.

Predicting early stage phase formation along a steel-interlayer-Mg alloy interface can be used to choose the appropriate interlayer between the steel and magnesium alloy. Simulation of the phase formation and thermodynamic properties of the phases during different joining processes, such as laser brazing, can be an important tool when developing high temperature joining processes. In this study, computational thermodynamics is used to examine the effect of using a 5 μm thick Ni interlayer between steel and AZ31B Mg alloy

sheet on the phases formed along the fusion zone-steel interface during a laser brazing process using AZ92 Mg brazing alloy.

The basic process of brazing depends strongly on wetting for the formation of braze to base metal contact and the brazeable surfaces (steel and Mg alloy) must allow the molten braze to wet within the available time. There is a need for an in-depth investigation into the molten magnesium alloy-steel interface utilizing detailed and well controlled wetting experiments. This need arises due to the non-existence of studies on the fundamental mechanisms and reaction characteristics at play during the reactive wetting of steels by molten magnesium alloys. Typically, magnesium does not wet or bond to steel [60] because of the nearly zero solubility of magnesium in iron. Wetting can, however, be improved in immiscible alloy systems using an interlayer and forming of a continuous layer of a new solid compound (reaction product) at the interface [61,62].

In this study, a reactive system including Ni electro-plated steel and AZ92 Mg alloy (liquid) using a laser as the heat source is studied to understand the effect of reaction products, especially lattice matching between the interfacial phase(s) formed and the substrate on wettability in a highly reactive metallic-metallic system. Understanding the relationship, if any, between interfacial phases and wetting characteristics in the Ni-plated steel-AZ92 Mg alloy couple with a strong metallurgical bond between the steel and Mg alloy will facilitate increased application and use of Mg alloys in the automotive and aerospace industries.

Since Al was found to have characteristics of an appropriate interlayer between Mg alloy and steel, in the present study, development of laser brazing process for joining Mg alloy to steel was started using aluminized steel. This type of steel sheet is coated by Al-12Si layer and is already used in the automotive industry.

Chapter 3
EXPERIMENTAL METHODS AND CONDITIONS

3.1 Laser Brazing Experiments

3.1.1 Materials

The laser brazing process was carried out on 60×50 mm specimens sheared from 2 mm thick commercial grade twin-roll strip cast AZ31B-H24 Mg alloy sheet and three types of cold-rolled steel sheets including 1 mm thick Al-12Si coated (aluminized) steel, 1 mm thick Ni electro-plated steel, and 0.6 mm thick Sn electro-plated steel sheets were used as the base materials. A 2.4 mm diameter TiBraze Mg 600 filler wire (Mg-Al-Zn alloy) with solidus and liquidus temperatures of 445 ˚C and 600 ˚C, respectively, was chosen for this study. The chemical compositions of the base materials are given in Table 3-1, Table 3-2, and Table 3-3. The commercial flux used in the experiments was Superior No. 21 manufactured by Superior Flux and Manufacturing Co. This powder flux was composed of LiCl (35-40 wt.%), KCl (30-35 wt.%), NaF (10-25 wt.%), NaCl (8-13 wt.%), and $ZnCl_2$ (6-10 wt.%) [63].

Table 3-1: Measured chemical composition of the AZ31-H24 Mg alloy sheet and TiBraze Mg 600 filler metal (wt.%)

	Al	Zn	Mn	Si	Mg
AZ31B-H24	3.02	0.80	0.30	0.01	Bal.
TiBraze Mg 600	9.05	1.80	0.18	---	Bal.

Table 3-2: Measured chemical composition of the aluminum coated steel sheet (wt.%)

C	Mn	P	S	Fe
0.01	0.6	0.010	0.004	Bal.

Table 3-3: Measured chemical composition of the Ni and Sn electro-plated steel sheet (wt.%)

C	Mn	P	S	Fe
0.01	0.5	0.010	0.005	Bal.

Prior to laser brazing, the oxide layers on the surfaces of the magnesium sheets were cleaned by stainless steel wire brushing. All specimens were ultrasonically cleaned in acetone to remove oil and other contaminants from the specimen surfaces.

Figure 3-1 shows an optical microscopic image of the steel/Al-12Si coating layer interface before the brazing process. The Al-12 wt.% Si coating layer on the steel sheet was 20±2 μm thick. In Figure 3-1b, a 3.5 μm thick Fe-Al-Si intermetallic compound (IMC) layer is clearly shown at the interface. This IMC layer was confirmed by X-ray diffraction to be the θ-Fe(Al,Si)$_3$ phase.

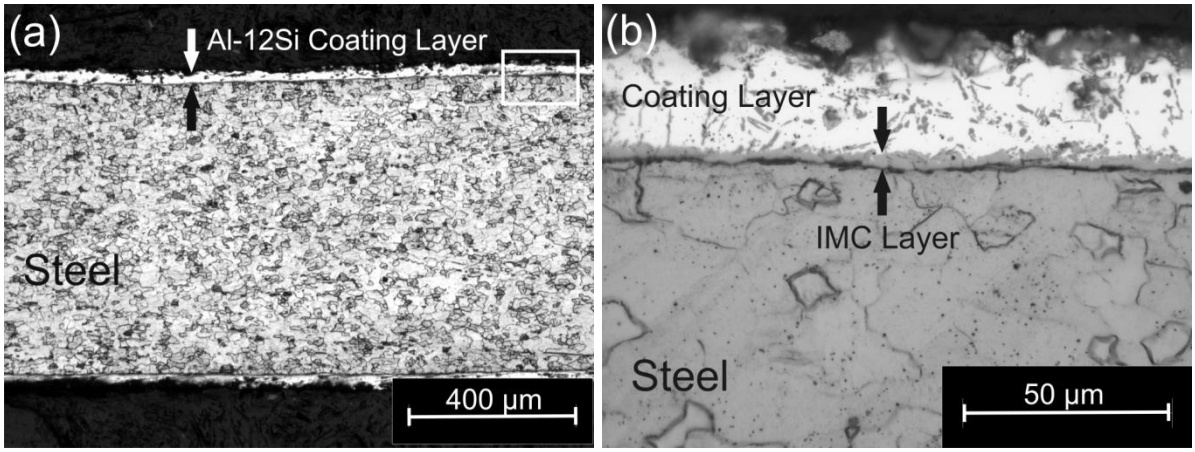

Figure 3-1: Transverse section of the original steel sheet showing: (a) the Al-12Si coating layer and (b) the pre-existing Fe-Al-Si IMC layer at the steel/coating layer interface.

A custom manufactured Ni electro-plated steel sheet was made for this study. For this purpose, the bare steel specimens with the compositions shown in Table 3-3, were cleaned in acetone and then ground to 1000 grit using SiC abrasive paper and again were ultrasonically cleaned in acetone. The prepared surfaces were then immediately electroplated with electrolytic pure nickel. In the Ni electro-plating process, the clean steel sample was the cathode and graphite was the anode. The composition of the electroplating solution and the electroplating conditions are listed in Table 3-4. Figure 3-2a shows a schematic of the Ni

electro-deposition process used. In order to get a uniform 5 µm thick Ni layer on the steel, different cathode current densities and plating times were tested. Electro-deposition of Ni using a cathode current density of 120 mA/cm^2 for 10 min was found to provide a 5.5 ± 0.9 µm thick pure Ni coating layer on the steel with a defect free interface. Figure 3-2b shows a SEM micrograph of the cross section of the nickel-coated steel. The white layer on top of the steel is the Ni coating layer. The coating was of uniform thickness with a void free interface. EDS analysis of the electro-deposited layer on the steel showed a pure Ni coating layer.

Table 3-4: Composition of Ni electroplating solution and electroplating parameters

Plating Solution Composition (g/l)		Electro-deposition Parameters	
$NiSO_4 \bullet 6H_2O$	263	Cathode Current Density	45-120 mA/cm^2
Na_2SO_4	215	Time (min)	5-20 min
H_3BO_3	31	pH	3
		Temperature	25 ˚C
		Anode	Graphite (8 cm^2)
		Cathode	Carbon Steel (6 cm^2)

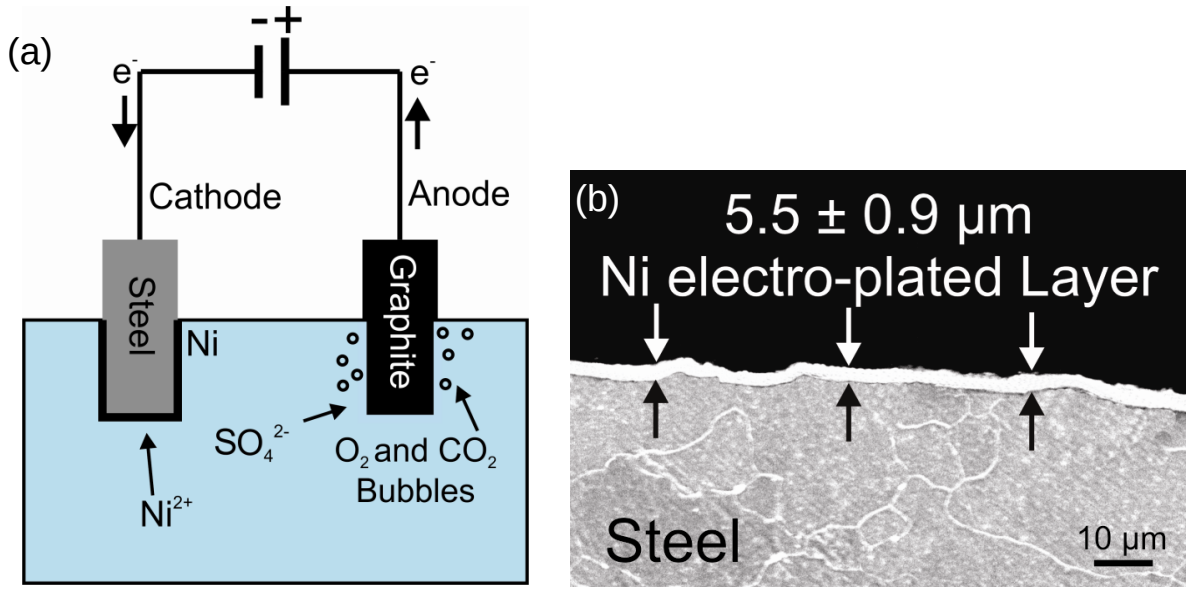

Figure 3-2: (a) Schematic of the Ni electro-deposition process on steel and (b) transverse section of the Ni electro-deposited layer on the steel substrate.

Figure 3-3 shows a SEM micrograph of the cross section of the Sn electro-plated steel. The brighter layer on top of the steel is the Sn coating layer. The electro-plated Sn coating layer on the steel sheet was 3.7 ± 0.7 µm thick. EDS analysis of Sn layer on the steel showed a pure Sn coating layer. The coating was of uniform thickness with a void free interface.

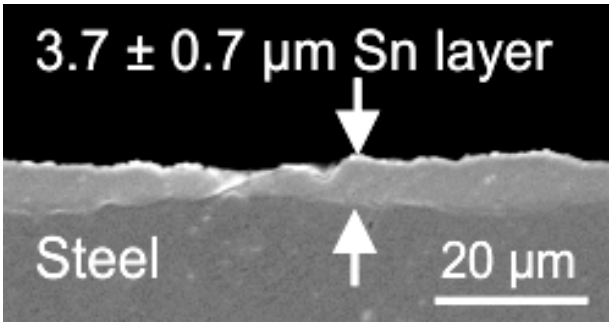

Figure 3-3: Transverse section of the Sn electro-plated layer on the steel substrate.

3.1.2 Joint Design, Laser Equipment, and Process Parameters

In this study, two different joint designs were applied. For the Al-12Si and Ni coated steels, the edge of each steel sheet was bent in order to make a single-flare bevel lap joint after clamping against the magnesium sheet, as shown in Figure 3-4a. When Sn electro-plated steel was used, the AZ31B sheet was clamped on top of the steel sheet to make a lap joint configuration as shown in Figure 3-4b. The filler wire was cut into pieces and pre-set on the work-piece at the joint line with some flux before heating and brazing by the laser beam.

An integrated Panasonic 6-axis robot and Nuvonyx diode laser system with a maximum power of 4.0 kW and a 0.5 × 12 mm rectangular laser beam intensity profile at the focal point was used for laser brazing. This energy distribution is more suitable for brazing processes compared with the non-uniform Gaussian-distributed circular beams generated by CO_2 and Nd:YAG lasers [64]. The beam was focused on top of the filler wire.

In order to limit oxidation, helium shielding gas was provided in front of the molten pool with a flow rate of 30 l/min from a 6 mm diameter soft copper feeding tube. Laser

brazing was performed using a range of laser powers, travel speeds, and beam offset positions.

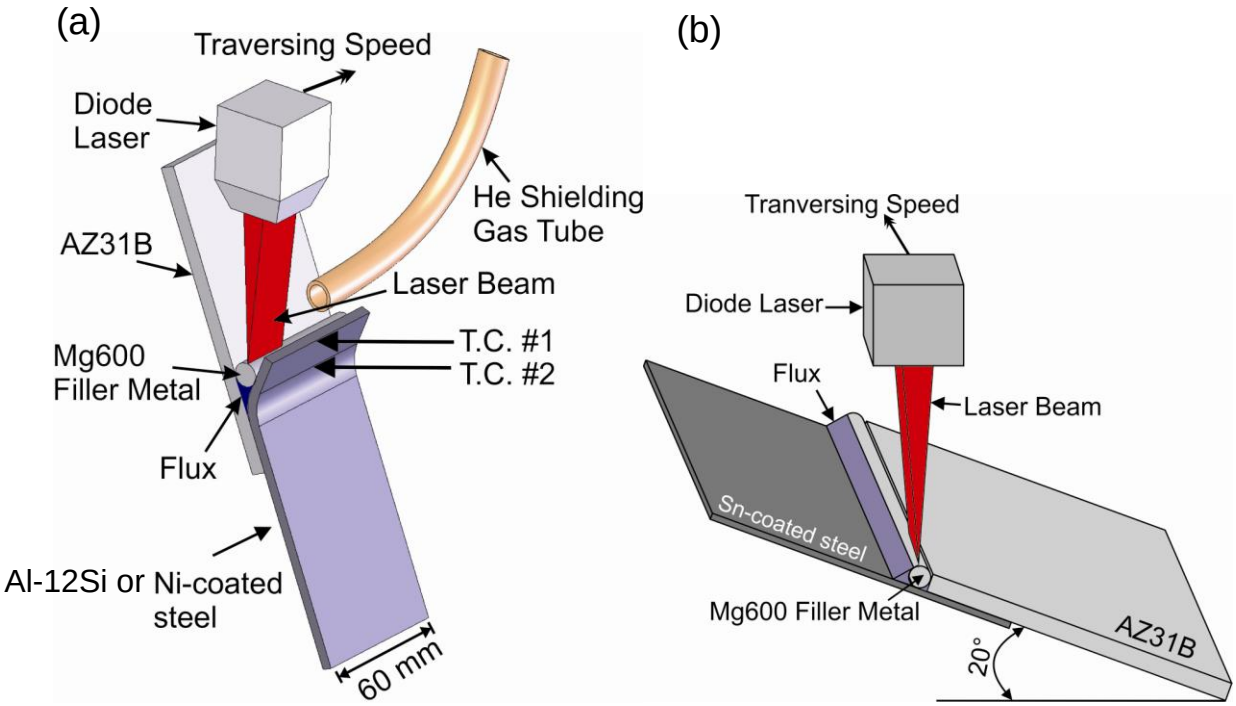

Figure 3-4: Schematic of the laser brazing system used for joining AZ31 Mg and (a) Al-12Si and Ni plated steel sheets in a single-flare bevel lap joint configuration showing the position of two thermocouples used for temperature measurements and (b) Sn electro-plated steel sheets in a lap joint configuration.

3.1.3 Microstructural Examination

After laser brazing, transverse cross-sections of the brazed specimens were cut and mounted in epoxy resin. The samples were then mechanically ground using 300, 600, 800, 1000, and 1200 grades of SiC grinding papers followed by polishing using a 1 µm diamond suspension. The polished specimens were etched to reveal the microstructure of the braze metal and AZ31B base material. The etchant was comprised of 20 ml acetic acid, 3 g picric acid, 50 ml ethanol, and 20 ml water [65].

Macro- and microstructures of the etched joints were examined using an optical metallographic microscope. The microstructure and composition of different zones of the joint cross section were determined using a JEOL JSM-6460 scanning electron microscope (SEM) equipped with an Oxford INCA energy dispersive X-ray spectrometer (EDS). Phase characterization of the phases formed in the steel-fusion zone interface and on the fracture surfaces was carried out using X-ray diffraction (XRD) phase analysis in a Rigaku AFC-8 diffractometer with Cu target, 50 kV acceleration voltage, and 40 mA current.

Transmission electron microscope (TEM) foils were prepared using the focused ion beam (FIB) (Zeiss NVision 40 [Carl Zeiss, Chicago, IL] FIB/field emission-SEM) and an in situ lift-out technique [66]. A carbon coating was deposited prior to FIB milling to protect the sample surface and the area of interest upon exposure to the Ga^+ beam. Once the TEM foil was attached to a Cu grid, final thinning was performed on the lamella, initially at an acceleration voltage of 30 kV, and finally at a low voltage of 1 kV because the milling of the Mg-Al fusion zone is much faster than that of Ni-plated steel substrate. Details of this procedure can be found in Ref. 66. The TEM studies were performed with a JEOL 2010F TEM operated at 200 kV equipped with an Energy Dispersive X-ray Spectrometer (EDS).

3.1.4 Mechanical Testing

Vickers microhardness profiles across the brazed joints were measured using a 50 g loading force and 10 s holding time. As shown in Figure 3-5, the brazed 5 mm width rectangular shaped specimens were cut and subjected to tensile shear tests with a crosshead speed of 1 mm/min. Shims were used at each end of the specimens to ensure shear loads in the lap joint while minimizing induced couples or bending of the specimens. Average tensile shear strength was calculated from tensile specimens to estimate the static mechanical resistance and efficiencies of the joints.

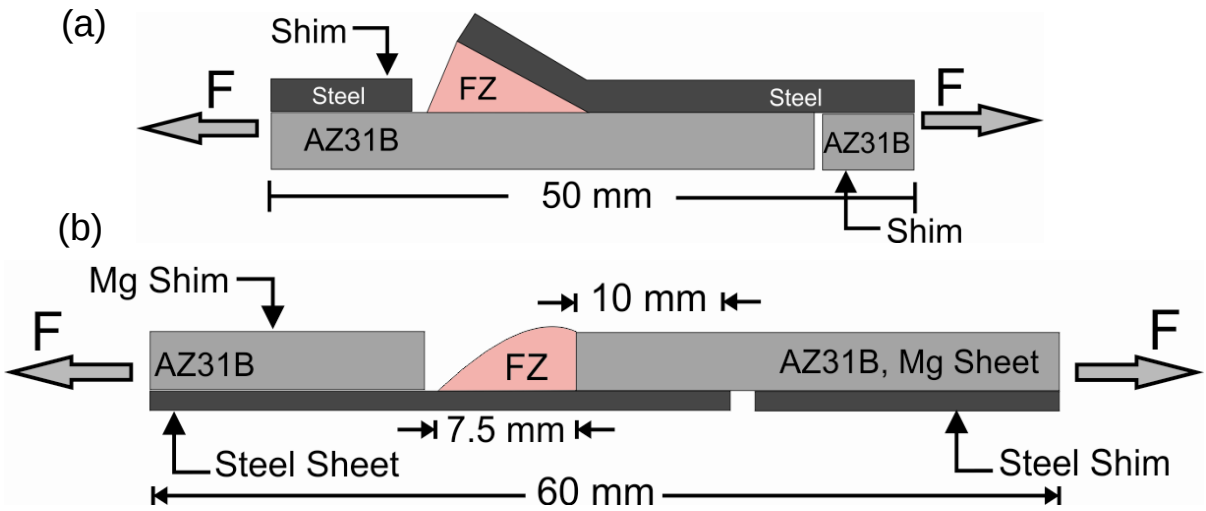

Figure 3-5: Schematic of the 5 mm wide tensile shear test specimen using (a) Al-12Si and Ni plated steel and (b) Sn plated steel sheets.

3.2 Wetting Experiments

Spreading of a homogeneous alloy droplet is normally performed under fully isothermal conditions using transferred drop (TD) [67] or dispensed drop (DD) [68] types of sessile drop techniques. However, these isothermal conditions differ from real practical applications which have inherent non-equilibrium thermodynamic conditions. In the present study, wetting experiments were performed using the classic version of the sessile drop technique in which a piece of the AZ92 Mg alloy was placed on the steel substrate and the system was heated to the experimental temperature. In order to simulate and characterize the wetting behaviour close to the laser brazing conditions, a 4 kW diode laser was used to heat and melt the Mg alloy.

In this work, 30 × 40 mm coupons were cut from 0.25 mm thick Ni electro-plated steel sheet and used as the substrate. The Ni coating layer on the steel sheet was 5 µm thick. A 5 mm length of Mg alloy (2.4 mm diameter around 0.3 g) specimen was cut and the oxide layer on the surface of the specimen was cleaned by grinding using SiC abrasive paper. The chemical compositions of the steel sheet and the Mg alloy were exactly the same as those

used in laser brazing experiments (given in Table 3-1 and Table 3-3). All specimens were ultrasonically cleaned in acetone to remove oil and other contaminants from the specimen surfaces. The Mg alloy specimen was then placed in the middle of the steel substrate as shown in Figure 3-6. The flux provided enough shielding during the wetting test; therefore, a shielding gas was not necessary.

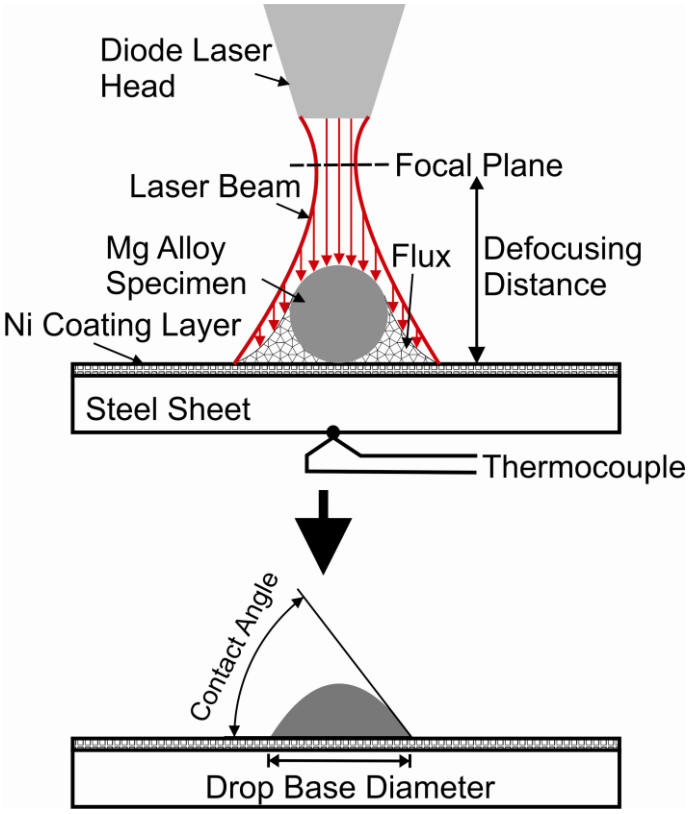

Figure 3-6: Schematic of the wetting test.

The wettability test was performed using the same diode laser system as the used laser for the brazing experiments. To obtain a laser beam intensity distribution all over the Mg alloy, 30 mm defocusing of the laser beam was applied. The diode laser beam was used for 1.6 s to melt the Mg alloy specimen on the substrate using different laser powers. Also, to measure the temperature profile versus time at different process parameters a thermocouple was attached to the bottom at the center of the steel substrate (see Figure 3-6).

Each test was repeated five times. After each test, the flux was washed off immediately using hot water. The samples were cross-sectioned using a high speed wafer cutting machine and mounted in epoxy. The mounted samples were ground and polished with silicon carbide coated papers and diamond suspension, respectively. The cross sectioned samples were photographed and the contact angles were measured using CorelDRAW software.

The macro-structure of sample cross-sections produced for the contact angle variation measurements and the microstructure and compositional analysis were determined using a JEOL JSM-6460 SEM equipped with an Oxford INCA energy dispersive X-ray spectrometer (EDS). For TEM analysis of the Mg alloy-steel interface, TEM foils were prepared using the FIB and in-situ lift out technique [66]. The Mg alloy-substrate interface was observed with a Titan 80-300LB, a high resolution HRTEM/STEM made by FEI Company operated at 300 kV.

Chapter 4
Laser Brazing of AZ31B to Al Coated Steel Sheet

A diode laser brazing procedure has been developed for joining AZ31B-H24 Mg alloy sheet to aluminum coated cold rolled carbon steel sheet in the single flare bevel lap joint configuration using a AZ92 Mg alloy filler wire. This included determination of the laser brazing process conditions required to make the brazed joints, detailed microstructural evaluation of the brazed joint, Al coating-steel interface, and steel-fusion zone interface and the mechanical performance of the joints. The work presented and described in this chapter has been previous published by Nasiri *et al*. [69].

4.1 Microstructures of the Brazed Joints

Using bare steel resulted in no bonding between steel and the braze alloy fusion zone (FZ) and the wetting of the steel by the braze metal was very poor (see Figure 4-1). The top surface appearance of a laser brazed joint and typical cross sectional view of laser brazed Mg to Al coated steel are shown in Figure 4-2. When using 2.2 kW laser power, 8 mm/s travel speed, and 0.2 mm beam offset to the steel side, a uniform brazed area with good wetting of both base materials and some partial melting of the AZ31B base metal was observed. The Al-Si coating on the surface of the steel significantly improved the wetting of the steel by molten Mg-Al filler metal resulting in metallurgical bonding with the fusion zone.

Figure 4-1: Cross sectional view of laser brazed AZ31B to bare steel sheets made using 8 mm/s travel speed and 2.2 kW laser beam power.

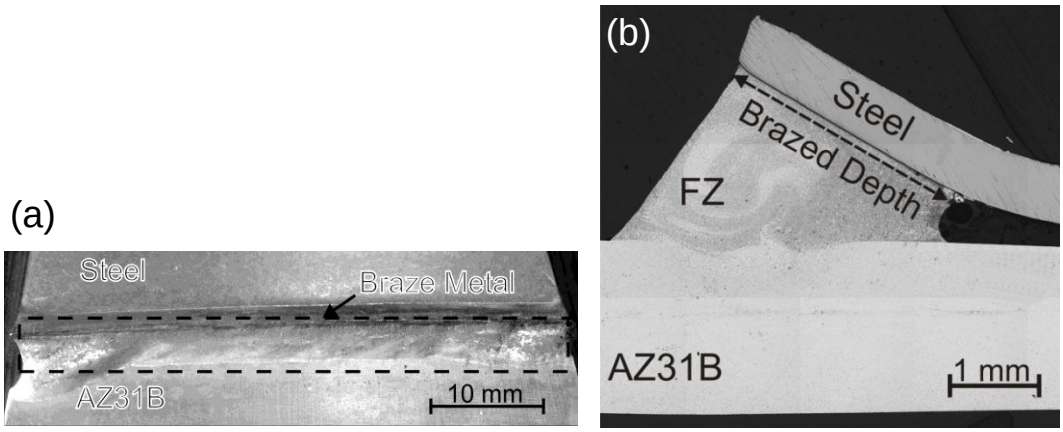

Figure 4-2: Laser brazed AZ31B to steel sheets made using 8 mm/s travel speed and 2.2 kW laser beam power: (a) top bead appearance and (b) transverse section with using Al-12Si coated steel.

The typical microstructure of a laser brazed AZ31B/steel joint transverse section and higher magnification images of various locations are shown in Figure 4-3. Grain growth toward the fusion boundary occurred in the AZ31B Heat Affected Zone (HAZ), as shown in Figure 4-3b. In the Partially Melted Zone (PMZ), localized melting or liquation of intergranular regions occurred as indicated in Figure 4-3c. This was also confirmed by SEM analysis. The thickness of the PMZ layer was not uniform around the fusion zone (20-100 μm) due to the temperature gradient resulting from the laser brazing process. Inspection by optical and scanning electyron microscopy suggested that the small extent of the liquated region did not result in intergranular cracking upon cooling.

As shown in Figure 4-3d, the solidification microstructure adjacent to the fusion boundary was initially planar, but changed to cellular, then columnar-dendritic, and finally equiaxed-dendritic morphologies with increasing distance from the fusion boundary. The black arrow on Figure 4-3d is the same arrow on Figure 4-3a and identifies the orientation of Figure 4-3d in Figure 4-3a. As indicated in Figure 4-3d, the planar, cellular, and columnar grains were only found in a narrow zone adjacent to the fusion boundary while the equiaxed dendrites were dominant in the fusion zone. The microstructure in the center of the fusion zone was homogeneous and characterized by numerous equiaxed dendrites with fine precipitates dispersed in the interdendritic regions, as shown in Figure 4-3e and Figure 4-4.

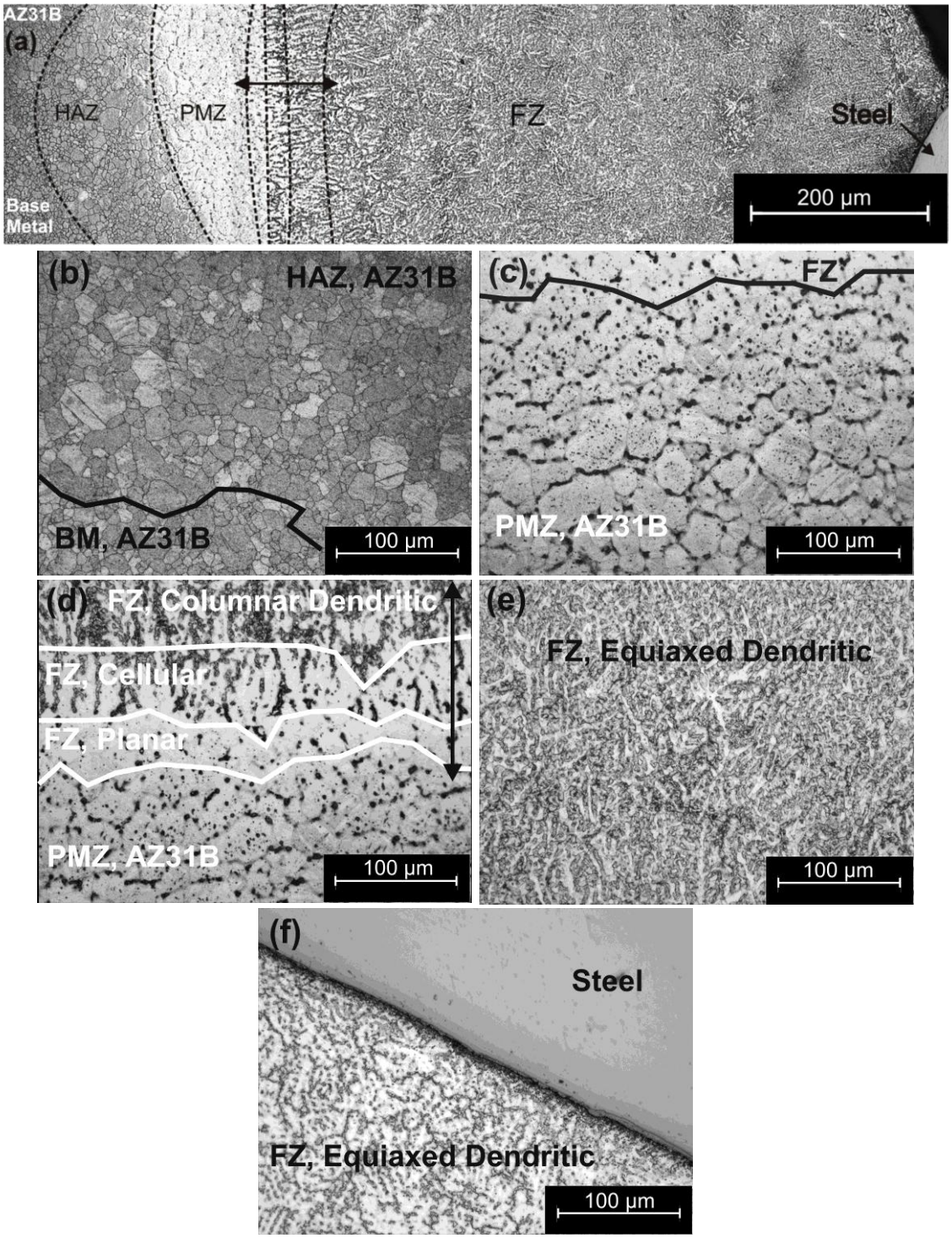

Figure 4-3: Photomicrographs of different microstructural regions in the laser brazed AZ31B/steel joint.

Figure 4-3f shows the microstructure of the fusion zone adjacent to the steel side, which was mainly equiaxed dendritic. Planar and cellular structures were not observed at this interface due to low temperature gradient and cooling rate in this interface compared to the AZ31B/fusion zone interface. This is a result of laser beam offset to the steel side during the laser brazing process and also the high thermal conductivity of AZ31B magnesium alloy as compared to steel, specifically 96 and 30 ($Wm^{-1}K^{-1}$), respectively [70].

A SEM image of the filler metal fusion zone microstructure is shown in Figure 4-4. An intermetallic phase was present at the equiaxed dendrite boundaries. This intermetallic phase appeared as the dark phase in optical microscopic images and as the white phase in the SEM images of the fusion zone. This phase had an average composition of 73.3±3.8 wt.% Mg, 24.5±3.7 wt.% Al, and 2.2±0.1 wt.% Zn, and was thus identified as the β-$Mg_{17}Al_{12}$ intermetallic phase with zinc as a substitutional element. This was confirmed by XRD results. The intermetallic phase was surrounded by supersaturated eutectic α-Mg solid solution that contained on average 92.7±0.5 wt.% Mg, 6.6±0.4 wt.% Al, and approximately 0.7±0.2 wt.% Zn. The eutectic α-Mg and the primary α-Mg dendrites (95.2±1.2 wt.% Mg, 4.3±1 wt.% Al, and 0.5±0.2 wt.% Zn) are outlined in the SEM micrograph of Figure 4-4. Each interdendritic region consisted of a single β-$Mg_{17}Al_{12}$ particle surrounded by eutectic supersaturated α-Mg grown from primary α-Mg dendrites. This type of eutectic is called a divorced eutectic, since the two eutectic phases (α-Mg and β-$Mg_{17}Al_{12}$) are completely separated. This divorced eutectic morphology has previously been reported in microstructures of Mg cast alloys either with high content of zinc or high cooling rates during solidification [71,72]. In this study, the high cooling rate of the laser brazing process and also 2 wt.% Zn content of filler metal promoted formation of the divorced eutectic shown in Figure 4-4.

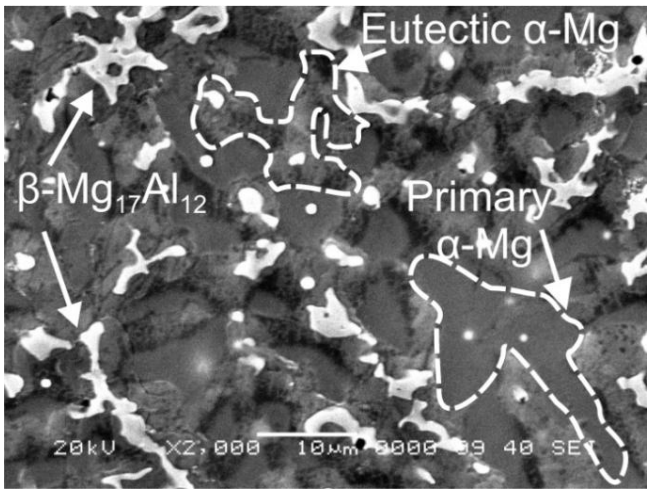

Figure 4-4: SEM image of the fusion zone shows primary and eutectic α-Mg with divorced eutectic β-phase at interdendritic regions.

4.2 Thermal Effect on IMC at Steel/Al-12Si Coating Interface

In order to see the thermal effect of the laser brazing process on the IMC layer on the steel, the opposite steel surface that did not come into contact with the brazing filler metal was examined (see Figure 4-5a). As shown in Figure 4-5b to d, growth of the IMC layer at the interface of the steel/coating layer occurred due to the high temperatures experienced during the brazing process. At the upper part of the interface (Figure 4-5b), the IMC layer showed two morphologies. The first morphology labeled as IMC I in Figure 4-5 adjacent to the steel was a compact plate-like phase thicker than the original IMC layer. The second morphology labeled as IMC II in Figure 4-5 shows long needle-like crystals, which grew from IMC I.

It was observed that upon moving from the location of Figure 4-5b to the location of Figure 4-5d, the needle-like crystals of IMC II gradually disappeared due to the lower temperature experienced during the process. Also, the average thickness of IMC I layer changed significantly from 8 μm at the upper location to about 4 μm at the location of Figure 4-5d compared to the original pre-existing IMC layer between coating layer and steel, which had an average thickness of 3.5 μm.

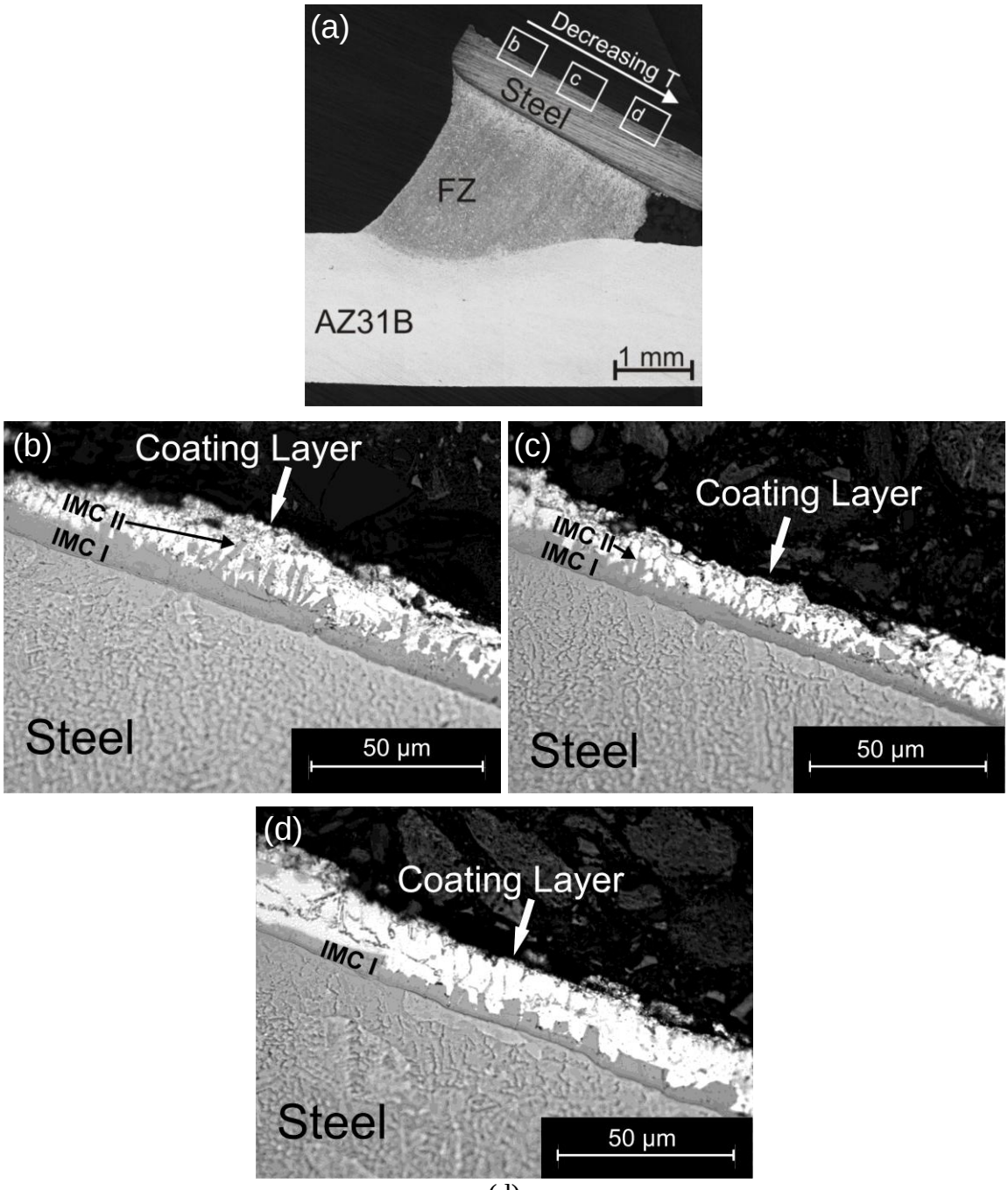

(d)

Figure 4-5: Thickness and morphology variation of IMC layer in different positions of the steel/coating layer interface indicated in (a): (b) upper side, (c) middle side, and (d) bottom side of the joint.

Figure 4-6 shows a SEM image and XRD result of the IMC layer between the steel and Al-12Si coating near the top side of the joint. EDS analysis was carried out for the IMC I layer at locations P1 to P4 in Figure 4-6a, and for IMC II at locations P5 to P8. The EDS results are summarized in Table 4-1. According to the XRD profile of the interface in Figure 4-6b and also composition of IMCs in Table 4-1, the IMCs were determined to be mixtures of the θ-$Fe(Al,Si)_3$ and τ_5-$Al_{7.2}Fe_{1.8}Si$ phases. From the Fe-Al-Si ternary alloy phase diagram and typical characteristics of Fe-Al-Si systems [73,74,75,76], the IMC I layer was determined to consist of the θ-$Fe(Al,Si)_3$ phase, and the needle-like IMC II layer was τ_5-$Al_{7.2}Fe_{1.8}Si$. These layers dissolved 10.4 and 16.1 wt.% of Si in solid solution, respectively, and Si atoms substituted for Al atoms in the IMC phases.

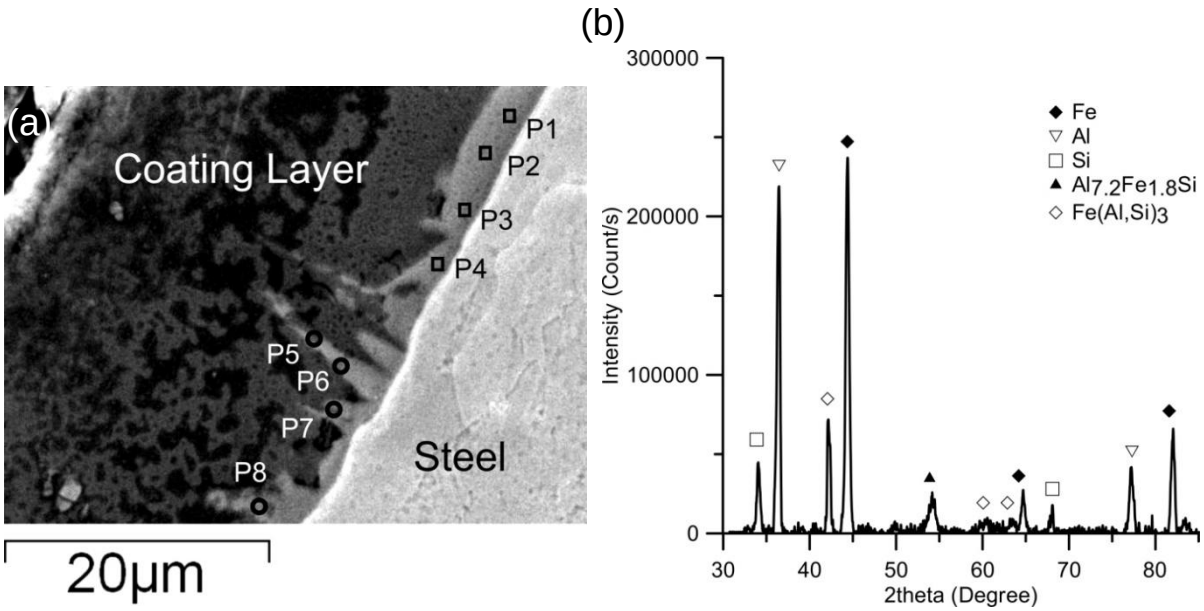

Figure 4-6: Al-12Si coating layer-steel interface of a laser brazed AZ31B-steel joint: (a) SEM image of IMC layer along interface demonstrates locations with EDS analysis and (b) X-ray diffraction pattern of the interface.

Table 4-1: EDS analysis results of IMC layers at the original steel/coating layer interface (wt.%)

IMC	Al	Si	Fe
I (P1-P4)	56.6±1.4	10.4±0.1	32.9±1.3
II (P5-P8)	62.6±2.6	16.1±1.6	21.3±1.2

The rationale for having 12 wt.% Si in composition of coating layer is explained as follows. According to previous work on hot dip aluminizing [77], the solubility of Fe in an aluminum bath increases from 5.3 wt.% to 12 wt.% with the content of Si increasing from 0 wt.% to 10 wt.% at 800 ˚C. With Al-12Si coating layer on the steel in this study, more Fe atoms were able to dissolve into the coating layer to form a thicker Fe-Al IMC layer. According to recent studies [75,76], the solubility of Si in Al-Fe IMC phase is 0.8-6 wt.% as substitute atoms in the θ-$FeAl_3$ phase. When up to 10 wt.% of Si atoms participate in the intermetallic phase formation, more Si atoms can dissolve in the θ-$FeAl_3$ phase to form a supersaturated solid solution during rapid cooling [76], but this does not change the brittleness of this compound. According to Peyre *et al*. [78], the same values of hardness were obtained for pure Fe-Al IMC and Fe-Al IMC containing up to 8 at.% Si (1200 ± 100 $HV20_{mN}$).

4.3 The IMC at the Steel/Fusion Zone Interface

In the laser brazing process, most of the Al-Si coating was melted and diffused into the FZ leaving only an IMC layer of non-uniform thickness as seen at the steel/braze interface in Figure 4-7. Based on EDS analysis results, this IMC layer was found to contain 54.7±6.1 wt.% Al, 40.1±7.7 wt.% Fe, and 5.2±3.7 wt.% Mg. Based on these measurements and an XRD profile of the steel-fusion zone interface shown in Figure 4-8, the IMC was identified as predominantly θ-$FeAl_3$ with some Mg diffused into the IMC layer during laser brazing.

As shown in Figure 4-7, the thickness of the IMC layer at the FZ/steel interface varied along the interface. At the top, closest to the heat source of the laser, the IMC layer largely dissolved into the FZ leaving a very thin layer less than 2 μm (see Figure 4-7b and Figure 4-7c). However, farther down and away from the heat of the laser beam, the IMC had grown to approximately 8 μm in thickness (see Figure 4-7d). The change in the thickness of the intermetallic layers is controlled by two simultaneous phenomena: the diffusion controlled

growth of intermetallic layers and their dissolution by molten alloy [79,80]. Roulin *et al*. [81] studied the furnace brazing of steel-Al alloy dissimilar joints with Al-12Si filler metal. It was reported that the first formed phase along the steel-Al interface at 600 ˚C was a ternary Fe-Al-Si IMC with a parabolic growth rate indicating a diffusion controlled mechanism. At this temperature, dissolution of the IMC was negligible [81]. In contrast, Viala *et al*. [80] reported the formation of a Fe-Al-Si IMC at 780 ˚C during hot dipping of steel in molten Al-7Si alloy. It was reported that this IMC remained very thin (2-3 μm) at 780 ˚C due to its rapid dissolution [80]. It can be concluded that with increasing temperature, the dissolution rate of Fe-Al-Si IMC increases more rapidly than the growth rate (diffusion rate).

From these observations, the following mechanism can be proposed for change in IMC thickness along the steel-fusion zone interface from top to bottom portion of the joint. According to the binary phase diagram of Al-Si, the melting temperature of the eutectic composition coating layer (Al-12 wt.% Si) is approximately 577 ˚C. When compared to the brazing temperature of the filler metal used in this study (600~620 ˚C), the Al-Si coating layer experienced temperatures higher than its melting point during the process. Consequently, the high temperature of the process led to the melting of the Al-Si coating and also promoted dissolution of the pre-existing IMC layer between the Al-12Si coating and the steel. At the top side of the interface, the dissolution mechanism of pre-existing IMC was more dominant than the diffusion growth mechanism due to the rapid temperature increase. However, with decreasing temperatures from top towards bottom of the interface, the IMC dissolution rate in the fusion zone decreased and its growth rate increased (decreasing temperature favours the diffusion controlled growth mechanism more than the dissolution mechanism).

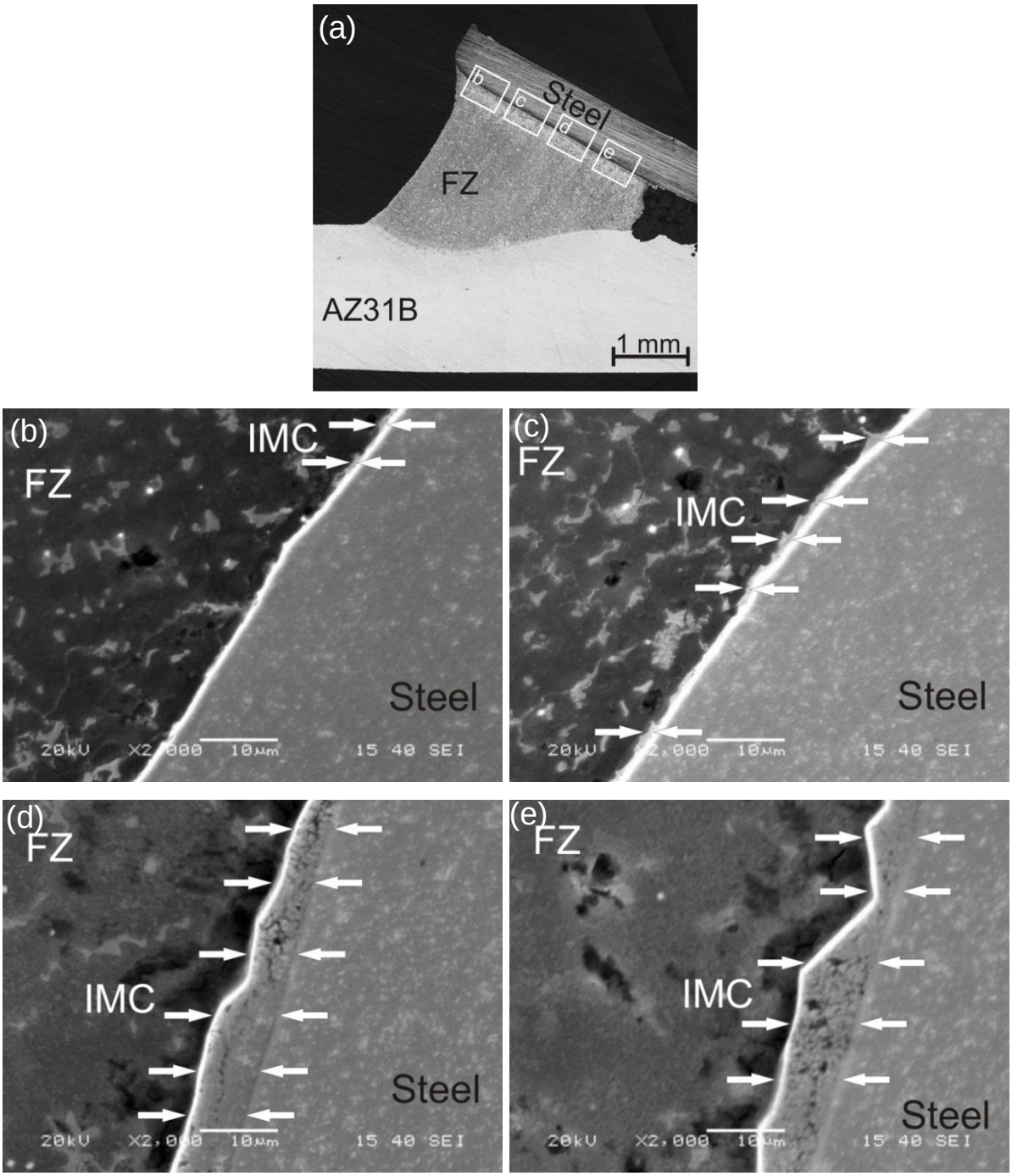

Figure 4-7: SEM images in different positions of the steel/FZ interface in (a): (b-e) IMC layer in b-e zone shown in (a).

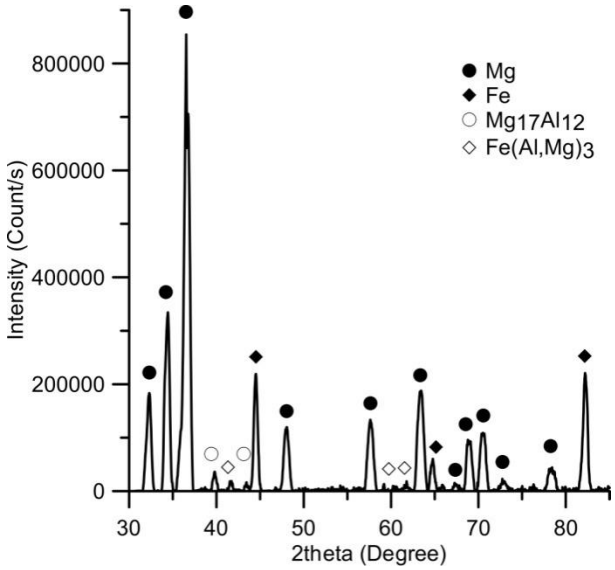

Figure 4-8: X-ray diffraction pattern of the steel-fusion zone interface of a laser brazed AZ31B-steel joint.

Representative concentrations profiles of Al, Mg, and Fe across the interface between the fusion zone and steel are shown in Figure 4-9. Fe and Al atoms diffused into the fusion zone as a result of high temperature experienced during the laser brazing process. As a result, a diffusion or transition layer formed in front of the IMC layer on the fusion zone side. According to element distributions of Fe, Al, and Mg (see Figure 4-9b), in the diffusion layer I with the thickness of almost 1.5 µm, from the FZ side to IMC side, Fe and Al contents increased gradually while the Mg content decreased rapidly. As shown in Figure 4-9a, diffusion layer I is part of the IMC, thus the formation of this diffusion layer led to growth of the IMC layer from 5 µm to 6.5 µm. The latter occurred at the bottom of the brazed joint. The main mechanism that controls the composition of this area is the time and temperature dependent diffusion process.

Another diffusion layer (diffusion layer II) is shown in Figure 4-9a on the steel side of the IMC layer between the fusion zone and the steel. The thickness of this layer was ≅ 3 µm and thus was wider than the diffusion layer I. In this layer, solid-state diffusion is believed to control the overall thickness. During diffusion of an element, the composition gradient is the

driving force that allows an element to diffuse to a place of lower concentration. As a result, for diffusion layer I, the elements Fe and Al diffused from the IMC layer to the FZ, but the diffusion direction for the Mg would be the opposite. In diffusion layer II, the IMC layer showed a higher concentration of Al and Mg as compared to steel. Consequently, the diffusion direction changed from the IMC layer to the steel side (for Al and Mg). But, Fe atoms diffused into solid solution of the IMC layer (from the steel side). The same type of diffusion layer has been observed by Miao *et al*. [82] after laser penetration brazing of Mg alloy to steel dissimilar joints.

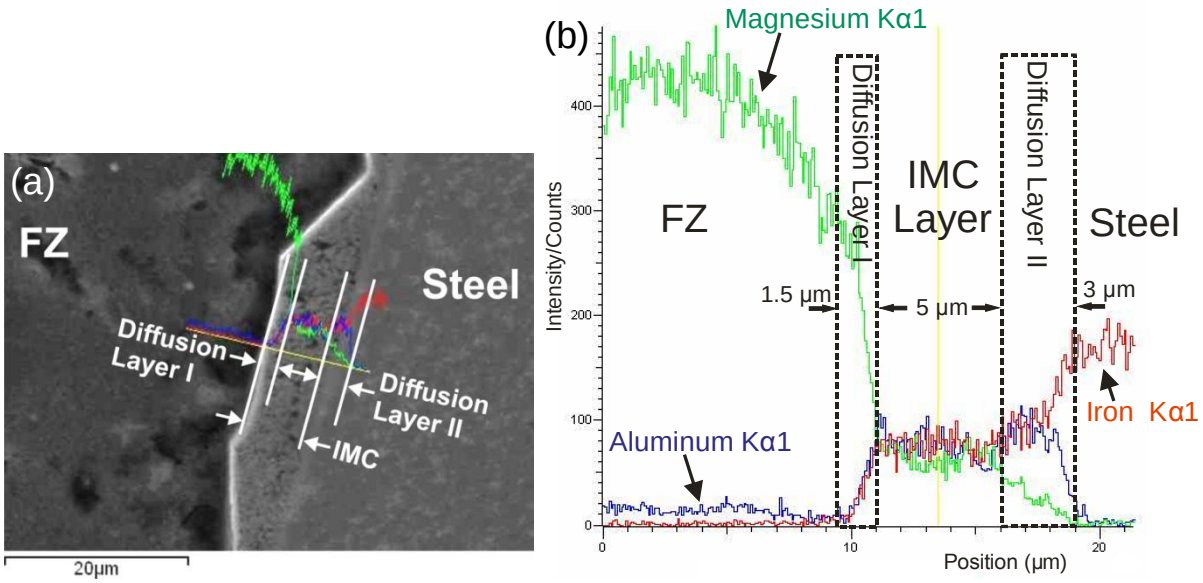

Figure 4-9: EDS composition line scans at the FZ/steel interface: (a) SEM image of the interface and (b) line scans of Al, Fe and Mg.

It is worth noting that melting of the Al-12Si coating layer during the laser brazing process not only promoted the growth of the IMC layer in the bottom portion of the interface, but also caused formation and growth of Al/Mg eutectic in the form of the divorced eutectic β-$Mg_{17}Al_{12}$ phase. Regional quantitative analysis of the chemical compositions by EDS (see Table 4-2) from the middle part of the fusion zone and also near the steel/FZ interface showed that the area near the interface contained 15.7 wt.% Al, which is more than the

11.4 wt.% Al in the middle part of the FZ. This difference is the result of the coarse β-$Mg_{17}Al_{12}$ phase near the interface as compared to the middle part of FZ.

Table 4-2: EDS analysis results of fusion zone at the middle part and at steel/coating layer interface (wt.%).

Location	Mg	Al	Fe	Zn
R1 (Near the interface)	79.5	15.7	1.9	2.9
R2 (middle part)	86.1	11.4	---	2.5

4.4 Mechanical Properties

A Vickers microhardness profile across a brazed joint was measured using 50 g load and 10 s holding time. The microhardness distribution profile is shown in Figure 4-10. The average hardnesses of the AZ31B Mg alloy and steel were 62.4±2.3 HVN and 116.3±3.4 HVN, respectively. In the fusion zone, the average hardness increased to 85.7±8.5 HVN due to the strengthening effect of the increased Al content and β-$Mg_{17}Al_{12}$ phase particles in the intergranular regions. The size of the microhardness indenter was too large to measure the hardness of the thin IMC layers formed at the interface. However, higher hardness values are expected for the IMC layer, since the reported average hardness of the θ-$FeAl_3$ phase is 700-800 HVN [83], which is much higher than the hardness of the base metals.

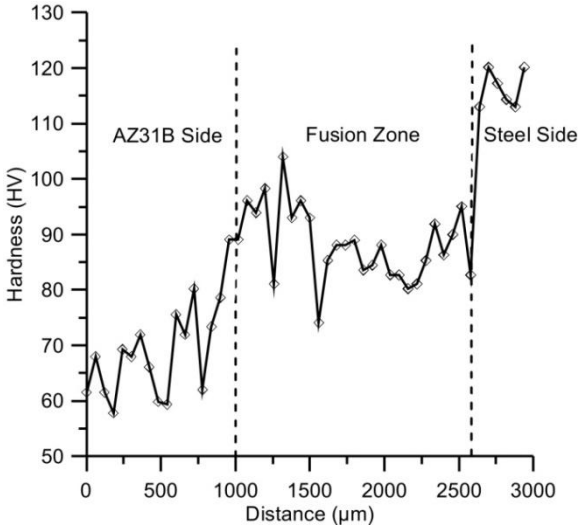

Figure 4-10: Micro-hardness profile of a laser brazed AZ31B-steel joint.

Four 50 mm long by 5 mm wide tensile specimens were cut out of each sample and tested at a tensile cross-head speed of 1 mm/min. A schematic of the tensile shear test specimen is shown in Figure 3-5a. Due to the non-symmetric configuration of the tensile test specimen, a combination of shear and tensile forces existed at the interface. Consequently, the joint strengths were reported as fracture load, since it is impossible to separate tensile and shear stresses.

The average fracture load of the laser brazed AZ31B-steel joints using Mg-Al filler metal was 767±138 N. If only the shear plane is considered, the average shear strength of the joints was 46.4±8.1 MPa, or 29±5% joint efficiency with respect to the AZ31B-H24 Mg alloy base metal. The joint efficiency values were obtained by dividing the shear strength of the laser brazed spacimen by shear strength of the AZ31B-H24 Mg alloy base metal (~ 160 MPa). The high standard deviation of the tensile shear strength in this study indicates that this laser brazing process for Al-12Si coated steel-AZ31B joints has inherent instability. This instability caused variation in the brazed depth (defined in Figure 4-2b) at different locations along the joint line, which is associated with changing actual load carrying area of the joint resulting in different tensile shear strength along the joint line. Further study is needed to improve the process stability for this dissimilar metal combination.

All tensile shear specimens fractured at the FZ-steel interface. The macro and microstructure profiles of the joint after fracture are shown in Figure 4-11. In each case, fracture initiated in the IMC layer at the bottom of the joint where the geometry of the joint created a high stress concentration area and the thickness of brittle IMC layer was also at a maximum. Then, the crack continued into the brazed FZ at the upper portion of the joint where the IMC layer was thinner. The thick layer of brittle intermetallic at the FZ/steel interface can significantly reduce the strength of the joint as any crack initiating in the layer can easily propagate through this continuous sheet of brittle material [84]. From these observations, the type and thickness of the IMC layer determined the joint strength. At the bottom of the joint, the thickness of the IMC layer was more than 8 μm which significantly degraded the mechanical strength of the joints. At the upper portion of the joint, the crack

deviated into the FZ and propagated along the grain boundaries of the brazed metal due to existence of β-$Mg_{17}Al_{12}$ phase in the grain boundaries. Therefore, the tensile shear properties and the thickness of the IMC layer appeared to dictate the overall strength of the joints.

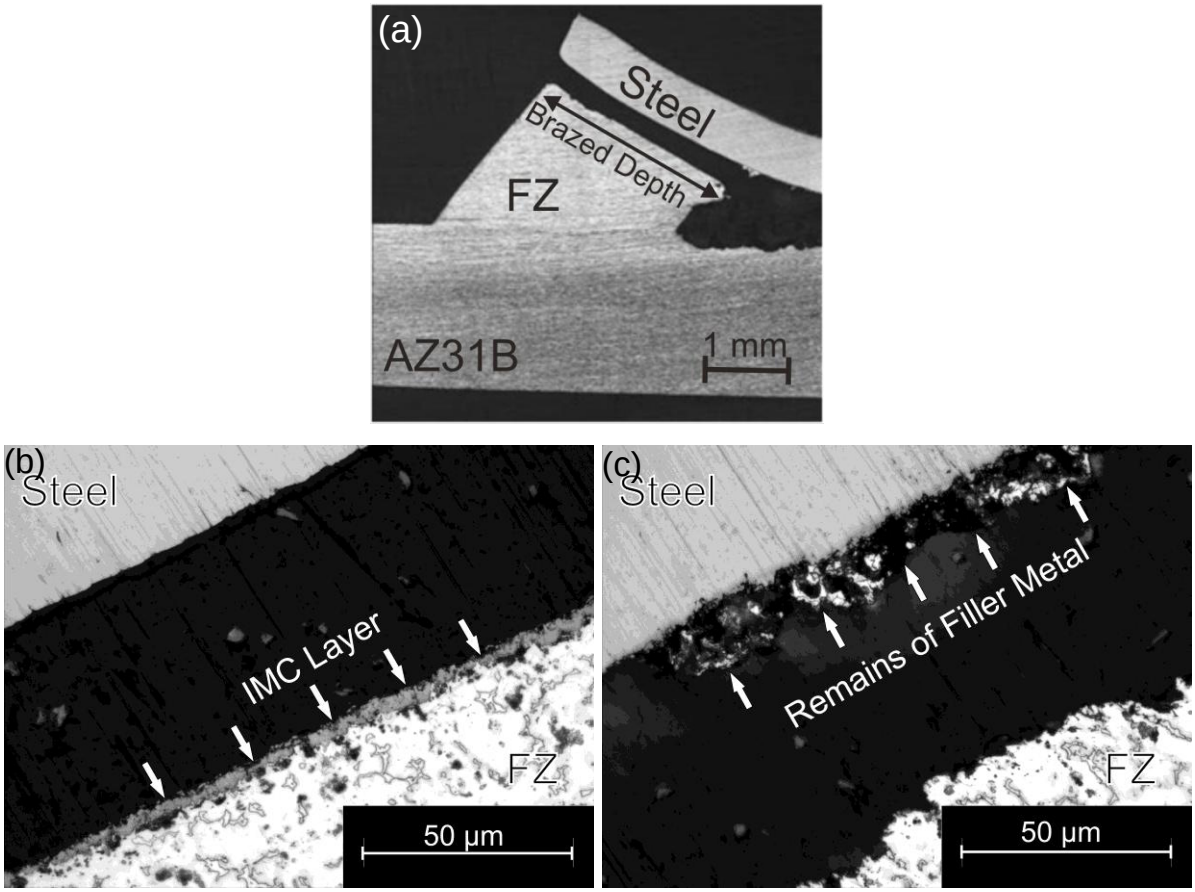

Figure 4-11: Fracture location of the tensile shear test specimen, (a) fractured specimen, (b) crack propagation in bottom side of the joint, and (c) crack propagation in upper side of the joint.

Figure 4-12 and Figure 4-13 show SEM images of typical fracture surfaces of the fusion zone and steel sides after tensile shear testing, respectively. The fracture morphologies indicate mixed characteristics of brittle and ductile fracture. At the upper side of the joints (region 1 in Figure 4-12a for the FZ side and region 1 in Figure 4-13a for steel side), where

the crack propagated into the fusion zone, non-uniform ductile fracture was observed (Figure 4-12b and Figure 4-13b). Meanwhile, at the bottom side of the fracture surface (regions 3 in Figure 4-12a and Figure 4-13a), where the crack formed in the IMC layer, evidence was seen of more brittle cleavage fracture as shown in Figure 4-12d and Figure 4-13d. In the middle of the fracture surface (regions 2 in Figure 4-12a and Figure 4-13a), an area was observed where the fracture surface contained both ductile and brittle fracture characteristics (see Figure 4-12c and Figure 4-13c). This area is called the transition zone from ductile to brittle fracture modes.

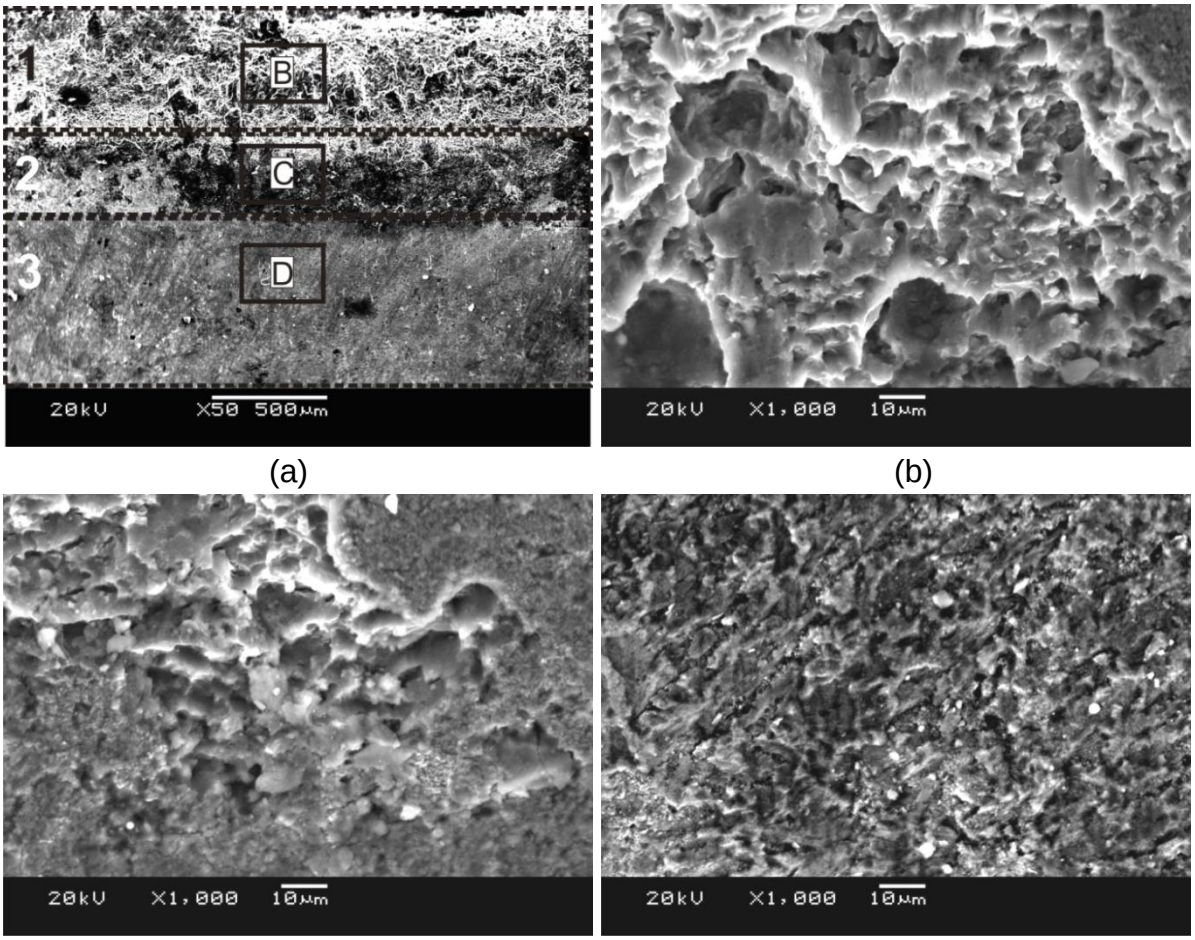

Figure 4-12: SEM images of typical fracture surface of fusion zone side after tensile shear test, (a) fusion zone side including: (b) top of the surface indicated by B, (c) middle of the surface indicated by C, and (d) bottom of the surface indicated by D.

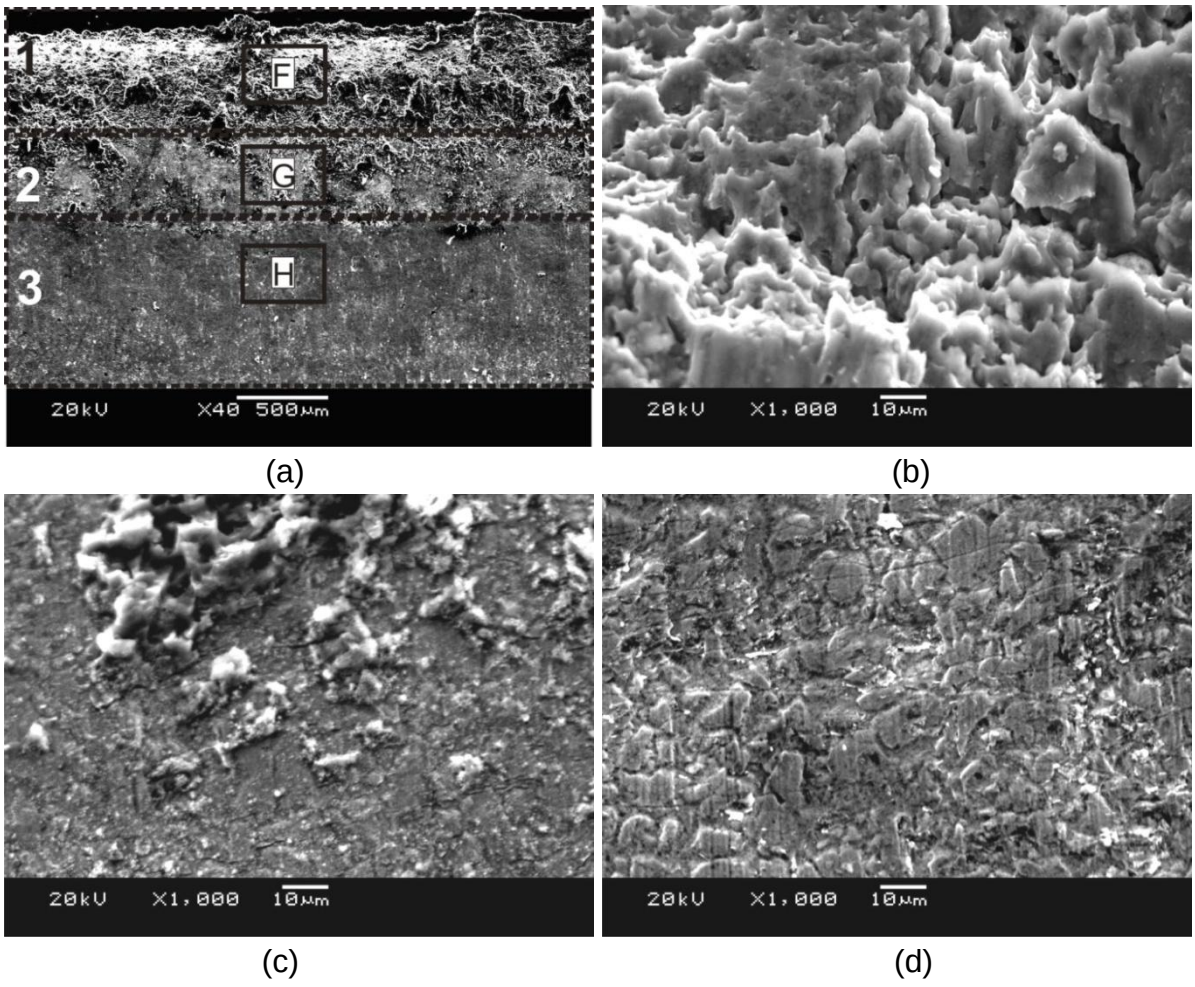

Figure 4-13: SEM images of typical fracture surface of steel side after tensile shear test, (a) steel side including: (b) top of the surface indicated by F, (c) middle of the surface indicated by G, and (d) bottom of the surface indicated by H.

Table 4-3: EDS analysis results of different locations on the fracture surface shown in Figure 4-12a and Figure 4-13a (wt.%)

Element	Fusion Zone Side			Steel Side		
	Top (B)	Middle (C)	Bottom (D)	Top (F)	Middle (G)	Bottom(H)
Mg, Ka	90.18	68.88	18.05	90.01	32.69	-
Al, Ka	9.82	21.00	59.96	9.99	29.57	20.98
Fe, Ka	-	10.12	21.98	-	37.74	79.02

EDS analysis results of the fracture surfaces of both steel and FZ sides are shown in Table 4-3. At the top of the fracture surface (region B in Figure 4-12a for the FZ side and region F in Figure 4-13a for the steel side), the composition was similar to the FZ. This implied that the crack propagated into the FZ in the upper portion of the joint. In contrast, at the bottom area of the fracture surface (regions D in Figure 4-12a and H in Figure 4-13a), the compositions corresponded to the Fe-Al IMC layer indicating that the crack in this region propagated along the IMC layer adjacent to the steel.

4.5 Lattice Matching Analysis of the Interfaces

The importance of lattice matching along the adjoining lattices of Mg-reaction product(s)-steel interfaces in the interfacial energy, which affects both bond strength and the wetting, was discussed in Sections 2.5.3 and 2.6. To correlate between lattice matching and mechanical strength of the laser brazed joints, the lattice matching between two sides of different observed interfaces in this study was theoretically investigated using an edge-to-edge crystallographic matching model [85,86].

For each of the observed interfaces in this study, one interface, which is the intersection plane of the matching planes, forms in between the phase and the substrate. This plane consists of a series of matched atom rows. In order to minimize the strain energy at the interface, the interatomic spacing misfit along the matching direction should be minimized [85]. The strain energy at the interface is also affected by the interplanar spacing (*d*-value) mismatch between the matching planes [85]. During phase formation (*e.g.*, formation of $FeAl_3$ between Mg and Fe), to minimize the free energy of the system, the system tries to find matching planes with small *d*-value mismatch.

To further study the interatomic spacing misfit along matching directions and the interplanar spacing mismatch between matching planes for the different interfaces, the edge-to-edge crystallographic model developed by Zhang and Kelly [85,86] was used. In this matching model, the matching directions and matching planes are the close or nearly close-

packed directions and planes [85,86]. The interatomic misfit and interplanar mismatch between two phases can be calculated by:

$$\delta = \frac{|\Delta a_0|}{a_0} \tag{4.1}$$

where Δa_0 is difference between interatomic or interplanar spacings of the two phases and a_0 is the interatomic or interplanar spacing of the substrate for a specific direction or plane [85,86]. The calculation procedure and the results of the interatomic spacing misfits along matching directions and interplanar spacing mismatches between matching planes for different formed interfaces in this study are given in the Appendix, Section A.1.

Using an Al-12Si interlayer between the Mg alloy and steel resulted in formation of θ-$FeAl_3$ IMC layer at the Mg alloy-steel interface after the laser brazing process [69]. Therefore, the theoretical analysis of the lattice matching in the Mg-$FeAl_3$-Fe system using the edge-to-edge matching model was performed (see Section A.1). The calculated minimum interplanar mismatches were 16.2% $_{\{Mg\text{-}FeAl3\}}$-1.5% $_{\{FeAl3\text{-}Fe\}}$. These results showed that no possible pair of planes between Mg and $FeAl_3$ was found to form an OR with low mismatch strain in their adjoining lattices. Therefore, high mismatch strain energy along the Mg-$FeAl_3$ interface and very low mismatch strain energy along $FeAl_3$-Fe interface were found. Despite low interfacial strength of the Mg-$FeAl_3$ interface, the low fracture toughness of $FeAl_3$ reaction product dictated the fracture of the joint [69].

4.6 Chapter Summary

The current chapter detailed development of a diode laser brazing procedure for joining AZ31B-H24 Mg alloy sheet to aluminum coated cold rolled carbon steel sheet in the single flare bevel lap joint configuration using a Mg-Al based filler wire. In this process, the Mg-Al based filler metal and a shallow surface layer of the Mg alloy sheet were melted simultaneously by a diode laser beam, while no melting of the steel sheet occurred. The results of this study suggest that feasibility of this process depends strongly on the pre-existing Al-12Si coating layer on the steel sheet that promotes wetting of the Mg-Al filler

alloy as well as formation of a layer of θ-$Fe(Al,Si)_3$ intermetallic compound along the braze/steel interface. From the middle part of the braze/steel interface to the root of the joint, the Al-Si layer melted and mixed into the braze alloy and the intermetallic layer grew up to 8 μm thick. From the middle part of the braze/steel interface to top of the joint, both the Al-Si and the intermetallic layer were dissolved. These two simultaneous phenomena led to an intermetallic layer with non-uniform thickness ranging from 0 to 8 μm along the braze/steel interface. The average fracture load of the joint was 767 N, representing 29% joint efficiency with respect to the AZ31B-H24 Mg alloy base metal. Failure occurred when cracks propagated along the intermetallic layer starting at the root of the bevel joint and moved into the braze metal at the upper part of the joint. To further study the interplanar spacing mismatch between matching planes for the formed different interfaces in this study, an edge-to-edge crystallographic model was used. According to the obtained results from this model, when $FeAl_3$ phase forms as the reaction product along the Mg-steel interface, an interface with high mismatch strain energy and low bond strength will form between the Mg and the $FeAl_3$ reaction layer.

Laser brazing of Al-12Si coated steel sheet to AZ31B Mg alloy has been successfully performed. However, a pre-existing layer of brittle θ-$FeAl_3$ along the braze-steel interface was found to degrade the mechanical properties of the joint as failure of the joint always occurred by fracture of this brittle intermetallic layer. Therefore, further studies were required to improve the joints efficiencies. Based on the data available in the literature, Ni was chosen as another potential interlayer alloy between the steel and Mg alloy to improve mechanical strength of the laser brazed steel-Mg alloy joints. The following chapter includes the theoretical results of a thermochemical analysis of the phases likely to form at the interface of a Mg alloy-Ni-plated steel joint during laser brazing as well as the experimental results of the laser brazing of AZ31B Mg alloy to Ni electro-plated steel sheet.

Chapter 5

Laser Brazing of AZ31B to Ni Electro-Plated Steel Sheet

In order to predict early stage phase formation in the Mg alloy-interlayer-steel system during the laser brazing process, the thermodynamic stability of precipitated phases at the Mg alloy-Ni-steel interface during laser brazing of Ni-plated steel to AZ31B magnesium sheet using AZ92 magnesium alloy filler wire has been evaluated using FactSage thermochemical software [87]. Ni interlayer was chosen with the purpose of the joint strength improvement. The results will provide better understanding of the phases that might form at the interface of the dissimilar metal joints during the laser brazing process. To confirm these theoretical results, the brazeability of AZ31B-H24 magnesium alloy and steel sheet with a microlayer of electro-deposited Ni in a single flare bevel lap joint configuration has been investigated [88]. The macro- and microstructure, element distribution, and interfacial phases of the joints were studied by optical microscopy, scanning electron microscopy, transmission electron microscopy, and X-ray diffraction [88]. The work presented and described in this chapter has been previous published by Nasiri *et al*. [87,88].

5.1 The Thermochemical Model

It is well-known that welding conditions are far from equilibrium conditions. However, useful estimations can be obtained from thermodynamic models provided that one looks at "local equilibrium". This assumption is supported by the fact that a liquid state, with high rates of mass transfer, is present in most welding processes. In this study, prediction of early stage phase formation along the steel-Ni-Mg alloy interface was done in two steps. In the first step, with the assumption of full local equilibrium during cooling after the local maximum temperature has been reached, all phases that could possibly form in the steel-Ni-Mg alloy system for a range of temperature and composition were predicted. It was assumed that the time is very short due to fast heating and cooling rate during the laser brazing process, so mass transfer is constrained to short distances. In the second step, amongst all the phases that could possibly form, the phase most likely to precipitate first from the liquid at

one specific temperature and composition was identified by finding which phase has the highest driving force to form from the liquid phase.

A schematic diagram of the thermochemical model domain that includes the interface between the Ni-plated steel sheet and the AZ92 Mg brazing alloy is shown in Figure 5-1a. In order to find the phases that might form in this steel-Ni-Mg alloy system at different temperatures during laser brazing, a ternary system consisting of the steel alloy, Ni interlayer and Mg alloy (filler metal composition) was defined. Its composition field is presented on a Gibbs triangle in Figure 5-1b. Since the temperature of the laser brazing process is less than the melting temperature of the steel [88], the steel stays in solid-state during this process. Therefore, it was assumed that if the steel participates in any reaction by dissolving into the fusion zone close to the interface, the maximum content of the steel in this system will be low. Thus, the maximum content of the steel alloy in the steel-Ni-Mg alloy system was assumed to be about 10 wt. % as indicated by the dotted tie line in Figure 5-1b. In practice, the assumption is that the entire Ni layer can potentially react with the molten AZ92 filler, and the mass of potentially reacting steel components is estimated to be equal to 10 % of the mass of the Ni layer. The sensitivity of the predicted results to this assumed value was evaluated by performing the same analysis using a lower value of 5 wt.% steel. The results confirmed that in this range, the assumed percentage of steel does not change the predicted results as very similar phase stability maps were generated.

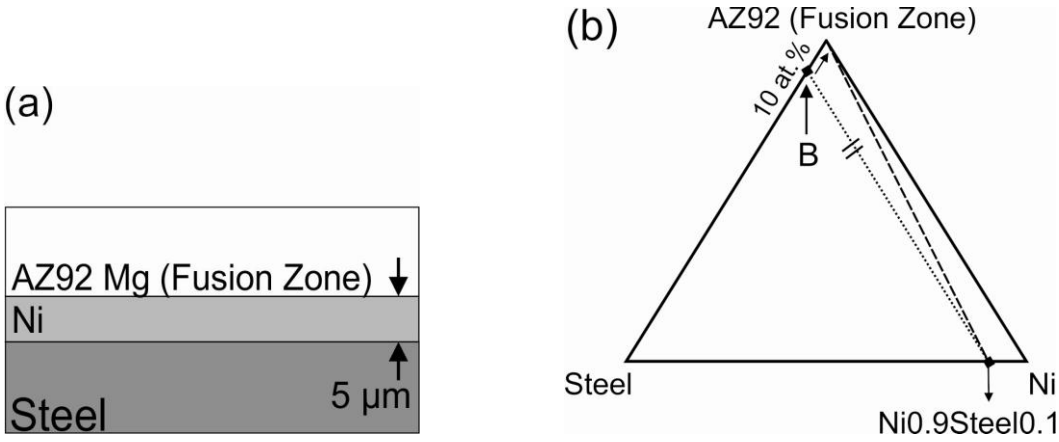

Figure 5-1: (a) Schematic of the interface between the Ni plated steel sheet and the AZ92 Mg brazing alloy and (b) steel-Ni-Mg alloy ternary system defined in this study.

In the laser brazing process, melting of the filler metal by the laser beam occurs initially, since the laser is focused on the filler metal. Following this, partial or full dissolution of the Ni interlayer may occur, but very little of the steel components (Fe-C-Mn) should dissolve as their solubility in Mg-Al-Zn is small. Therefore, immediately after melting of the filler metal and before dissolution of the Ni interlayer into the fusion zone, the steel is not in contact with the fusion zone (see Figure 5-1a). However, point B on the steel-Ni-Mg alloy ternary system (Figure 5-1b) shows that steel and the AZ92 Mg filler metal (FZ) can be in contact with each other. For this reason, point B was moved to the top corner of the ternary system. Therefore, instead of the dotted line in Figure 5-1b, the dashed line was considered as a tie line corresponding to a (10 wt.% Steel-Ni)-Mg alloy pseudo-binary system during the laser brazing process.

5.2 Thermochemical Analysis Procedure

The Phase Diagram module of the commercial thermochemical analysis code FactSage [56] was used first to generate ternary isothermal sections (in wt.%) in the steel-Ni-Mg alloy system at different temperatures from 873 K (600 °C) to 1373 K (1100 °C). The results are shown in Figure 5-2a-f. The zero-phase fraction lines for $AlNi_{(s)}$, $Al_3Ni_{5(s)}$, and $Mg_2Ni_{(s)}$ are shown. The position of the dashed line in the phase diagrams of Figure 5-2a-f shows which phases are predicted to form under local equilibrium conditions during laser brazing at one specific temperature. For example, at 873 K (600 °C) and 973 K (700 °C), Al_3Ni_2, AlNi, Mg_2Ni, and Al_3Ni_5 are predicted to form. However, from 1073 K (800 °C) to 1373 K (1100 °C), AlNi is the only intermetallic compound that is predicted to form and all other phases are no longer stable.

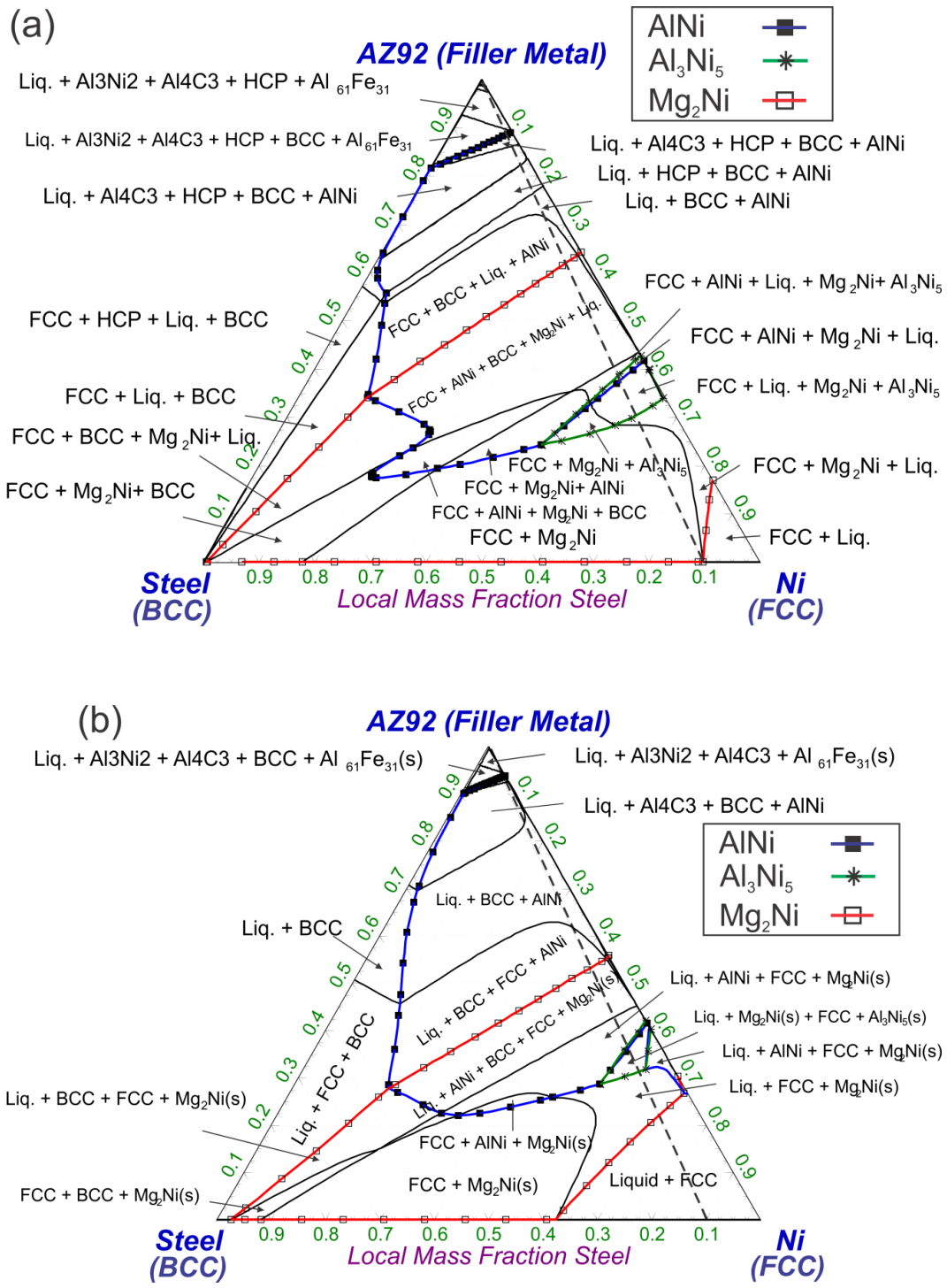

Figure 5-2: Predicted steel-Ni-AZ92 Mg alloy ternary system at (a) 873 K (600 ºC), (b) 973 K (700 ºC), (c) 1073 K (800 ºC), (d) 1173 K (900 ºC), (e) 1273 K (1000 ºC), and (f) 1373 K (1100 ºC).

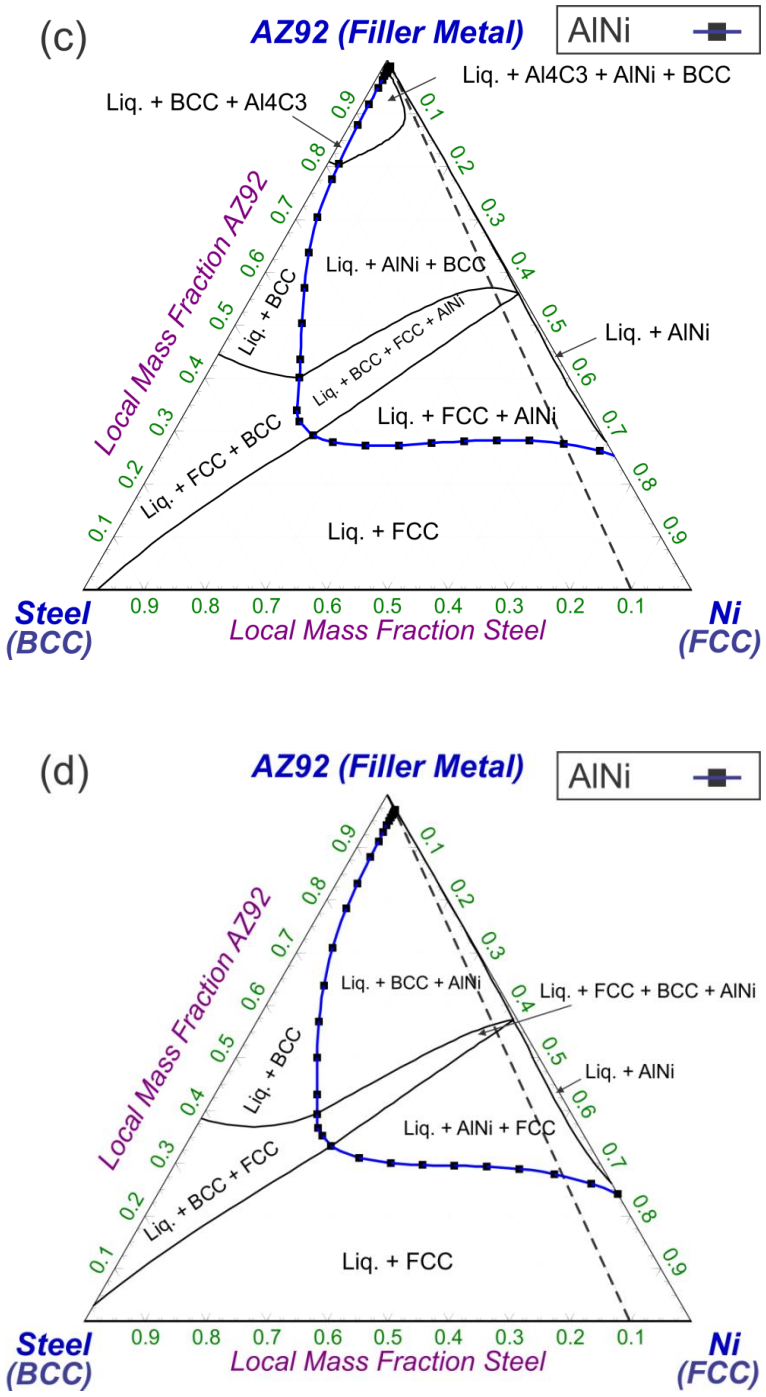

Figure 5-2: Predicted steel-Ni-AZ92 Mg alloy ternary system at (a) 873 K (600 ºC), (b) 973 K (700 ºC), (c) 1073 K (800 ºC), (d) 1173 K (900 ºC), (e) 1273 K (1000 ºC), and (f) 1373 K (1100 ºC).

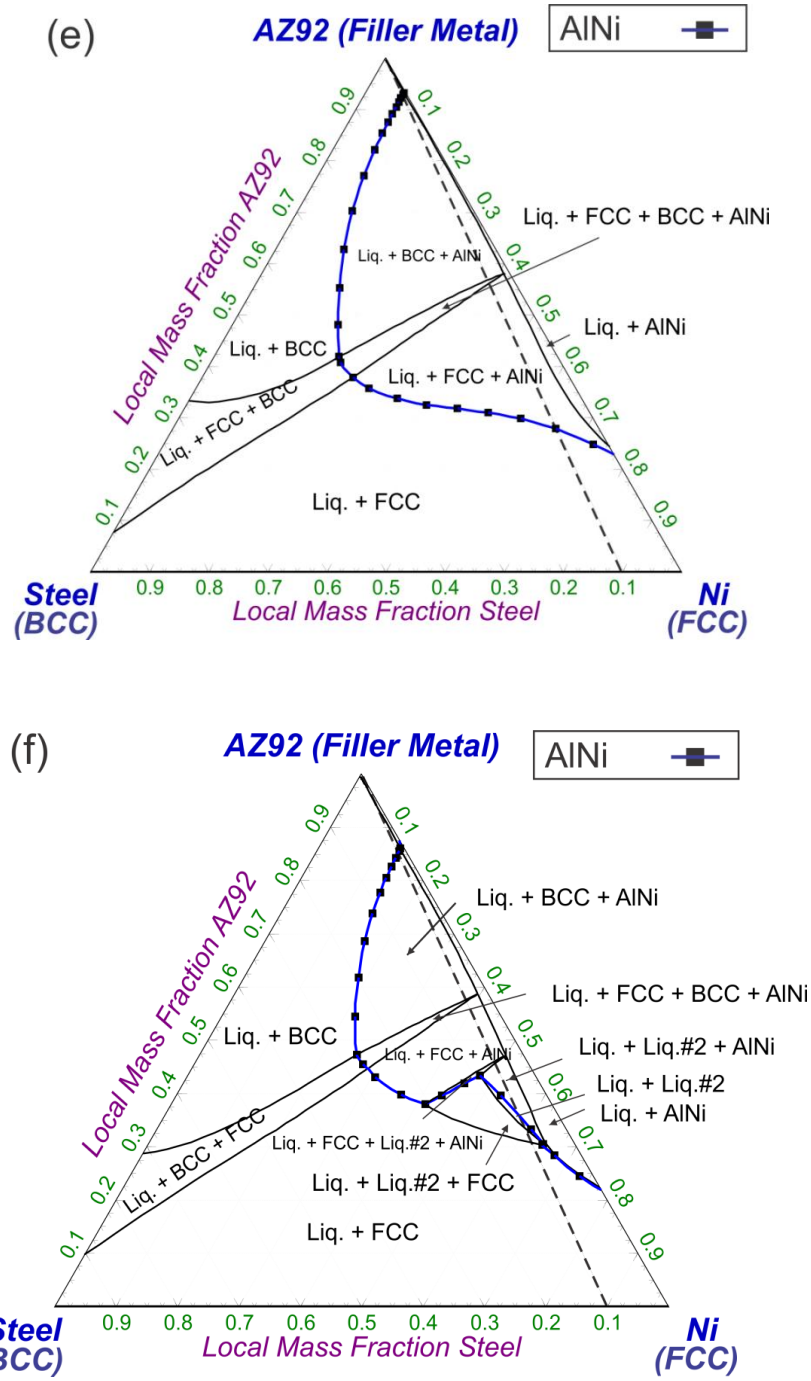

Figure 5-2: Predicted steel-Ni-AZ92 Mg alloy ternary system at (a) 873 K (600 ºC), (b) 973 K (700 ºC), (c) 1073 K (800 ºC), (d) 1173 K (900 ºC), (e) 1273 K (1000 ºC), and (f) 1373 K (1100 ºC).

Since each dashed line in Figure 5-2a-f is a mass constrain between the AZ92 filler metal and the $Ni_{0.9}Steel_{0.1}$ compositions at a specific temperature, the phases predicted to exist along this line over the temperature range of 873 K (600 °C) to 1373 K (1100 °C) can be used to construct a pseudo-binary system between the AZ92 and the $Ni_{0.9}Steel_{0.1}$ versus temperature as shown in Figure 5-3. Figure 5-3 is the calculated isoplethal section (T vs. wt.%) along the dashed line in Figure 5-2a-f. This diagram was used to identify the phases that might form along the steel-Ni-Mg alloy interface at different temperatures during laser brazing. These phases are Al_3Ni, Al_3Ni_2, AlNi, Mg_2Ni, and Al_3Ni_5. All of these phases are binary phases, but may include some minor solubility of a third element. In the next step, the procedure used for finding the first phase most likely to precipitate from the liquid at a specific temperature and composition is explained.

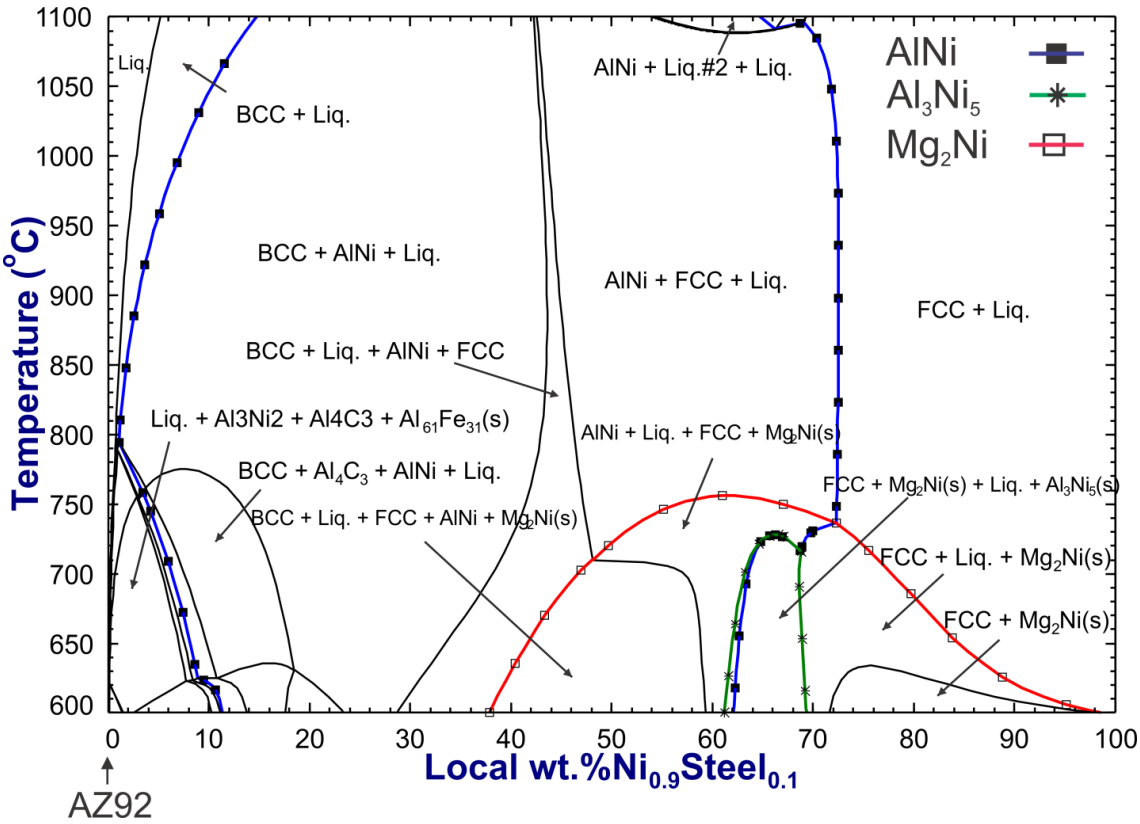

Figure 5-3: Predicted AZ92 (filler metal)-$Ni_{0.9}Steel_{0.1}$ pseudo-binary phase diagram showing the phases that might form along the steel-Ni-Mg alloy interface.

By expressing the composition of a solid phase in the form of a binary compound A_xB_y, the possible reaction for formation of this compound from the liquid in the steel-interlayer (Ni)-Mg alloy system in the laser brazing temperature range can be given as follows:

$$x[A]+y[B]\longrightarrow A_xB_{y(s)} \tag{5.1}$$

In order to evaluate the stability of the possible precipitated phases, it is important to have a reliable calculation for the change of Gibbs free energy, ΔG, of the reaction shown in Eq. (5.1). A negative ΔG indicates that the reaction will proceed spontaneously to the right, whereas a positive ΔG indicates that the reaction shown in Eq. (5.1) will proceed spontaneously from right to left.

The standard Gibbs free energy change with the formation of a solid phase from pure liquid components (given as [A] and [B]) (ΔG^o) indicated in Eq. (5.1) can be determined using [89]:

$$\Delta G^o_{T,(A_xB_y)} = -RT\ln\frac{a(A_xB_y)}{a^x([A])a^y([B])} \tag{5.2}$$

where R is the Universal Gas constant, T is absolute temperature (K), and a is the chemical activity of each phase. For 1 mole of the elements, we have,

$$\frac{x}{x+y}[A]+\frac{y}{x+y}[B]\longrightarrow\frac{1}{x+y}A_xB_{y(s)} \tag{5.3}$$

and, therefore,

$$\Delta G^o_{T,(A_{x/x+y}B_{y/x+y})} = -RT\ln\left(\frac{a(A_xB_y)}{a^x([A])a^y([B])}\right)^{\frac{1}{x+y}} \tag{5.4}$$

After local fusion of the "system", for a given local temperature and local composition, which fixes the chemical activity of [A] and [B] in the liquid state, the chemical activity of $A_xB_{y(s)}$ can be computed when $\Delta G^o_{(T)}$ is known (from the databases). At equilibrium, if $[a(A_xB_y)]^{1/x+y} > 1$, then A_xB_y should form spontaneously. The stability and driving force for formation of the phase increase with increasing activity. Therefore, the first precipitated phase from the liquid at a specific temperature and composition will be the phase with the

maximum activity value, but only if this activity is greater than unity. This concept can be used when there are many possible phases predicated and we are not really sure which, if any, will form. Considering the phases that might form along the steel-Ni-Mg alloy interface, for 1 mole of the system, the following reactions and net change in free energy are possible:

0.75 mole Al + 0.25 mole Ni will form 0.25 mole of Al_3Ni

with a change of Gibbs free energy of:

$$\Delta G^{o}_{T,(Al_{3/4}Ni_{1/4})} = -RT\ln\left(\frac{a(Al_3Ni)}{a^3([Al])a([Ni])}\right)^{\frac{1}{4}} \tag{5.5}$$

Similarly,

0.60 mole Al + 0.40 mole Ni will form 0.20 mole of Al_3Ni_2

with a change of Gibbs free energy of:

$$\Delta G^{o}_{T,(Al_{3/5}Ni_{2/5})} = -RT\ln\left(\frac{a(Al_3Ni_2)}{a^3([Al])a^2([Ni])}\right)^{\frac{1}{5}} \tag{5.6}$$

0.50 mole Al + 0.50 mole Ni will form 0.50 mole of AlNi

with a change of Gibbs free energy of:

$$\Delta G^{o}_{T,(Al_{1/2}Ni_{1/2})} = -RT\ln\left(\frac{a(AlNi)}{a([Al])a([Ni])}\right)^{\frac{1}{2}} \tag{5.7}$$

0.375 mole Al + 0.625 mole Ni will form 0.125 mole of Al_3Ni_5

with a change of Gibbs free energy of:

$$\Delta G^{o}_{T,(Al_{3/8}Ni_{5/8})} = -RT\ln\left(\frac{a(Al_3Ni_5)}{a^3([Al])a^5([Ni])}\right)^{\frac{1}{8}} \tag{5.8}$$

and

0.666 mole Mg + 0.333 mole Ni will form 0.333 mole of Mg_2Ni

with a change of free energy of

$$\Delta G^{o}_{T,(Mg_{2/3}^{\ }Ni_{1/3}^{\ })} = -RT\ln\left(\frac{a(Mg_2Ni)}{a^2([Mg])a([Ni])}\right)^{\frac{1}{3}} \tag{5.9}$$

The component activities were evaluated using the Equilib module of FactSage [56] at different laser brazing temperatures. The activity-composition diagrams for Al_3Ni, Al_3Ni_2, AlNi, Mg_2Ni, and Al_3Ni_5 from 873 K (600 ºC) to 1373 K (1100 ºC) are shown in Figure 5-4. At 873 K (600 ºC) and 973 K (700 ºC), Al_3Ni_2, AlNi, and Mg_2Ni are predicted to be the first precipitated phases from the liquid at different composition ranges (mass fraction of $Ni_{0.9}Steel_{0.1}$). Note that the composition here should be seen as an approximated position between the filler (x = 0) and an initial position within the steel just next to the Ni-steel interface (x = 1), where the mass ratio of Ni to steel is roughly 10 to 1. In the temperature range of 1073-1373 K (800-1100 ºC), AlNi is predicted to be the first and only precipitated phase from the liquid. Using this calculation procedure, a phase stability map, shown in Figure 5-5, was plotted indicating the first precipitated phases from the liquid at different temperatures and compositions during the laser brazing process. This stability map suggests that at temperatures higher than 873 K (600 ˚C), immediately adjacent to the $Ni_{0.9}Steel_{0.1}$ (*i.e.*, when $x \rightarrow 1$, on the steel side), there will likely be a layer of liquid very rich in $Ni_{0.9}Steel_{0.1}$ at most temperatures. When the temperature of this liquid drops below about 998 K (725 ˚C), Mg_2Ni will likely form between the $Ni_{0.9}Steel_{0.1}$ and the AlNi. When the $Ni_{0.9}Steel_{0.1}$ composition of the AZ92 liquid drops below about 0.72 mass fraction, AlNi will likely form over a large composition range (0.02-0.72 mass fraction of $Ni_{0.9}Steel_{0.1}$). At temperatures higher than 1048 K (775 ˚C), when the mass fraction of $Ni_{0.9}Steel_{0.1}$ in the liquid drops below 0.02 to 0.15 further away from the interface, the liquid will be mostly AZ92. When the temperature drops below about 1048 K (775 ˚C), there may be a thin band of Al_3Ni_2 form between the AlNi and the AZ92 filler metal. Note that on Figure 5-4a and b the chemical activity of Al_3Ni_2 is barely greater than the one of AlNi, suggesting a very small difference of driving forces for forming these phases from the liquid solution.

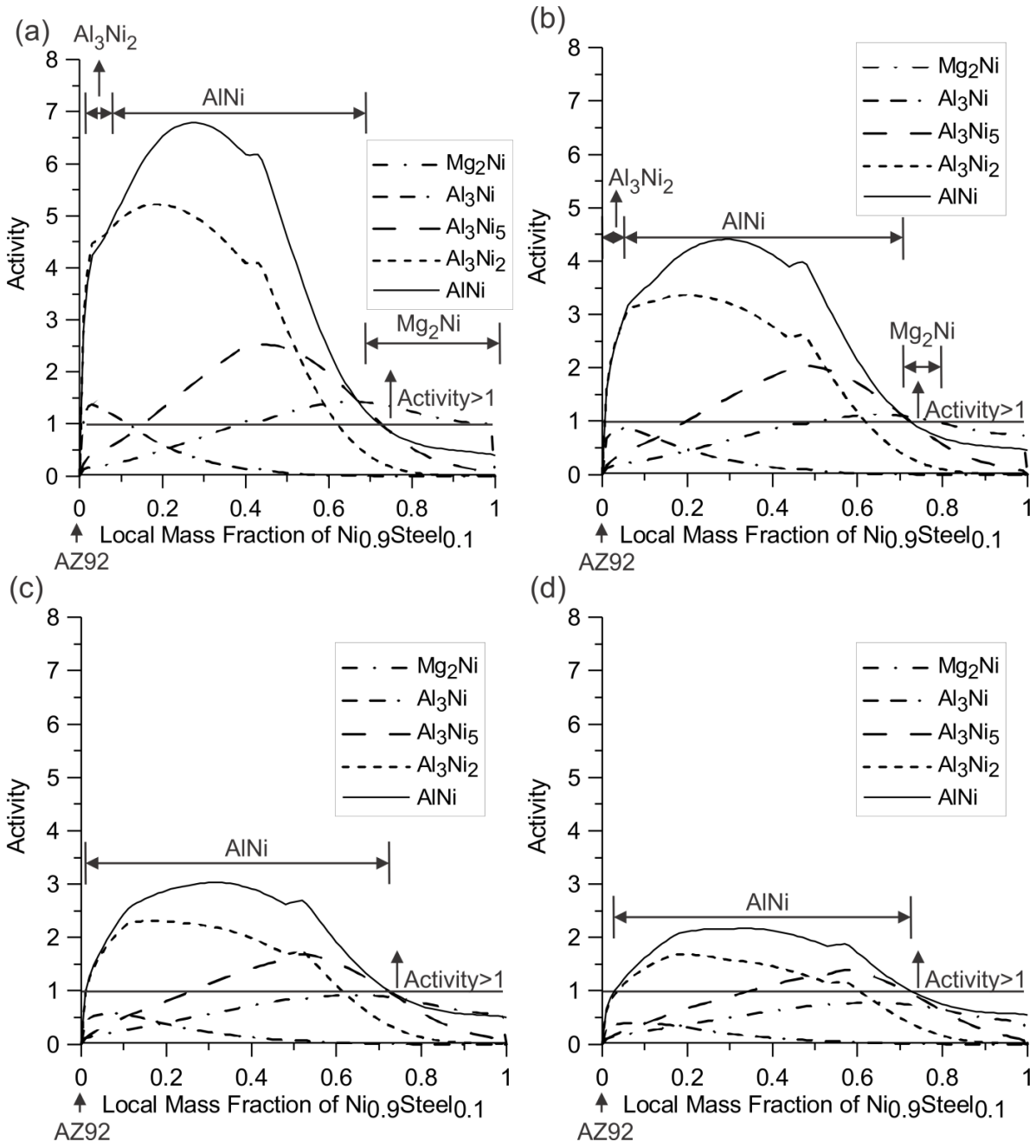

Figure 5-4: The activity-composition diagrams for AlNi, Al_3Ni_2, Al_3Ni_5, Al_3Ni, and Mg_2Ni at (a) 873 K (600 ºC), (b) 973 K (700 ºC), (c) 1073 K (800 ºC), (d) 1173 K (900 ºC), (e) 1273 K (1000 ºC), and (f) 1373 K (1100 ºC).

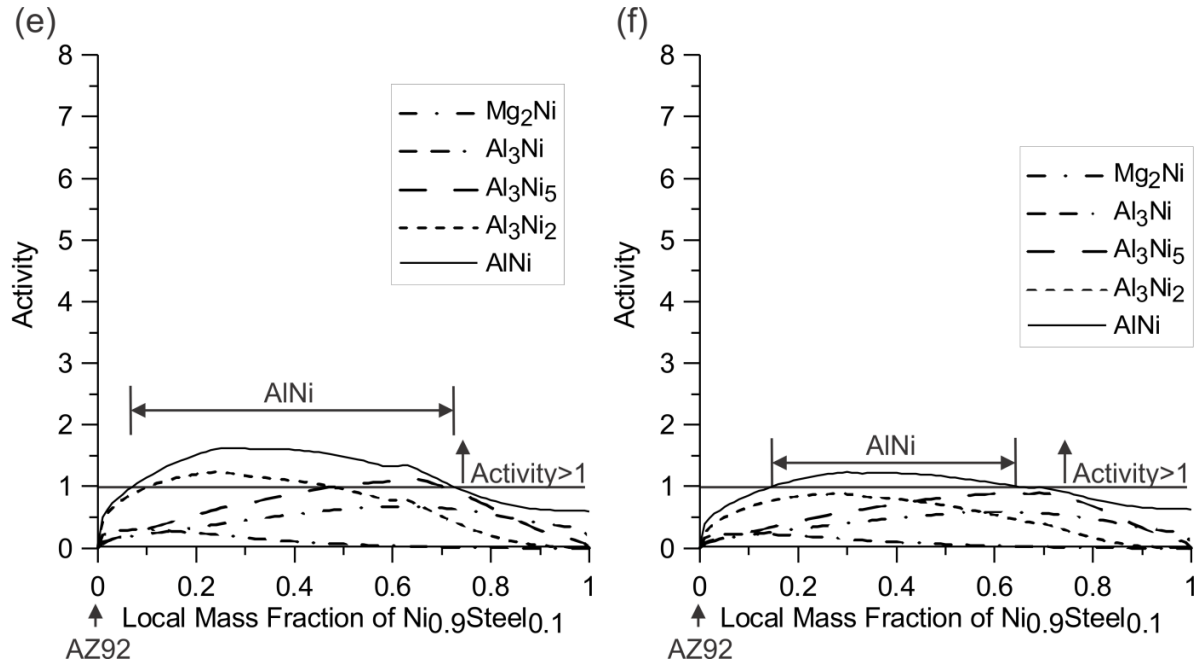

Figure 5-4: The activity-composition diagrams for AlNi, Al_3Ni_2, Al_3Ni_5, Al_3Ni, and Mg_2Ni at (a) 873 K (600 ºC), (b) 973 K (700 ºC), (c) 1073 K (800 ºC), (d) 1173 K (900 ºC), (e) 1273 K (1000 ºC), and (f) 1373 K (1100 ºC).

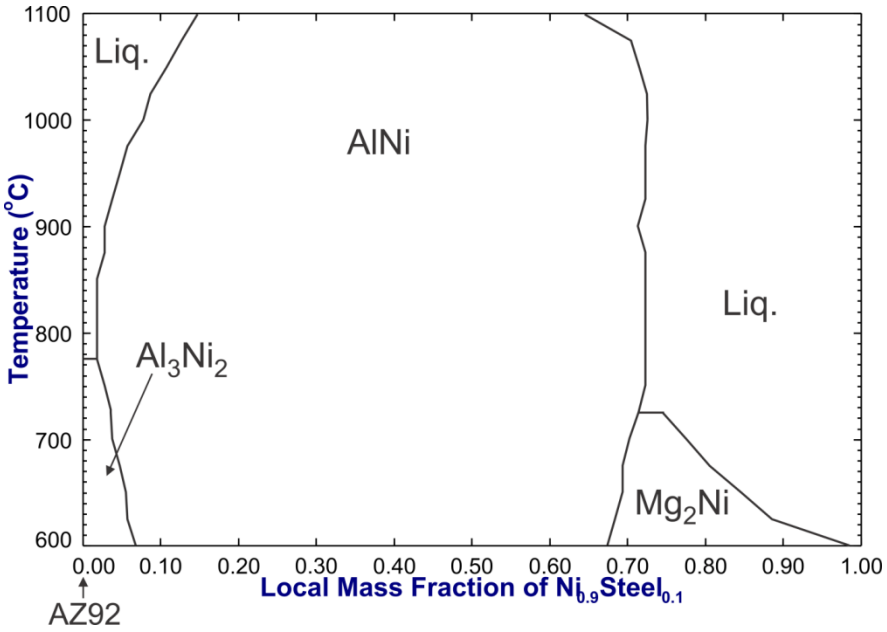

Figure 5-5: Phase stability or pseudo-binary phase diagram showing the phases predicted to precipitate first from the liquid at different temperatures and compositions during the laser brazing process.

In order to validate the thermodynamic predictions for the steel-Ni-AZ92 system, laser brazing experiments with single flare bevel lap joints between plain low carbon steel sheet with a 5 µm thick Ni electro-deposited layer and AZ31B-H24 magnesium alloy sheet using a AZ92 Mg alloy filler metal were performed.

5.3 Experimental Results and Discussion

A photograph of a laser brazed Ni electro-plated steel/AZ31B joint and a typical cross-sectional view of the joint are shown in Figure 5-6. This brazed joint was made using 2.2 kW laser power, 8 mm/s travel speed, and 0.2 mm beam offset to the steel side. The joint exhibited a uniform brazed area with good wetting of both base materials. Partial melting of the AZ31B base metal was observed. The 5.5 µm thick Ni electro-deposited layer on the surface of the steel significantly improved the wetting of the steel by molten Mg-Al filler metal. Detailed microstructural analysis of the fusion zone and AZ31B Mg alloy after the laser brazing process has been reported in the previous chapter [69]. This section will focus on microstructural analysis of the steel-fusion zone interface.

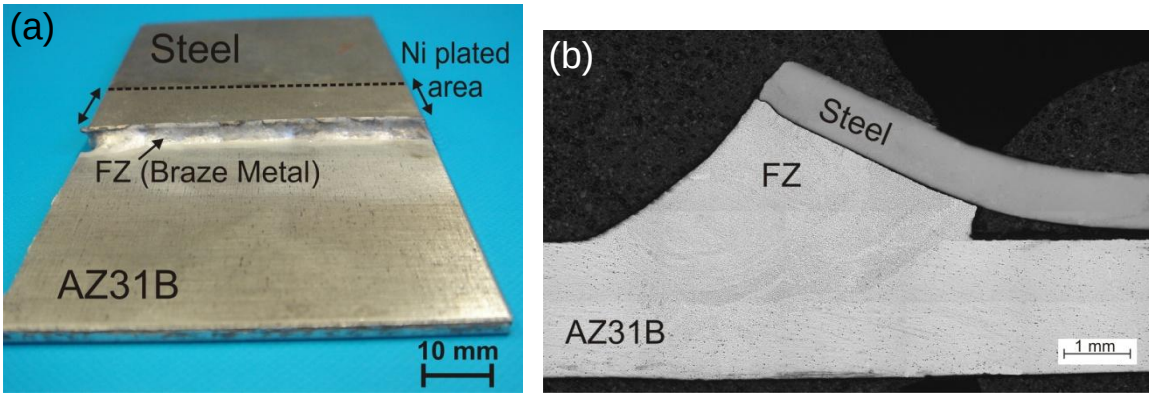

Figure 5-6: A laser brazed Ni electro-plated steel/AZ31B joint made using 8 mm/s travel speed and 2.2 kW laser beam power: (a) top bead and (b) transverse section of the joint.

5.3.1 Microstructural Evolution along the Steel-FZ Interface

Figure 5-7 shows the microstructure at different locations of the steel-FZ interface. The Ni coating was not detected as a separate layer along the interface after the LBP which would suggest that it had entirely melted and gone into solution in the liquid immediately adjacent to the interface. It was observed that the microstructure of the FZ-steel interface changed significantly across the FZ-steel interface from the bottom (Position A, Figure 5-7b) to top (Position F, Figure 5-7e) side of the joint. In order to explain this change of microstructure during the laser brazing process, temperature distribution along the interface versus time was measured during laser brazing using two thermocouples, one attached to the top side and the other to the bottom side of the steel sheet (see Figure 3-4a). According to the measured temperature profiles shown in Figure 5-8, the steel sheet experienced maximum temperatures of 1151.1 ˚C and 652.7 ˚C on the top and the bottom side, respectively. Therefore, a 500 ˚C temperature gradient was measured between the top and the bottom side of the steel sheet during the laser brazing process, since the laser beam was focused on the top of the filler wire, as shown in Figure 3-4a. This temperature difference and gradient across the joint interface during the laser brazing process is believed to be the main reason for the prominent change of microstructure across the FZ-steel interface.

As shown in Figure 5-7b, at the bottom of the interface, a few diamond-shaped bright phases were formed near the steel-FZ interface. In order to identify these phases, a TEM foil was prepared from position B of Figure 5-7a. Figure 5-9 shows the TEM images, EDS plot, and selected area diffraction pattern (SADP) of these submicron particles. The diffraction pattern shows a standard diffraction pattern of AlNi (with BCC structure) with [011] zone axis of the particle. According to an EDS analysis of the diamond-shaped bright phases shown in Figure 5-7b, the composition of the particles was 49.6±1.3 at.% Ni, 45.4±4.7 at.% Al, and 5.0±2.5 at.% Mg thus confirming that the diamond shaped particles were mainly composed of AlNi intermetallic compound (IMC). Representative concentration profiles of Ni, Al, and Mg across one AlNi particle are shown in Figure 5-9d which indicates that a trace amount of magnesium was found in this particle. It has been reported that each of the Al-Ni binary intermetallics has some solubility for substitutional magnesium atoms [90].

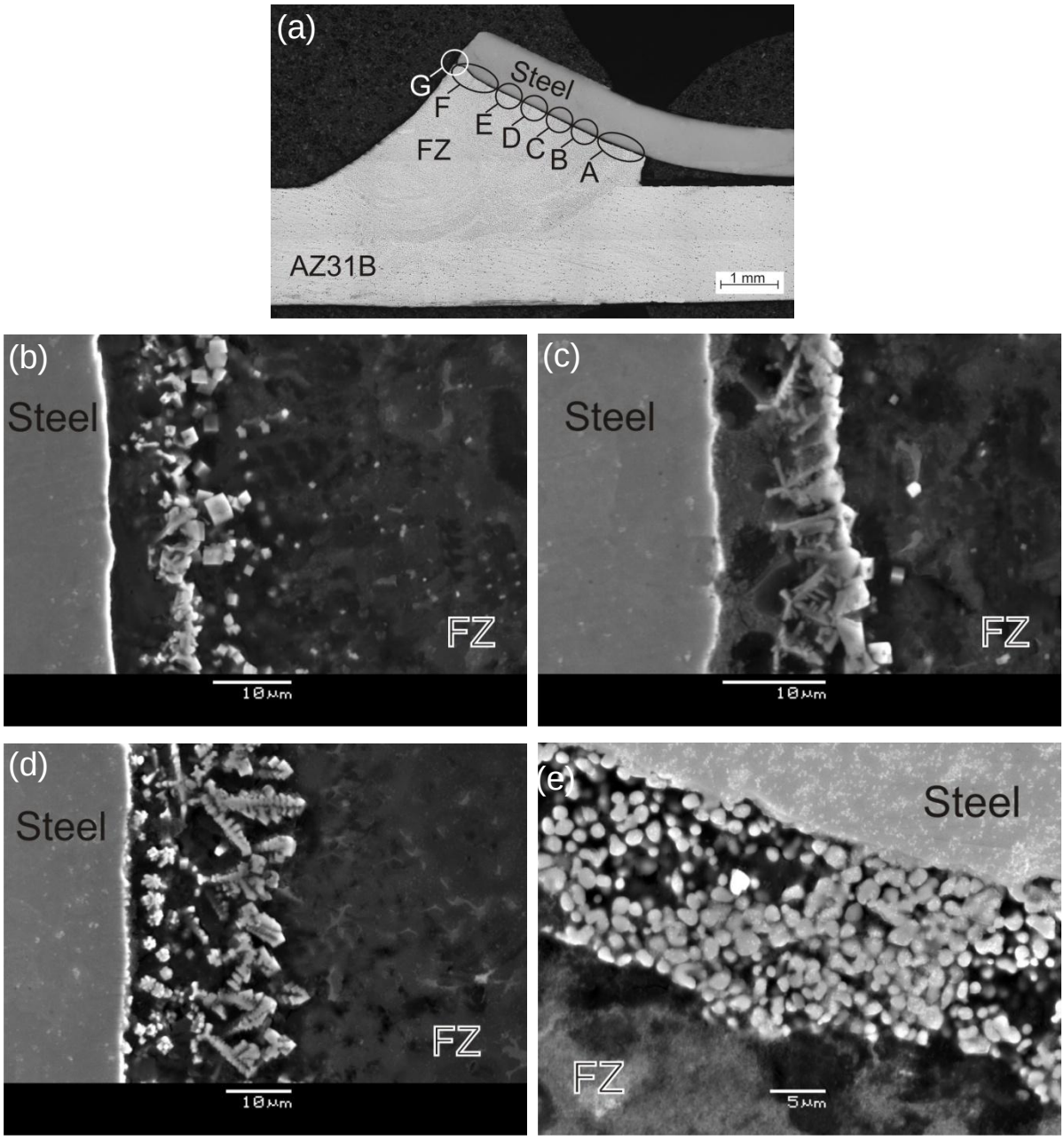

Figure 5-7: Transverse sections of a laser brazed joint: (a) optical micrograph of the entire joint and SEM images in different positions of steel-FZ interface shown in (a): (b) position A, (c) position C, (d) position E, and (e) position F.

Figure 5-10 shows the XRD spectra obtained from the middle of the steel-FZ interface. The area covered by the X-ray beam was a 300 µm diameter circle. This XRD result

confirmed the existence of AlNi IMC, Fe, β-$Mg_{17}Al_{12}$, and α-Mg. The AlNi IMC compound was not found at the middle of the FZ area, whereas the XRD pattern in Figure 5-10 showed some weak peaks suggesting that AlNi IMC had formed mainly at the steel-FZ interface.

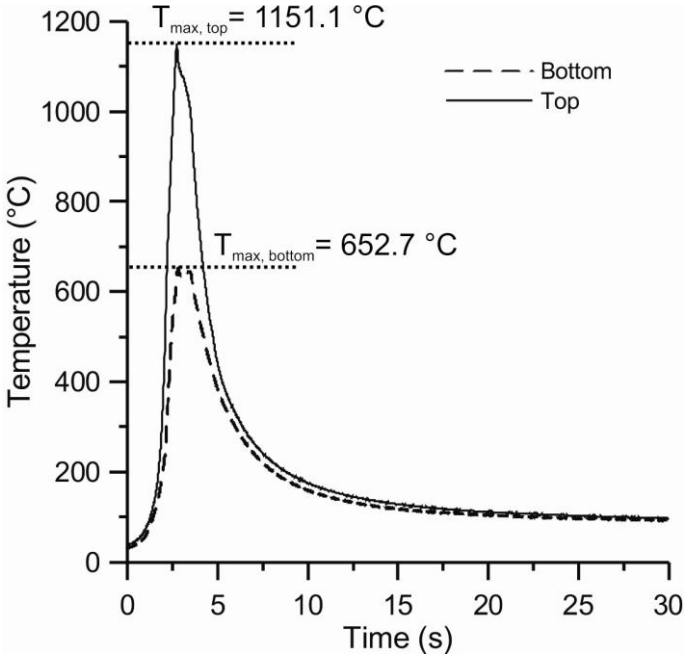

Figure 5-8: Typical temperature versus time profiles measured during laser brazing at the top and bottom side of the joint.

It was observed that upon moving from the bottom to the middle of the interface, which was associated with increasing temperature, the morphology of the IMC phase along the interface changed from the diamond shaped AlNi to a faceted dendritic shaped phase (see Figure 5-7c and Figure 5-7d). EDS analysis results indicated this dendritic phase contained 43.0±1.6 at.% Ni, 52.1±2.0 at.% Al, and 4.9±0.5 at.% Mg. This composition again corresponded with AlNi IMC phase. In this area, the first precipitated phase from the liquid was AlNi IMC, the same as at the bottom of the joint. This phase grew steadily in a faceted dendritic shape. As the interface temperature increased with moving from position A to position E in Figure 5-7a, the growth morphology of the AlNi phase changed from diamond-

shaped to a facetted dendritic shape, as demonstrated in Figure 5-7d. Continuous growth of the AlNi was observed in this area with some dendrites having long secondary dendrite arms (see Figure 5-7d).

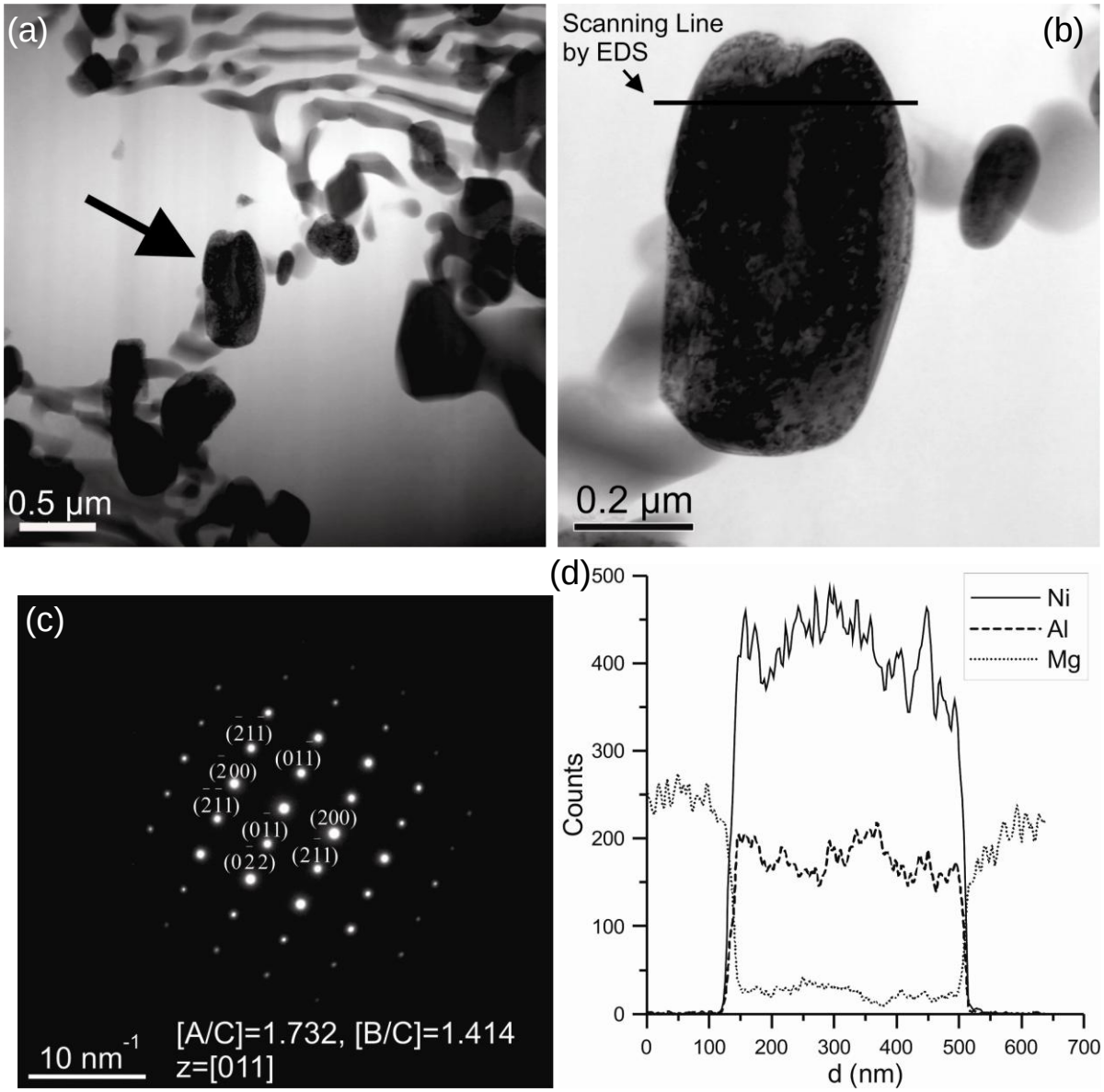

Figure 5-9: AlNi particle characterization at position B shown in Figure 4a: (a) and (b) TEM images, (c) SADP in the [011] zone axis of this particle, and (d) EDS composition line scans across an AlNi particle indicating line scans of Ni, Al, and Mg.

At the top of the joint (position F in Figure 5-7a), the morphology of the interfacial phase changed further and a high volume fraction of a particle-like phase with the composition of 48.4±1.4 at.% Ni, 50.1±1.2 at.% Al, and 1.5±0.4 at.% Mg was detected (Figure 5-7e). This phase was also found to be AlNi IMC phase. It should also be noted that formation of the AlNi phase consumed almost all of the Al content of the melt near the steel-FZ interface. Thus, no β-$Mg_{17}Al_{12}$ was observed near the interface compared with the central part of the FZ.

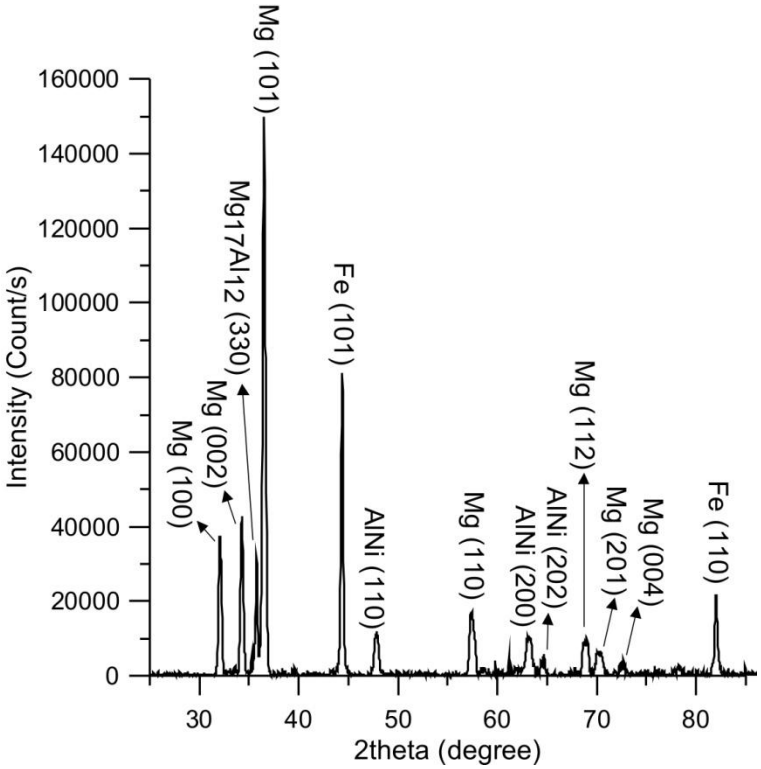

Figure 5-10: X-ray diffraction pattern of the steel-FZ interface.

5.3.2 Solidification of the Remaining Melt between the AlNi IMC Phase and the Steel

At the bottom of the joint, AlNi IMC first crystallized from the liquid close to the interface and then supersaturated α-Mg solid solution containing 10.6 ± 3.6 at.% Ni, 3.2 ± 1.7 at.% Al, and 2.9 ± 1.5 at.% Fe (dark regions in Figure 5-7b and Figure 5-11) solidified from the liquid

during cooling along with the AlNi phase. In some locations between the bottom and middle of the interface, some gray lamellar phases, as shown in Figure 5-11c and Figure 5-12, were also observed between the AlNi IMC layer and the steel. Figure 5-12a shows the position of AlNi precipitates with respect to the steel-fusion zone interface in the prepared sample during FIBing for TEM analysis. Figure 5-12b and c show TEM images of this lamellar (plate-like) phase. According to EDS analysis, the white lamellae corresponded to α-Mg and the dark lamellae containing 27.6 ± 7.2 at.% Ni and 72.3 ± 7.3 at.% Mg represented the Mg_2Ni stoichiometric intermetallic compound (also confirmed by SADP analysis). Based on these results, these two phases next to each other are the Mg-Mg_2Ni lamellar eutectic.

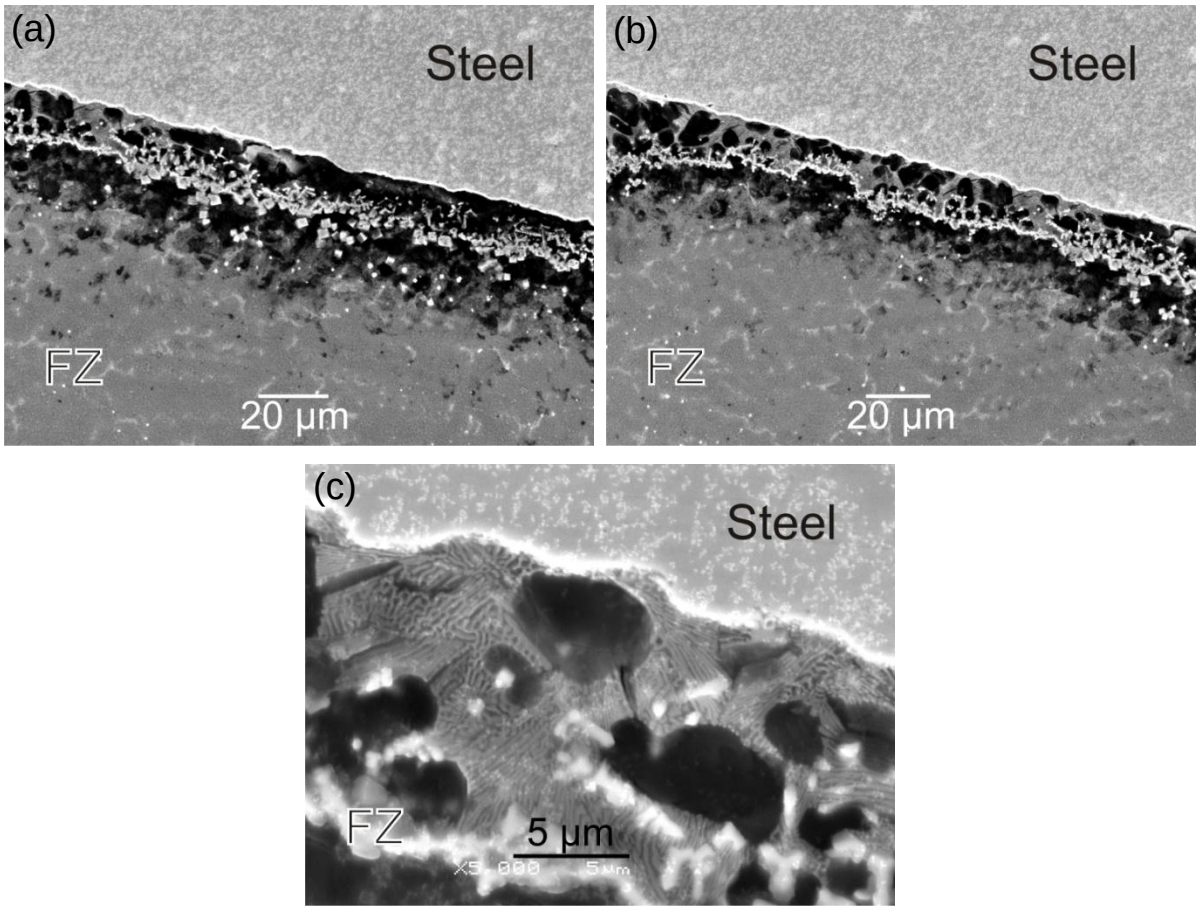

Figure 5-11: SEM images of the steel-FZ interface show the solidification morphology of remaining melt between IMC layer and the steel side: (a) position A in Figure 5-7a near bottom side, (b) position B in Figure 5-7a, and (c) Mg-Mg_2Ni eutectic phases.

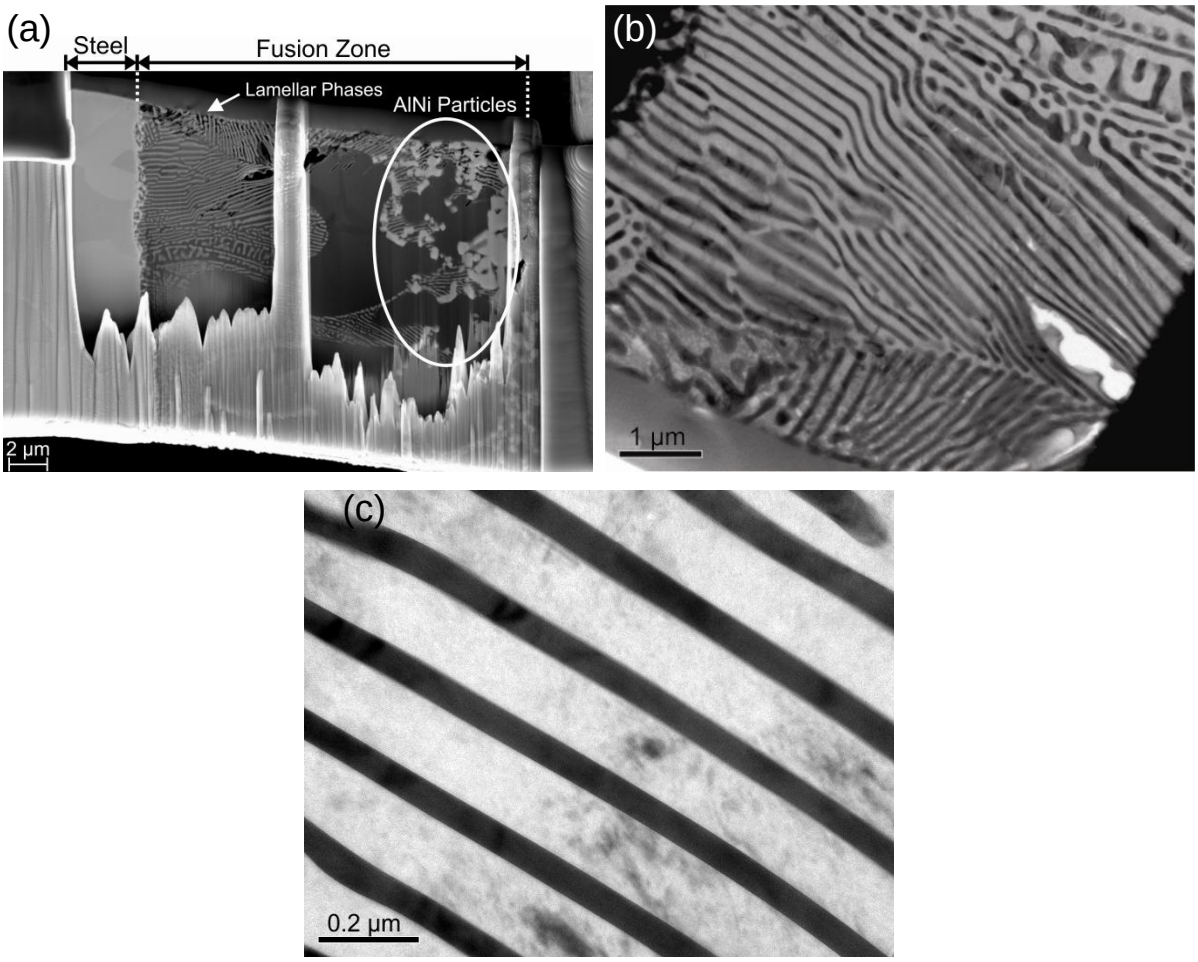

Figure 5-12: (a) TEM sample attached to a copper grid, (b) and (c) TEM images of the lamellar phases formed along the steel-FZ interface.

Formation of the Mg-Mg_2Ni lamellar eutectic was not uniform and continuous along the interface. As shown in Figure 5-11a and b, in some locations between the steel and the AlNi IMC layer, Mg_2Ni crystallized in the form of a lamellar gray phase and in other locations it was not seen and a dark solid solution of Mg containing small amounts of Ni, Al, and Fe was formed. In the middle portion of the interface, the AlNi phase crystallized first in the liquid (Figure 5-7d). Then, dark α-Mg solid solution containing 5.8 ± 2.1 at.% Ni, 1.2 ± 0.3 at.% Al, and 3.1 ± 0.5 at.% Fe formed during cooling along with AlNi phase. Finally, at the top of the joint, the AlNi phase precipitated heavily in the liquid along the interface and

then the remaining liquid solidified during cooling in the form of α-Mg solid solution (containing 2.4 ± 0.6 at.% Ni, 0.3 ± 0.1 at.% Al, and 3.4 ± 0.3 at.% Fe) along with and among AlNi particles (see Figure 5-7e). Upon moving from the bottom to the top of the interface, the Fe content of the remaining liquid between AlNi IMC and the steel increased from 2.9 to 3.4 at.% due to more diffusion of Fe from the steel side to the FZ at higher temperature. In contrast, Al and Ni showed opposite behaviours due to an increase in the thickness of AlNi IMC from the bottom to the top portion of the joint (from 5 to 30 μm).

5.3.3 Comparison with the Theoretical Results

These experimental results have confirmed the formation of dendritic AlNi IMC and also α-Mg + Mg_2Ni phases along the interface at the bottom of the joint (Figure 5-11), where measured temperatures during the process were close to 973 K (700 ºC), and just a dendritic AlNi phase along the interface at the middle and top side of the joint (Figure 5-7d and e), where the measured temperatures were more than 1073 K (800 ºC). These experimental results are in agreement with the predicted phase stability map shown in Figure 5-5 at 973 K (700 ºC) and more than 1073 K (800 ºC).

The Al_3Ni_2 IMC that was predicted to form by the thermochemical analysis was not detected along the steel/FZ interface after the laser brazing process. According to Al-Ni binary phase diagram, Al_3Ni_2 forms after formation of AlNi as a result of a peritectic reaction. Since this reaction proceeds much more slowly than monotectic reactions (formation of AlNi) or eutectic reactions (formation of α-Mg + Mg_2Ni) [92], the very fast cooling rates experienced during the laser brazing process must prevent the formation of this phase. Therefore, some additional features must be taken into account when attempting to predict phase formation in a complex system based on such thermochemical calculations. While useful estimations and predictions can be obtained from thermodynamic models based on the assumption of local equilibrium, when dealing with welding and brazing processes, the high cooling rates and solute microsegregation that takes place during solidification can lead to many non-equlibrium effects. For instance, some phases that are not stable in the

equlibrium condition, may become stable as a result of solute enrichment during solidification. Second, the calculations do not consider phase transformation kinetics. When trying to predict the microstructure or possible formed phases the kinetics of the phase transformation should also be considered. Some kinetic calculations based on a diffusion-controlled mechanisms tied in with the computational thermodynamic approach are possible with available software [91].

5.3.4 Transition Layer

Based on the TEM analysis, the AlNi phase did not grow on the steel substrate, but instead nucleated and grew in the liquid adjacent to the interface and was surrounded by either α-Mg + Mg_2Ni eutectic phases or just α-Mg phase close to the interface. On the other hand, while it may appear in Figure 5-11 that all of the electroplated Ni had melted and gone into solution in the liquid and that the α-Mg may have nucleated and grown from the steel surface, it is well known that Mg and Fe are an immiscible couple. From a crystallographic point of view, it is not possible for magnesium to nucleate on steel due to the very large lattice mismatching of Fe and Mg [60]. Therefore, another layer or phase must be responsible for bonding between the steel and fusion zone.

Further high magnification microstructural analysis of the steel-fusion zone interface was performed by TEM to find an explanation for the observed interfacial phases. Figure 5-13a shows a TEM image of the steel-fusion zone interface. A continuous nano-interlayer (50-200 nm thick) phase was observed along the interface, which was bonded to the steel side on one side and to the fusion zone on the other side. Higher magnification of this layer (as shown in Figure 5-13b) confirmed good coherency between this layer and steel as well as the fusion zone. According to EDS point analysis, the Ni content of the transition layer varied between 17 at.% and 40 at.%. Figure 5-13c shows the selected area diffraction pattern (SADP) on the transition layer that identified it as Fe(Ni) solid solution with face centered cubic (FCC) structure. The lattice parameter of Fe(Ni) was calculated to be a = 3.650 $Å$,

which is similar to the lattice parameter of Ni (a_{Ni} = 3.516 $\AA$). Thus, the crystal structure and the lattice parameter of Fe(Ni) were similar to Ni.

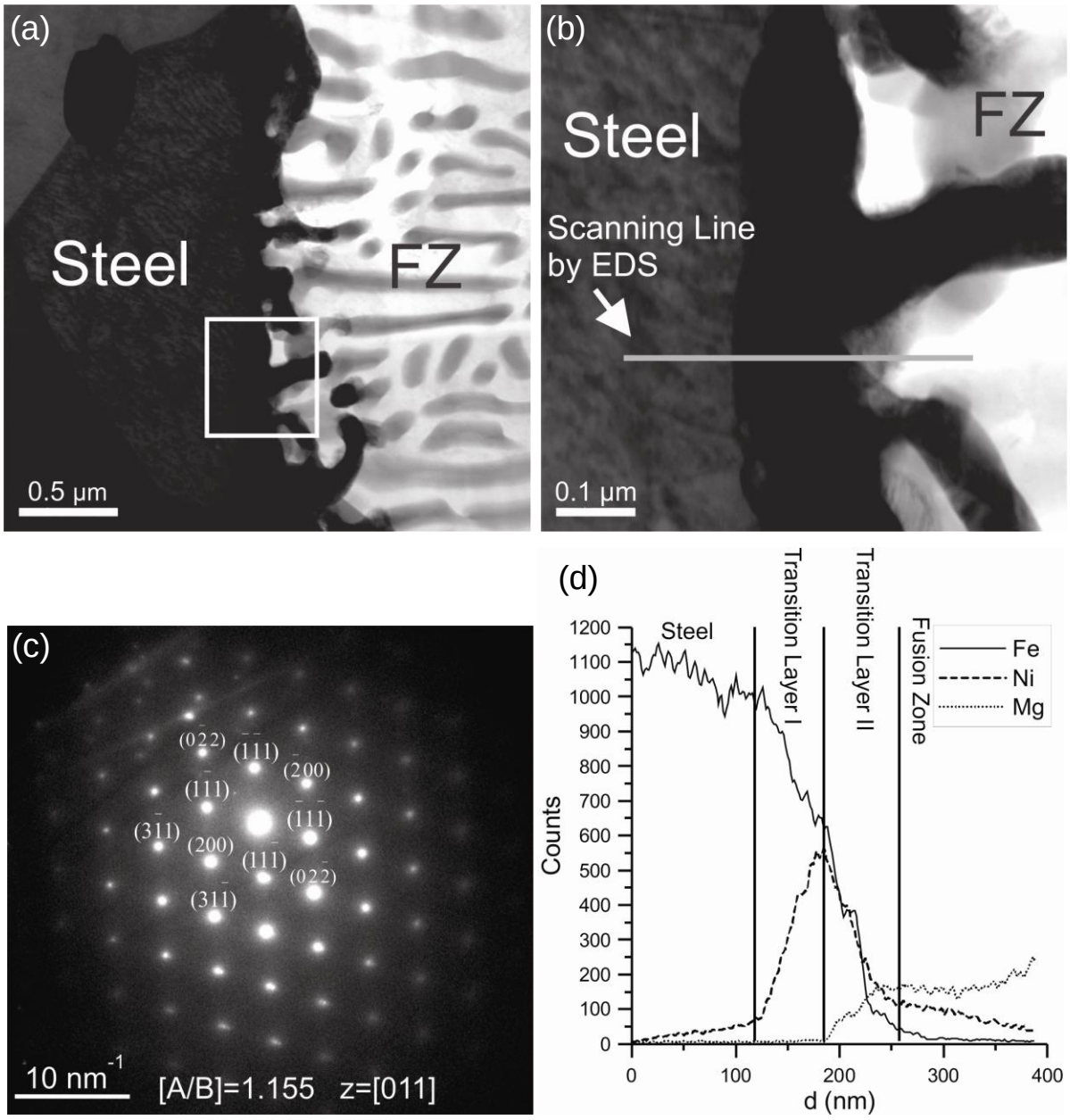

Figure 5-13: (a) TEM image of the steel-fusion zone interface, (b) higher magnification of the selected square area in (a), (c) SADP in the [011] zone axis of the interfacial phase, and (d) EDS line scan analysis of Fe, Ni, and Mg at the steel-fusion zone interface.

Therefore, the Fe(Ni) layer proved to be the key factor for realizing a metallurgical bond between the steel and the fusion zone. Representative concentration profiles of Fe, Ni, and Mg across the interface between the fusion zone and the steel are shown in Figure 5-13d. It is evident from these line scans that Fe, Ni, and Mg diffused into each other as a result of the high temperature experienced during the laser brazing process. As a result, two diffusion or transition layers formed between the steel and fusion zone. According to the element distributions of Fe, Ni, and Mg (see Figure 5-13d), in transition layer I with a thickness of almost 70 nm from the steel side, the Fe content decreased gradually while the Ni content increased. In this layer, solid-state diffusion of Ni and Fe into each other is believed to control the overall thickness of this layer.

Another diffusion layer (transition layer II) was observed in Figure 5-13d between the transition layer I and the fusion zone. The thickness of this layer was ≈ 60 nm. A slight diffusion of magnesium from fusion zone into transition layer II was detected. It would appear that there was sufficient solubility of the Mg in this Fe(Ni) interlayer for diffusion of the Mg to occur and that wetting and bonding of the α-Mg + Mg_2Ni eutectic phases had in fact occurred with the thin Fe(Ni) interlayer that had formed during laser brazing, and not directly with the steel.

5.3.5 Mechanical Properties

Due to the non-symmetric configuration of the 5 mm wide tensile-shear test specimens (see Figure 3-5a), a combination of shear and tensile forces existed at the interface. Consequently, the joint strengths are reported here as fracture load, since it is not possible to separate tensile and shear stresses. The average tensile shear strength of the laser brazed steel-Ni-AZ31B joints using the Mg-Al filler metal was found to be 153.7±2.7 kgf (or 1506.3±24.5 N). This is 94.8 % higher than tensile shear strength of the laser brazed Al coated steel-AZ31B Mg alloy specimens [69]. The low standard deviation of the tensile shear strength of the laser brazed steel-Ni-AZ31B joints (±2.7 kgf) compared with the laser brazed steel-Al-AZ31B joints

(±11 kgf) indicated that the laser brazing process was inherently stable and reproducible. If only the shear plane is considered, the average shear strength of the joints was 90.4±1.5 MPa, or 56.5±0.9% of that of AZ31B-H24 Mg alloy base metal (~ 160 MPa).

All tensile-shear specimens fractured in the FZ very close to the steel-FZ interface. Typical fracture surfaces of both the fusion zone side and the steel side after tensile shear testing are shown in Figure 5-14. Figure 5-14a and Figure 5-14c are low magnification SEM micrographs of the fracture surfaces of the fusion zone side and the steel side, respectively, and dimples are shown at high magnification in Figure 5-14b and Figure 5-14d. This uniform distribution of the dimples is characteristic of ductile fracture surfaces. These fracture surfaces indicated that the specimens failed under conditions similar to tensile test with a strong shear stress component (tensile-shear test). The effect of shear stress on the morphology of the dimples is very evident in these micrographs. The vertical direction in each of the micrographs is parallel to the direction of the shear and the elongation of the dimples under the action of shear stress is evident in Figure 5-14b and Figure 5-14d. The AlNi IMC compound was not found at the fracture surfaces.

The EDS analysis results of the fracture surfaces of both the steel and FZ side also indicated that crack propagation during the tensile shear tests had occurred entirely in the FZ. Based on the EDS results, the composition of the fracture surface for both steel side and FZ side were similar to the FZ, meaning fracture passed through the FZ near the steel-FZ interface.

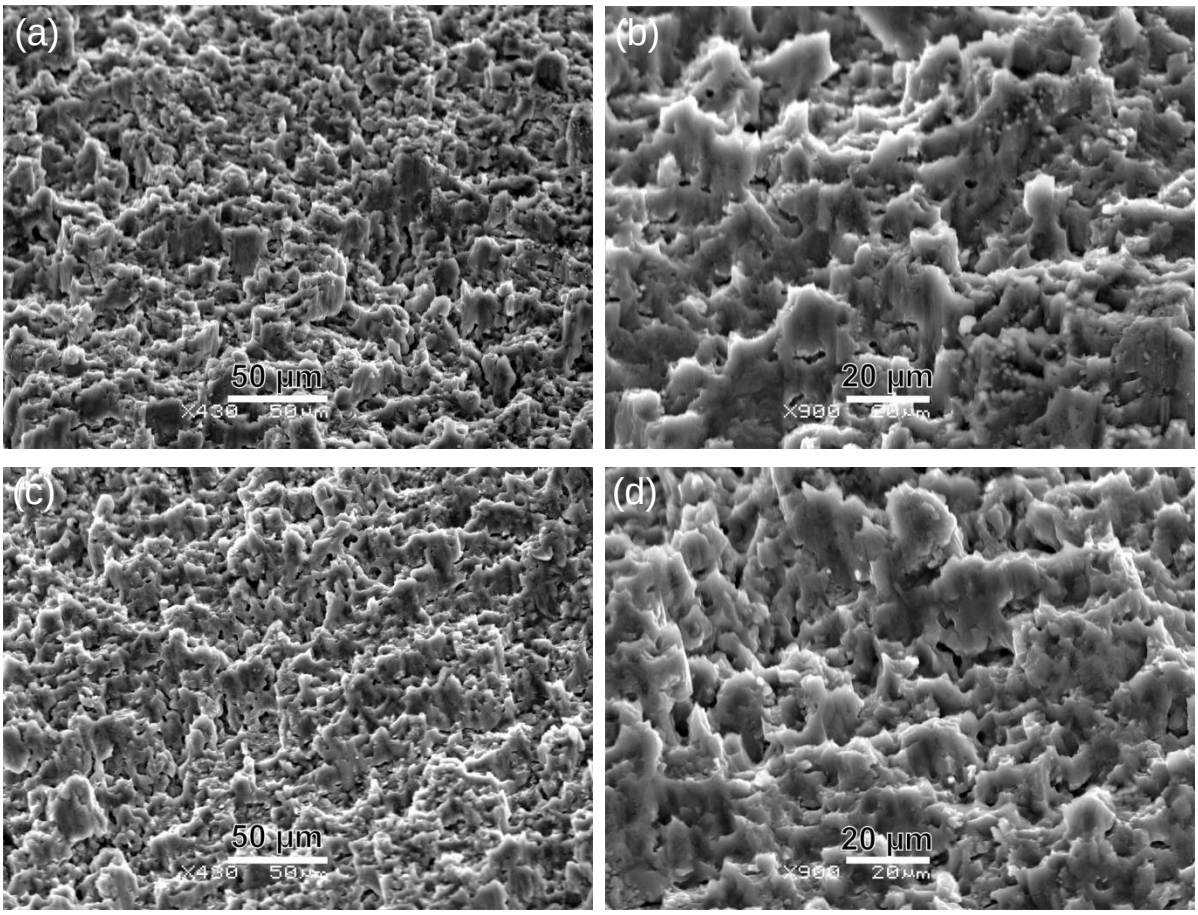

Figure 5-14: SEM images of typical fracture surfaces after the tensile shear test, (a) and (b) fusion zone side at different magnifications, (c) and (d) steel side at different magnifications.

Figure 5-15 shows the XRD pattern from the fractured surface of the joint on the steel side. Fe, α-Mg, and AlNi peaks were seen in this X-ray diffraction result. These findings were consistent with the SEM and EDS analysis results.

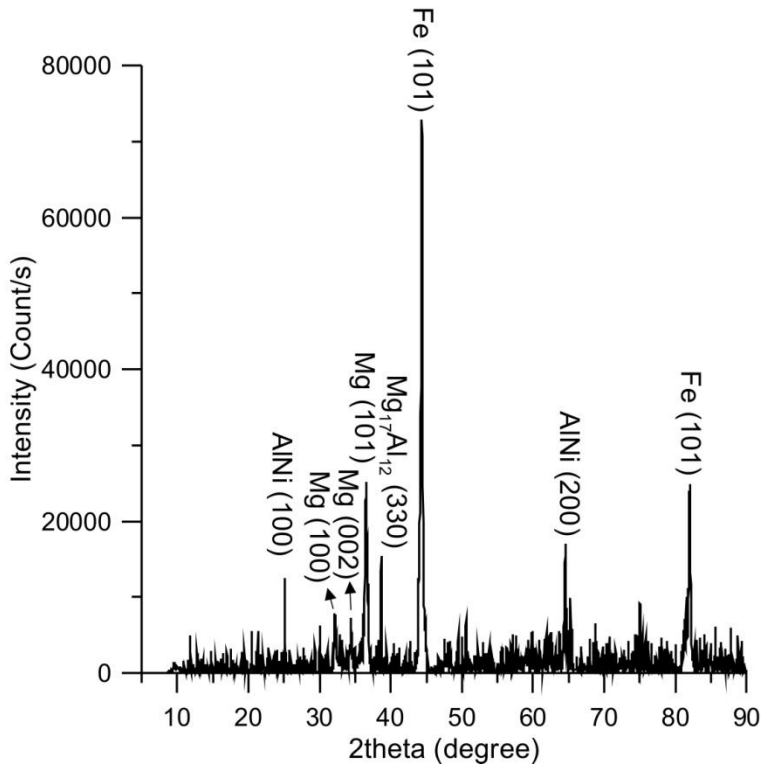

Figure 5-15: X-ray diffraction pattern of the fracture surface of the steel side.

5.3.6 Sequence of Phase Formation along the Interface (Bonding Mechanism)

From the above results, the interaction between the filler metal and the surface of the Ni-plated steel can be explained as follows (see Figure 5-16):

Firstly, the solid-state Ni plated steel is in contact with the liquid filler metal (Mg-Al alloy) at the laser brazing temperature and subsequently the liquid Mg-Al alloy flows over the Ni surface (Figure 5-16a).

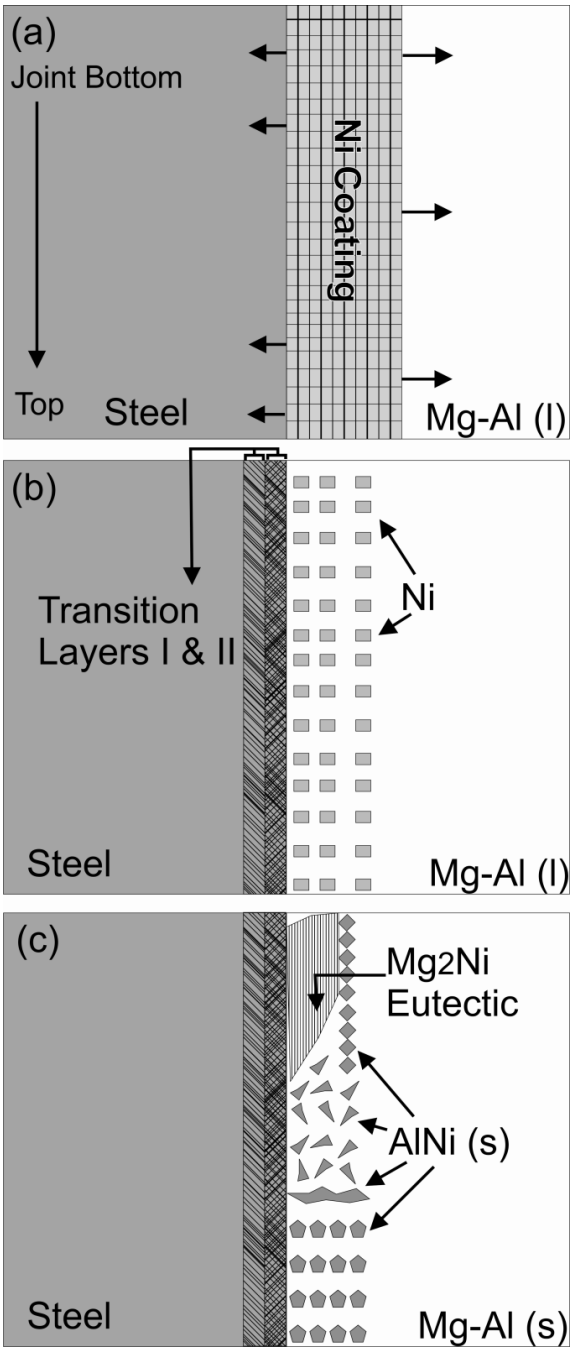

Figure 5-16: Formation of transitional layer and intermetallic compounds during the laser brazing of Ni-plated steel-AZ31B with Mg-Al filler metal: (a) wetting of the Ni-plated steel by molten filler metal and dissolution and diffusion of Ni into the FZ and steel substrate, (b) formation of the transitional layer and aggregation of Ni along the interface, and (c) nucleation and growth of AlNi IMC, and growth of the remaining liquid in the form of α-Mg + Mg_2Ni eutectic onto the thin Fe(Ni) interlayer.

Secondly, dissolution and diffusion of Ni atoms into the liquid occur, as shown in Figure 5-16b. At the same time, some solid-state diffusion of Ni atoms into the steel also occurs. A slight diffusion of Fe atoms into the liquid was also observed. Meanwhile, Mg atoms from the liquid may slightly diffuse into the Ni-alloyed steel side. Therefore, a thin diffusion or transition layer forms continuously along the interface between steel and fusion zone from the bottom side to the top side of the joint. This transition layer is a solid solution of Ni in Fe (with low content of Mg for transition layer II). This Fe(Ni) solid solution with FCC crystal structure is more favourable for bonding to Mg than having a body-centered cubic (BCC) phase along the interface.

Zhang *et al*. [45] used an edge-to-edge matching crystallographic model to predict all orientation relationships between crystals that have simple hexagonal close packed (HCP) and BCC structures and they found that the lattice mismatching of HCP (Mg) and BCC (Fe) is very large. On the basis of the observation in our study, a diffusion layer composed of Fe and Ni with FCC structure can provide the conditions for the heterogeneous nucleation of α-Mg during solidification. The result is formation of a metallurgical bond between the steel and magnesium alloy. A recent study by Liu *et al*. [44], showed that a nano-layer of Fe_2Al_5 on steel can also be a transition layer to bond Fe to Mg due to the low energy interfaces and good match of lattice sites between Fe and Fe_2Al_5 as well as Mg and Fe_2Al_5. The same behaviour was observed for the Fe(Ni) transition layer in this study. Formation of a transition zone was also reported in other studies [34-39] using different joining techniques, when an interlayer was used between steel and Mg alloy. These transition layers on steels were reported to make it possible to join Mg and steel.

Thirdly, during the solidification process, the AlNi phase with a high melting point (1133 ˚C) precipitates from the liquid and grows in a form of faceted dendrites very close to the interface (Figure 5-16c). These faceted dendrites form due to kinetic difficulties in forming new planes of atoms [92]. In this type of dendrite, the growing direction of dendrite arms are ones that are capped by relatively slow growing planes (usually low-index planes) [92]. The slowest growing plane would be expected to be the closest-packed planes. Weinberg and Chalmers [93] reported that the axis of a pyramid, whose sides are the most

closely packed planes, is generally the major dendrite direction. As a result, for AlNi faceted dendrites with BCC structure, this direction is <100>. Therefore, the process of solidification at the middle part of the joint starts with the nucleation and the growth of the AlNi faceted dendrites along the <100> growth direction.

Fourthly, if the Ni content of the remaining liquid between the steel side and the formed AlNi precipitates is high enough, Mg_2Ni with a melting point of 762˚C nucleates (see Figure 5-16c). Formation of Mg_2Ni depends on sufficient Ni concentration in the remaining liquid near the steel-FZ interface after formation of the AlNi IMC. The Ni content of the remaining liquid after precipitation of AlNi increases from 2.4 at.% at the top side of the interface to 10.6 at.% at the bottom portion; because formation of AlNi IMC layer consumed the Ni atoms near the interface and the volume fraction of this phase increased from the bottom to the top portion of the joint.

Based on the above analysis, high enough concentration of Ni in the remaining liquid close to the bottom side of the joint after formation of AlNi IMC resulted in formation of the Mg_2Ni + α-Mg lamellar eutectic in the form of a gray phase between the AlNi IMC and the steel. In order for this lamellar eutectic to grow, the local composition of the fusion zone should be close to the eutectic composition (10 at.% Ni, according to the Mg-Ni binary phase diagram) [92]. Reactions between Mg in the fusion zone and Ni along the interface caused formation of the Mg-Ni eutectic phase. This reaction can be represented by the following balanced chemical reaction:

$$L\left(10at.\%Ni\right)\xleftrightarrow{508°C}Mg_2Ni\left(33at.\%Ni\right)+Mg\left(0at.\%Ni\right) \qquad (5.10)$$

Therefore, at the bottom of the interface, two reactions occurred; the first one was precipitation of AlNi from the liquid and the second one was the eutectic reaction between Mg and Ni in the FZ (reaction 5.10). In the case of reaction sequences, first AlNi forms near the interface and then the remaining liquid with a low Al content between the AlNi IMC and steel-FZ interface, which is still rich in Ni, undergoes a eutectic reaction with Mg and results in the formation of the lamellar α-Mg + Mg_2Ni eutectic.

With the formation of the AlNi IMC layer, diffusion of Ni atoms from the steel side to the FZ is blocked. Therefore, the concentration of Ni in the remaining liquid between the

interface and preformed AlNi phase is expected to be higher than the remaining liquid on the other side of the AlNi phase. The result is the formation of Mg_2Ni just between the AlNi phase and the steel (see Figure 5-16a and b).

In the top portion of the interface, with the nucleation and growth of the AlNi particles, most of the Ni atoms are consumed. Therefore, the Ni content of the remaining liquid would not be enough for formation of the Mg_2Ni phase.

5.3.7 Lattice Matching Analysis of the Interfaces

Use of Ni as the interlayer between the steel and Mg alloy led to formation of a nano-scale Fe(Ni) transition layer on the steel [88]. Despite the fact that eutectic Mg_2Ni phase also formed in some area along the interafce, the dominant solidified phase on the Fe(Ni) phase was the Mg [88]. The average tensile shear strength of the laser brazed joint using Ni interlayer was siginificantly higher than the Al-12Si interlayer. Also, the fracture did not occurred along the steel-Mg interface. Therefore, strong interfaces (interfaces with low strain energy density) are expected to form when Fe(Ni) forms along the Mg-Fe interface.

To study the lattice matching along the formed interfaces, the edge-to-edge model was also applied to the Mg-Fe(Ni)-Fe system. The calculation procedure and the results of the interatomic spacing misfits along matching directions and interplanar spacing mismatches between matching planes for different formed interfaces in this study are given in the Appendix, Section A.2. The results presented in the Section A.2 confirmed that when Ni was used as the interlayer, formation of Fe(Ni) along the interface led to formation of interfaces with calculated minimum interplanar mismatches of $1\%_{\{Mg\text{-}Fe(Ni)\}}$-$4.4\%_{\{Fe(Ni)\text{-}Fe\}}$, interfaces with low strain energy values, thereby modifying such properties as the interfacial strength and the bond strength.

5.4 Chapter Summary

In this chapter, the thermodynamic stability of precipitated phases at the steel-Ni-Mg alloy interface during laser brazing of Ni-plated steel to AZ31B magnesium sheet using AZ92 magnesium alloy filler wire has been evaluated using FactSage thermochemical software. Also the brazeability of AZ31B-H24 magnesium alloy and steel sheet with a micro-layer of electro-deposited Ni in a single flare bevel lap joint configuration was analyzed. Assuming local chemical equilibrium at the interface, the chemical activity-temperature-composition relationships of intermetallic compounds that might form in the steel-Ni interlayer-AZ92 magnesium alloy system in the temperature range of 600-1100 °C were estimated using the Equilib module of FactSage. The results provided better understanding of the phases that might form at the interface of the dissimilar metal joints during the laser brazing process. The addition of a Ni interlayer between the steel and the Mg brazing alloy was predicted to result in the formation of the AlNi, Mg_2Ni, and Al_3Ni_2 intermetallic compounds at the interface depending on the local maximum temperature. This was confirmed experimentally by laser brazing of Ni electro-plated steel to AZ31B-H24 magnesium alloy using AZ92 magnesium alloy filler wire. The macro- and microstructure, element distribution, and interfacial phases of the joints were studied by optical microscopy, scanning electron microscopy, transmission electron microscopy, and X-ray diffraction. As predicted, the formation of just AlNi and Mg_2Ni from a monotectic and eutectic reaction, respectively, was observed near the interface. It was also shown that improved wetting and bonding between the magnesium brazing alloy and electro-plated Ni steel sheet was facilitated by the formation of a transition layer composed of a solid solution of Ni in Fe that formed on the steel surface by diffusion of the Ni a short distance into the steel during brazing. The average fracture shear load of the bond reached 1506.3 N and the joint efficiency was 56.5% with respect to the AZ31B-H24 Mg alloy base metal. In all cases, failure occurred in the fusion zone very close to the steel-fusion zone interface.

Chapter 6
Laser Brazing of AZ31B to Sn Electro-Plated Steel Sheet

The brazeability of AZ31B-H24 magnesium alloy sheet to Sn-coated, AISI 1008 plain carbon steel sheet in the lap joint configuration using an Mg-Al-Zn alloy filler metal and a diode laser heat source has been investigated. This included determination of the mechanical properties of the joints and detailed microstructural evaluation of phases at the interface and their crystal orientation relationships by optical microscopy, scanning electron microscopy and high resolution transmission electron microscopy. The work presented and described in this chapter has been submitted for publication by Nasiri *et al*. [94].

6.1 Results

Visually acceptable laser brazed joints were made using 2.2 kW laser power, 8 mm/s travel speed, and 0.2 mm beam offset to the steel side. These conditions resulted in melting of the filler alloy to form a fillet with triangular cross section between the AZ31B Mg and steel base metals (see Figure 6-1). Typically, there was a uniform brazed area with good wetting of the Mg-Al-Zn brazing alloy to the steel base metal and some melting of the AZ31B base metal. The average leg length of the Mg-Al-Zn alloy filler metal-steel interface was 7.5 ± 2.1 mm.

Figure 6-1a shows a typical tensile shear test of a laser-brazed specimen. All tensile-shear specimens fractured in the steel base metal well away from the brazed joint. The average fracture load of 10 mm wide tensile shear specimens was found to be 2064 ± 85 N. This value was exactly the same as fracture load of the steel base metal with the same size tensile specimen, confirming that fracture of the laser brazed joint always occurred in the steel base metal. The average interface area between the braze alloy and the steel sheet was 75 mm^2; therefore, the tensile shear strength of the interface was greater than 2,064/75 = 27.5 MPa.

A cross sectional view of a typical laser brazed specimen is shown in Figure 6-1b. The average contact angle of the fusion zone (FZ) on the steel substrate was measured to be

35º±5º, which is indicative of good wetting of the Sn-coated steel substrate by the molten Mg filler alloy [25]. Defects such as porosity or cracks were not observed in the joint.

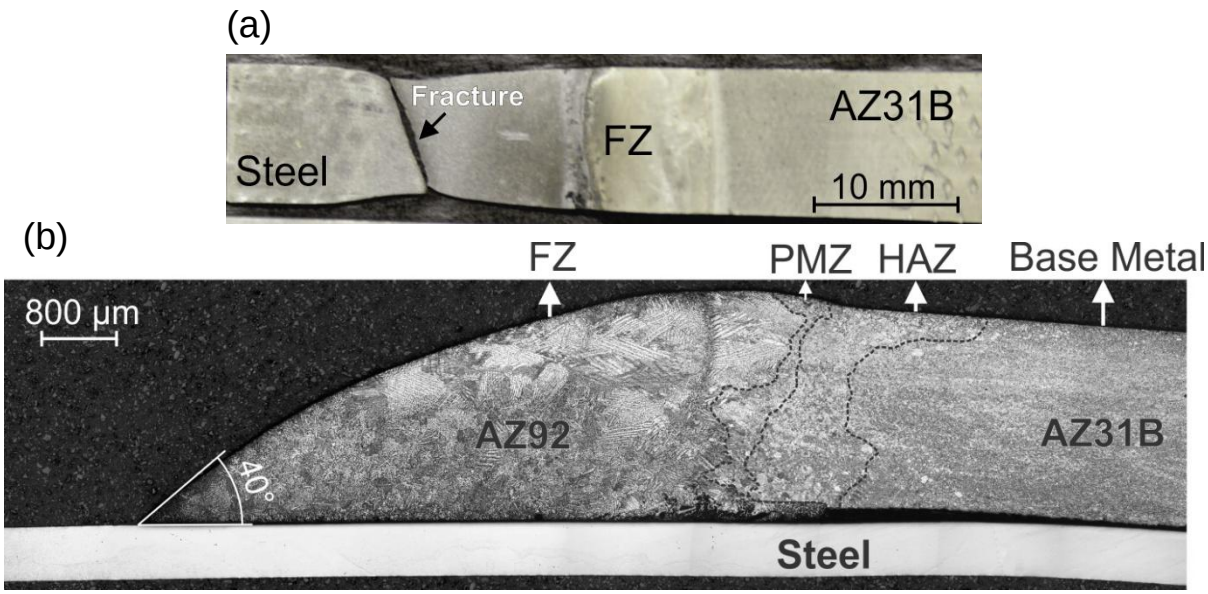

Figure 6-1: (a) a typical fractured specimen after tensile shear test of the laser brazed joint and (b) transverse section of a laser brazed Sn electro-plated steel/AZ31B joint made using 2.2 kW laser power, 8 mm/s travel speed, and 0.2 mm beam offset to the steel side.

6.1.1 Microstructural Analysis of the Steel-FZ Interface

The microstructure in the AZ31B-H24 Mg base metal and filler metal were similar to that observed in previous studies with these alloys [69,88]. As indicated in Figure 6-1b, in the base metal, continued recrystallization and grain growth occurred in the AZ31B heat affected zone (HAZ). In the partially melted zone (PMZ), localized melting or liquation of the intergranular regions occurred. The solidification microstructure of the FZ was a combination of columnar and equiaxed α-Mg dendrites with a divorced eutectic β-$Mg_{17}Al_{12}$ intermetallic phase at the dendrite boundaries. A more detailed microstructural analysis of the fusion zone and AZ31B Mg alloy microstructure may be found in Chapter 4 [69].

Figure 6-2 shows a typical SEM image of the microstructure along the steel-fusion zone interface. After the laser brazing process, the Sn coating was not detected as a separate layer along the interface. This suggests that the low melting point Sn (T_{mp} = 232 ºC) layer had been entirely melted and mixed with the molten Mg filler alloy immediately adjacent to the interface. The microstructure of the steel-FZ interface was the same along the entire length of the interface. The contrast of α-Mg adjacent to the interface looks darker than the α-Mg in the fusion zone, meaning lower Al content of α-Mg adjacent to the interface (see Figure 6-2). Therefore, Al atoms near the interface should be consumed in a way, which is unclear according to the SEM photomicrograph. While this SEM photomicrograph might suggest that the α-Mg phase has bonded directly to the steel substrate, it is well known that this will not occur due to the very large lattice mismatching of Fe and Mg [39]. In our previous studies [69,88], a sub-micron thick transitional layer or phase was found to exist at the steel-magnesium interface that could not be resolved by optical microscopy or the SEM. This intermediate phase was found through TEM examination to be responsible for the metallurgical bond between these two immiscible alloys.

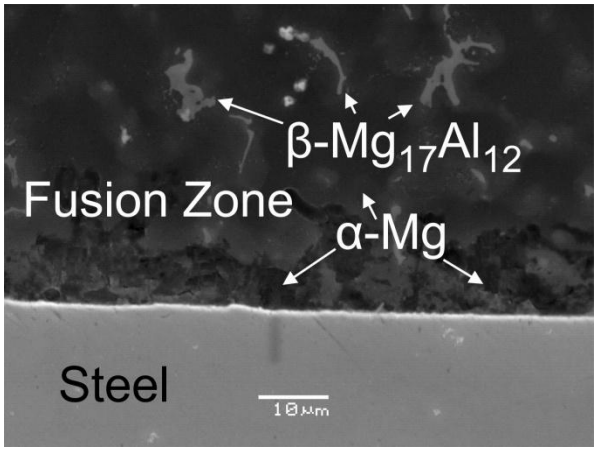

Figure 6-2: SEM image along the steel-FZ interface.

Figure 6-3a shows a scanning transmission electron microscopy (STEM) image of the steel-fusion interface. Complete metallurgical bonding appears to have occurred along the

entire length of the interface; however, there is a band of nano-scale pores with an average diameter of 145 ± 22 nm in the steel substrate adjacent to the interface. As shown at even higher magnification in Figure 6-3b, a very thin layer of a distinctly different phase exists between the steel and the fusion zone which appears to have created a transitional interlayer between these two alloys that forms a bond with the steel substrate on one side as well as the magnesium filler alloy on the other side.

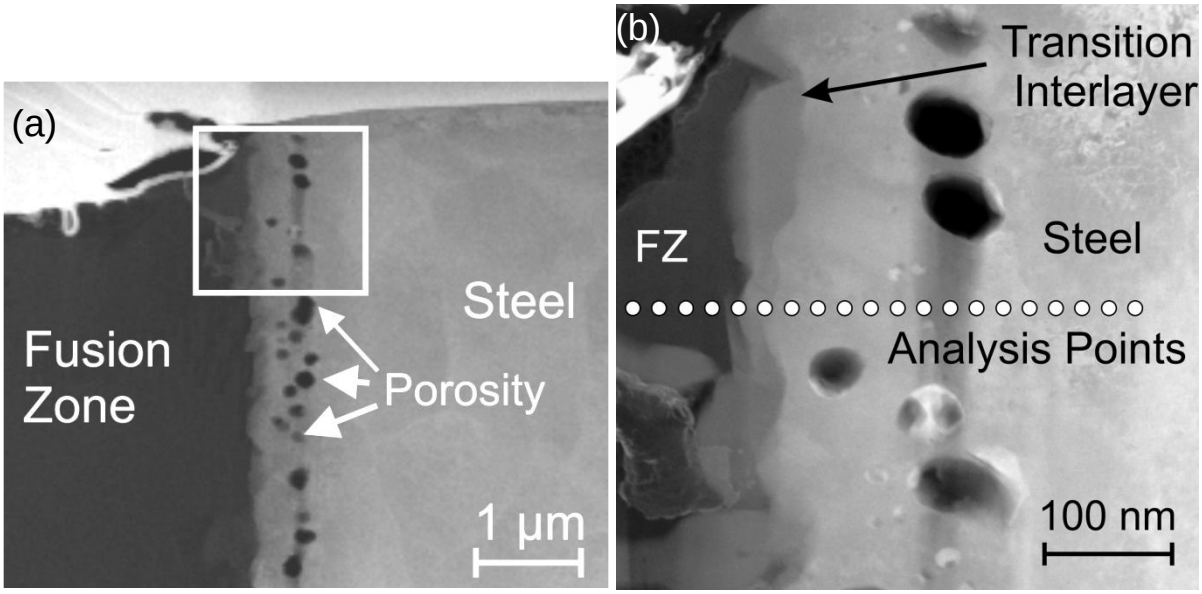

Figure 6-3: (a) STEM image of the steel-fusion zone interface and (b) higher magnification of the selected square area in (a).

STEM-EDS compositional mapping and line scanning analysis were used to identify the composition of the phases formed at the steel-fusion zone interface shown in Figure 6-3. Figure 6-4a shows a STEM image of a representative area of the interface and concentration maps of this same area for Mg, Fe, Al, Mn, and Sn. Mg is seen to be present primarily in the fusion zone, but nowhere else. Similarly, Fe from the steel exits up to the interlayer, but is not present in the fusion zone. The nano-scale pores are within the Fe. There is a significant concentration of Al from the braze alloy within the interlayer and also to a depth of about 270 nm into the steel substrate and past the band of pores. Mn, also from the braze alloy, is

concentrated primarily within the interlayer and is not detected in significant quantities elsewhere in the braze alloy and only in small concentrations in the steel. Finally, there appears to be very low concentrations of Sn only within the steel close to the interface.

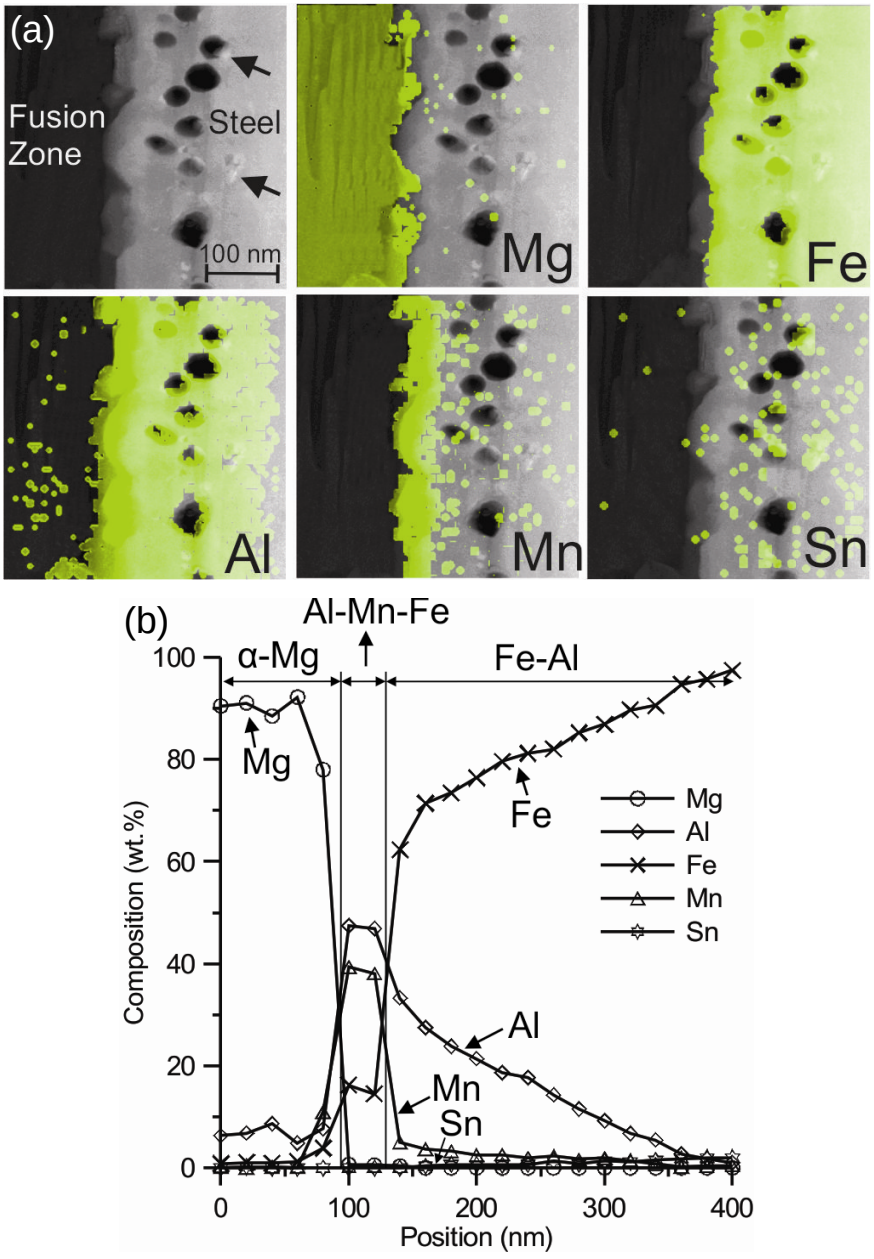

Figure 6-4: (a) STEM-EDS concentration maps and (b) STEM-EDS composition line scans across the steel-fusion zone interface shown in Figure 6-3b, indicating scans of Mg, Fe, Al, Mn, and Sn.

The composition and distribution of elements across the interface between the steel and fusion zone was also analyzed using STEM-EDS point analysis along the line shown in Figure 6-3b. These results are shown in Figure 6-4b and are consistent with those shown in the element maps in Figure 6-4a, *e.g.*, the Mg exists only in the filler metal and Sn is detectable in only very small concentrations within the steel. While the Al concentration in the fusion zone is close to the nominal 9 wt.% Al of the braze alloy (see Figure 6-4b), the concentration increases in a step-wise fashion to about 48 wt.% Al in the interlayer and then drops to about 31 wt.% followed by a continual decrease of the Al concentration to a distance of about 270 ± 46 nm into the steel which is past the band of pores. This is indicative of solid-sate diffusion of the Al into the steel. With the increased Al concentration in the steel, there is a complementary decrease of the Fe concentration at the steel surface approaching the interlayer. The Fe concentration appears to drop to about 15 wt.% in the interlayer and is not detected in the fusion zone. Mn, also present in concentrations less than 1 wt.% in all three alloys, is concentrated up to 40 wt.% primarily within the interlayer and is not detected in significant quantities elsewhere in the braze alloy and only in small concentrations in the steel. The average thickness of the interlayer was 45 ± 10 nm and it contained only 60.9 ± 0.2 at.% Al, 34.8 ± 0.6 at.% Mn and 4.3 ± 0.4 at.% Fe. This suggests that the interlayer is composed of the $Al_8(Mn,Fe)_5$ intermetallic compound.

The range of composition in the Fe-Al diffusion layer evident in Figure 6-4b is consistent with the range of Al composition over which the disordered α-Fe and ordered Fe-Al solid solution phases exist in the Fe-Al binary phase diagram [95]. This was confirmed using SADP analysis. Figure 6-5a shows a bright field TEM image of the interface region between the steel substrate, the $Al_8(Mn,Fe)_5$ interlayer and the Mg braze alloy and Figure 6-5b shows a SADP obtained from the Fe-Al phase region. Analysis of this pattern indicated that this phase is a Fe(Al) solid solution with a Body Centered Cubic (BCC) crystal structure. The SADP was taken along the $\left[\bar{1}11\right]$ zone axis of the phase. The lattice parameter of Fe(Al) was calculated to be a = 2.885 *Å*, which is similar to the lattice parameter of Fe (a_{Fe} = 2.8606

Å). Thus, the crystal structure and the lattice parameter of Fe(Al) were similar to Fe. The Fe-Al binary phase diagram shows up to 55 at.% solid solubility for Al in Fe [95,96]. The Fe(Al) solid solution is well-known for its relatively high strength, high oxidation resistance, low cost and excellent fracture toughness [97,98].

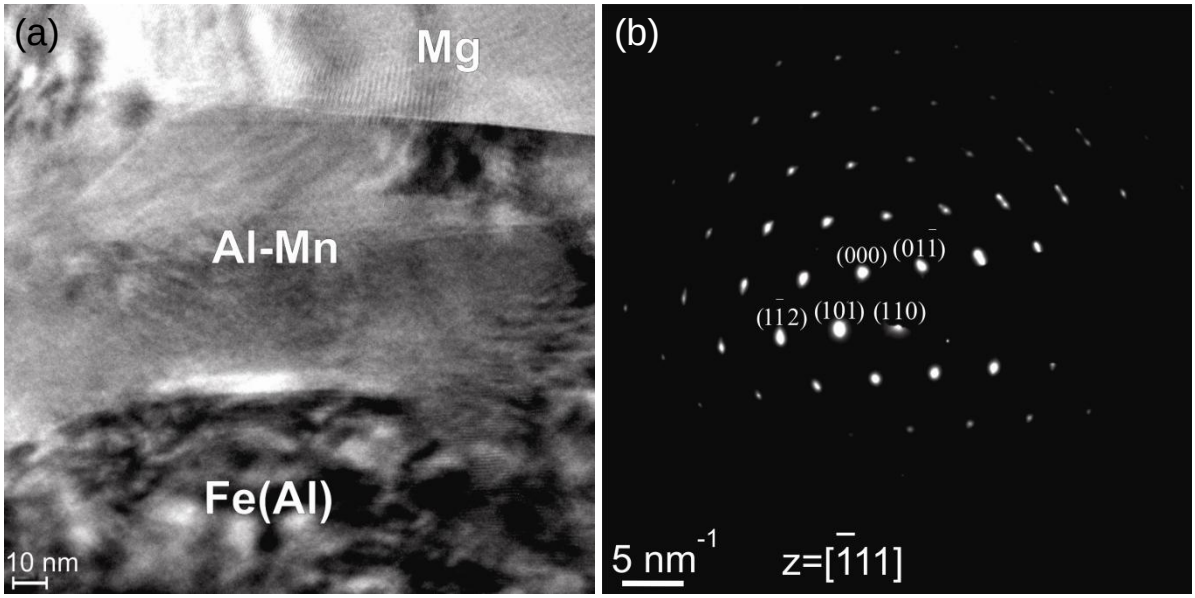

Figure 6-5: (a) Bright field TEM image of the Fe(Al)/Al-Mn/Mg (substrate-fusion zone) interfaces and (b) SADP of the Fe(Al) phase in the $\left[\bar{1}11\right]$ zone axis of this phase.

According to the results of thermodynamic calculations under Scheil cooling conditions performed by Kim *et al.* [99], during solidification of the Mg-Al-Zn brazing alloy, the sequence of phase formation during solidification is first Al_8Mn_5, then α-Mg and finally the β-phase ($Mg_{17}Al_{12}$). Therefore, it is expected in the present study that a thin layer of Fe(Al) compound at the steel-FZ interface forms first by solid-state diffusion of Al in the FZ liquid into the steel. Upon further cooling, the Al_8Mn_5 intermetallic nucleates and grows on the Fe(Al) compound surface layer that has formed on the steel and there is time for a thin layer to grow and cover the Fe(Al) (BCC) surface. Thereafter, the remaining FZ liquid will be in contact with only the thin Al_8Mn_5 layer and this new interlayer phase now plays the

role of the substrate for subsequent reactive wetting, nucleation and growth of the remaining α-Mg liquid onto the thin surface layer of Al_8Mn_5.

6.1.2 Measurements of the Crystallographic Orientation Relationships and Lattice Matching at the Steel-FZ Interface

When reaction products form at the interface of dissimilar metals, the bond strength between the two phases is directly affected by the interfacial energy density of the interface which in turn depends on the degree of crystallographic registry, *i.e.*, the crystallographic orientation relationship, OR, and lattice matching, that exists between the two phases at their interface [25,100]. In the present study, in order to identify the OR and lattice matching between the Al_8Mn_5 phase with a rhombohedral crystal structure and the BCC Fe(Al) phase on the one side (steel) and the Hexagonal Close-Packed (HCP) α-Mg phase on the other side (fusion zone), high resolution (HR)-TEM analysis of the interface was performed.

Figure 6-6a shows a HR-TEM image of the Al_8Mn_5 phase-Fe(Al) substrate interface. When the specimen was aligned with the direction of Al_8Mn_5 $\left[10\bar{1}1\right]$, the $\{110\}_{Fe(Al)}$ was within 4.2° of the $\left\{30\bar{3}3\right\}_{Al_8Mn_5}$ and the measured interplanar spacing for these planes were $d_{\{110\}Fe(Al)}$ = 2.095 Å and $d_{\{30\bar{3}3\}Al_8Mn_5}$ = 2.204 Å, which represents only 5.2 % interplanar mismatch at the interface. Thus, good lattice matching with low angle rotation of matched lattice planes exists between the Fe(Al) and Al_8Mn_5 phases at this interface.

Figure 6-6b shows the HR-TEM image of the Al_8Mn_5-α-Mg interface. Using HR-TEM, it was found that when $\left[10\bar{1}1\right]_{Al_8Mn_5}$ //$\left[10\bar{1}0\right]_{Mg}$, the $\left\{30\bar{3}3\right\}_{Al_8Mn_5}$ was within 47.4° of the $\{0002\}_{Mg}$. Similarly, the measured *d*-value of the $\{0002\}_{Mg}$ was 2.574 Å. This represents 16.8 % mismatch with that of the $\left\{30\bar{3}3\right\}_{Al_8Mn_5}$. This analysis showed a poor crystallographic matching between Al_8Mn_5 and α-Mg with a large angle rotation of matching planes at their interface. As shown in Figure 6-6, HR-TEM analysis of the Fe(Al)-Al_8Mn_5 interface showed an OR with low angle rotation of the matching planes and low interplanar mismatch. This

good match of lattice sites between Al_8Mn_5 and Fe(Al) leads to low energy density interface and, therefore, good wetting and strong bond between these phases present at the interface.

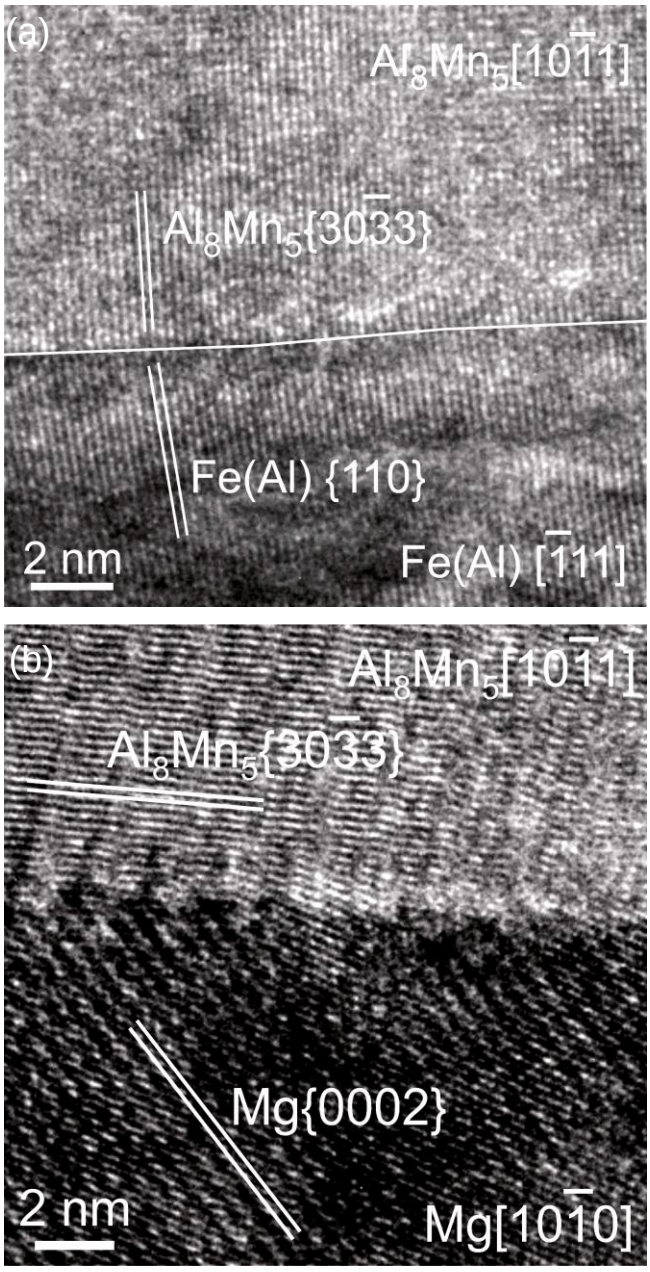

Figure 6-6: HR-TEM image of the (a) Fe(Al)–Al_8Mn_5 interface and (b) Al_8Mn_5–Mg interface.

6.1.3 Analysis of the Lattice Matching at the Steel-FZ Interface

The HR-TEM measurements in this study indicated that good lattice matching exists between the Al_8Mn_5 and Fe(Al) phase on the steel side. To further study the interatomic spacing misfit along matching directions and the interplanar spacing mismatch between matching planes of the Al_8Mn_5-Fe(Al) and Mg-Al_8Mn_5 interfaces, the edge-to-edge crystallographic model was used.

Calculated data reported in the Appendix, Section A.3 indicate that initial formation of the Al_8Mn_5 phase on the Fe(Al) with good match of lattice sites at the solid (steel)-liquid (magnesium) interface during laser brazing (with calculated minimum interplanar mismatches of 10.4% $_{\{Mg\text{-}Al8Mn5\}}$-6.3% $_{\{Al8Mn5\text{-}Fe(Al)\}}$) ultimately led to formation of ORs with low mismatch strain along the Al_8Mn_5-Fe(Al) interface, thereby decreasing the energy density of the solid-liquid interface and improving not only the interfacial strength and the bond strength, but also the wetting and the work of adhesion between these two otherwise immiscible alloys. This is in good agreement with the HR-TEM experimental results (see Figure 6-6). Also, the measured average contact angle of the fusion zone (FZ) on the steel substrate ($35^o \pm 5^o$) was an indication of good wetting of the Sn-coated steel substrate by the molten Mg filler alloy (see Figure 6-1b).

It is worth noting that having the same crystal structure (BCC) and very similar lattice parameters (a_{Fe} = 0.286 nm and $a_{Fe(Al)}$ = 0.288 nm) for the Fe and Fe(Al) phase led to formation of a very coherent interface with extremely low strain energy. For this reason, the lattice matching results of the Fe(Al)-Fe interface were not included in the Appendix.

6.2 Discussion

6.2.1 Porosity Formation at the Steel-FZ Interface

In Figure 6-3 and Figure 6-4, there is evidence of a band of spherical, nano-scale pores that have formed parallel to the interface and within the single-phase Fe(Al) surface layer that

was created during the laser brazing operation. This type of porosity is very similar to the Kirkendall porosity observed by Saiz *et al*. [54] within a layer of $FeSn_2$ which formed parallel to the interface during soldering of a Fe-Ni alloy using Sn-Ag solder at 523 K (250 ºC). Salamon and Mehrer [101] have observed Kirkendall porosity formation in the diffusion zone of a $Fe_{82}Al_{18}/Fe_{58}Al_{42}$ diffusion couple. Springer *et al*. [102] reported formation of Kirkendall porosity in the reaction layer Fe_2Al_5 formed at the interface of friction stir welded steel to Al alloy joints. Finally, Tiwari and Mehrotra [103] have observed Kirkendall effect and Kirkendall porosity in their recent study of interphase interdiffusion mechanisms in NiAl and FeAl intermetallic compounds.

The necessary condition for occurrence of Kirkendall effect and formation of Kirkendall porosity in a binary diffusion couple is that two diffusing species should have unequal intrinsic diffusion coefficients [104]. In the present study, considering the location of the porosity (see Figure 6-3), the Kirkendall porosity is formed during inter-diffusion of the Al and Fe atoms within the Fe-Al diffusion layer; however, since the diffusivity of Al in Fe is greater than Fe in Al, there is a net flux of vacancies in the opposite direction of the Al diffusion that results in vacancy concentrations that exceed equilibrium values and ultimately result in nucleation and growth of nano-pores similar to those shown in Figure 6-3 [101-104].

In Figure 6-3, the average area fraction of Kirkendall porosity in the shear plane parallel to the interface is about 15%. However, this reduction in throat area due to the porosity was not sufficient to compromise the strength of the interface, primarily because of the significant strength of the Fe(Al) layer relative to the steel and the Mg-Al-Zn brazing alloy. The ultimate tensile strength (UTS) of Fe(Al) along the [001] crystallographic direction has been reported to be 19,000 MPa [105] whereas the UTS the steel sheet was 344 MPa and the Mg-Al-Zn brazing alloy is 170 MPa [106]. Thus, even with the Kirkendall porosity defects, the strength of the Fe(Al) layer far exceeds the strength of the steel and Mg-Al-Zn brazing alloy so that the Kirkendall porosity did not limit the overall tensile shear strength of the joint.

6.2.2 Sequence of Phase Formation along the Interface (Bonding Mechanism)

Based on the results described above, a sequence of events may be surmised to take place during laser brazing of the Sn-plated steel and the AZ31B Mg sheet. These are shown in the schematics in Figure 6-7 starting with the original joint configuration at room temperature shown in Figure 6-7a. During initial heating (see Figure 6-7b) the electroplated Sn layer melts when the temperature exceeds the melting temperature of the Sn (505 K (232 ºC)). At this stage, the steel surface is still covered by $Sn_{(l)}$ which continues to prevent oxidation of the steel surface. As shown in Figure 6-7c, at higher temperatures approaching 873 K (600 ºC), the flux is activated and then melting of the Mg-Al-Zn brazing alloy begins. The liquid Sn layer then easily diffuses from the interface into the molten FZ (Figure 6-7c), thereby allowing direct contact between the molten filler metal and the clean, oxide-free steel surface. At this stage, Al atoms from the fusion zone preferentially diffuse very rapidly from the molten FZ into the steel leading to the formation of a Fe(Al) diffusion layer (Figure 6-7d). Continued diffusion of the Al into the steel and growth of the Fe(Al) layer result in the formation of nano-sized Kirkendall pores within the Fe(Al) diffusion layer. As shown in Figure 6-7e, as cooling and solidification begins, the newly formed Fe(Al) layer also acts as an effective site for heterogeneous nucleation and growth of the Al_8Mn_5 phase from the molten FZ.

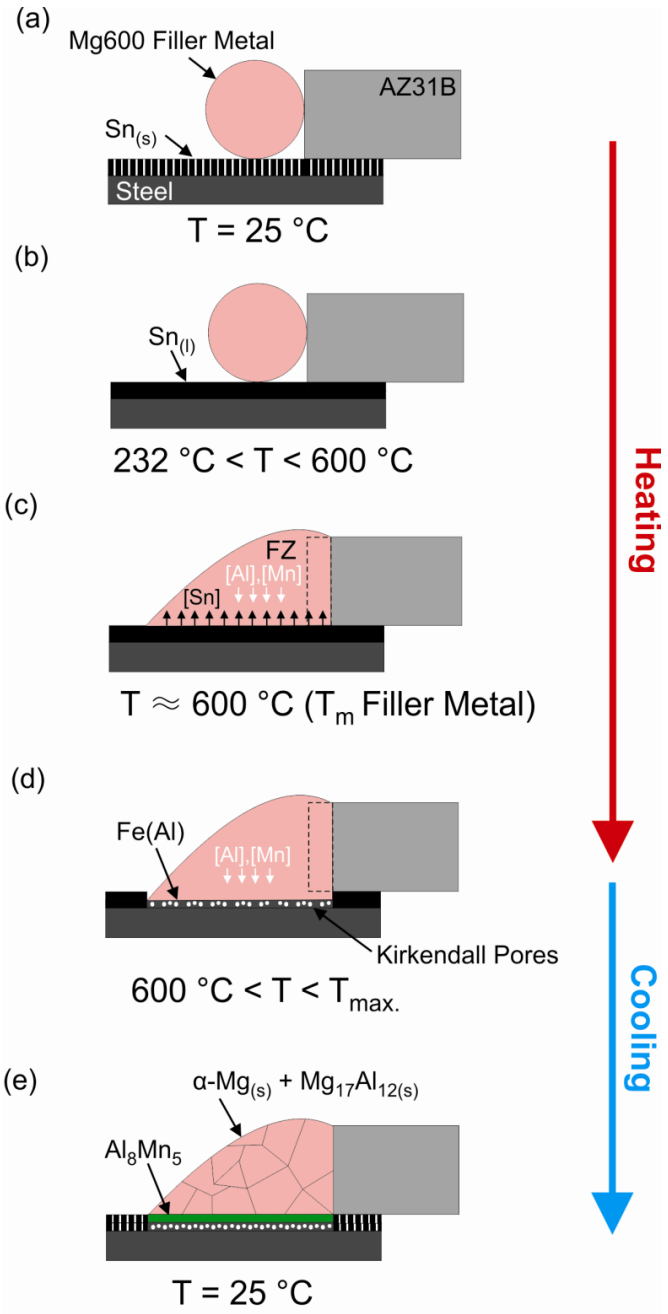

Figure 6-7: Schematic of interfacial layers formation during the laser brazing of Sn electroplated steel-AZ31B with Mg alloy filler metal: (a) lab joint design configuration prior to the laser brazing process at room temperature, (b) melting of Sn electroplated layer during heating, (c) melting of the filler metal and dissolution of liquid Sn into the FZ, (d) formation of Fe(Al) phase containing Kirkendall porosities on top of the steel substrate, and (e) nucleation of Al_8Mn_5 IMC on top of Fe(Al) phase and solidification of the FZ during cooling.

The good OR and lattice matching that exist between the Al_8Mn_5 and Fe(Al) phases result in low interfacial energy density, good wetting and good bonding between these two solid solutions along the fusion zone-Fe(Al) interface. Meanwhile, some Fe atoms from the substrate diffuse into this newly formed Al_8Mn_5 interfacial phase. As the temperature continues to drop, this $Al_8(Mn,Fe)_5$ intermetallic compound with rhombohedral crystal structure provides a surface for heterogeneous nucleation and growth of the solid α-Mg phase from the molten FZ. The resulting interface between the $Al_8(Mn,Fe)_5$ intermetallic compound and the solid α-Mg facilitates better wetting and bonding between these two phases than is possible between Mg and either Fe(Al) or Fe directly [88,107]. Finally, continued cooling and solidification of the FZ results in an equiaxed dendritic mixture of primary α-Mg and α-Mg + $Mg_{17}Al_{12}$ eutectic phases (see Figure 6-7e). Thus, bonding between the Mg-Al-Zn brazing alloy and the Sn-coated steel is a multi-step process involving first the creation of a Fe(Al) diffusion layer on the surface of the steel to which an interlayer of $Al_8(Mn,Fe)_5$ nucleates and grows and finally nucleation and growth of primary α-Mg from the molten FZ onto the $Al_8(Mn,Fe)_5$ interlayer. The results of this study indicate that formation of a strong bond between steel and magnesium is possible provided the conditions exist for formation of appropriate interfacial phases (reaction products) with good crystallographic OR and lattice matching with the substrate that leads to low interfacial energy densities and, therefore, good wetting and strong bonding between the interlayers.

It is interesting to note that the Sn coating on the steel does not appear to play a role in creating the final bond between the Mg-Al-Zn brazing alloy and the steel sheet. However, the Sn coating layer was essential to prevent oxidation of the steel surface during initial heating and prior to activation of the flux and direct contact between the molten filler alloy and the steel surface. Dissolution of the molten Sn layer into the molten fusion zone allows a clean and oxide-free steel surface to come in direct contact with the molten filler metal. Similar functional behaviour for the interlayer was recently reported by Wahba and Katayama [38] in laser welding of AZ31B magnesium alloy to Zn-coated steel, where Zn played the role of the interlayer.

6.3 Chapter Summary

In this chapter, the brazeability of AZ31B-H24 magnesium alloy sheet to Sn-coated, cold-rolled carbon steel sheet in a lap joint configuration using a Mg-Al-Zn based filler metal has been investigated. This included determination of the laser brazing process conditions required to make the brazed joints, the mechanical properties of the joints and detailed microstructural evaluation of phases at the interface and their crystal orientation relationships by optical microscopy, scanning electron microscopy and high resolution transmission electron microscopy.

The results showed that visually acceptable braze joints could be produced using 2.2 kW diode laser beam power moving at 8 mm/s travel speed along the joint. While the Sn coating promoted good wetting between the molten filler alloy and the steel sheet, it did not play a role in forming the final bond. Its primary function appeared to be in maintaining a clean, oxide-free steel surface until the molten Mg filler alloy could come in direct contact with the steel surface. In all cases, failure of transverse tensile shear test specimens of the joint occurred in the steel base metal. Bonding between the magnesium alloy and the steel was facilitated by the formation of two transition layers composed of Fe(Al) solid solution on the steel as a result of diffusion of Al from the fusion zone into Fe, followed by a nano-scale layer of Al_8Mn_5 phase on top of Fe(Al) in the fusion zone along the interface. Examination of the Fe(Al)-$Al_8(Mn,Fe)_5$ interface using HR-TEM showed that an orientation relationship with low angle of rotation of the matching planes and low interplanar mismatch existed at the Fe(Al)-$Al_8(Mn,Fe)_5$ interface (*i.e.*, $\{110\}_{Fe(Al)}$ was 4.2° from $\{30\bar{3}3\}_{Al_8Mn_5}$ with 1.3 % interplanar mismatch). These results were further validated using an edge-to-edge crystallographic matching model of the Fe(Al)-$Al_8(Mn,Fe)_5$ and $Al_8(Mn,Fe)_5$-Mg interfaces. These orientation relationship and interplanar mismatch between the interlayer and base metal phases are responsible for the low interfacial energy densities, good wetting and strong interfacial bonds observed in this complex dissimilar metal steel-Fe(Al)-$Al_8(Mn,Fe)_5$-Mg system.

Chapter 7

The Effect of Interfacial Reactions on Wettability of Ni-plated Steel by Molten Magnesium Brazing Alloy

In this study, wetting has been characterized by measuring the contact angles of AZ92 Mg alloy on Ni electro-plated steel as a function of measured peak temperature reached during laser heating. In particular, the effects of interfacial reaction products and lattice mismatching on wettability are discussed. The work presented and described in this chapter has been submitted for publication by Nasiri *et al*. [108].

7.1 Temperature *vs*. Laser Power

When using a constant 1.6 s pulse time, the laser power was found to directly affect the peak temperature during wettability tests in the range between 618 ºC (higher than liquidus temperature of the Mg alloy and flux activation temperature ≈ 600 ºC) up to 1020 ºC (close to the boiling point temperature of magnesium ≈ 1100 ºC). Figure 7-1 shows the maximum measured temperature from the back side of the steel sheet versus the laser powers used in this study. As expected, increasing laser power resulted in increased maximum measured temperature. A linear behaviour for temperature was expected to be observed with increase of the laser power. However, a significant increase of the temperature was found when the laser power was increased from 0.84 kW to 0.88 kW. To understand this behaviour, the same experiments were carried out using Ni-plated steel without the Mg alloy. The results are shown with a dashed line in Figure 7-1. Interestingly, a reasonable continuous and monotonic increase of temperature with increased laser power with almost linear behaviour was observed. These results suggest that the cause of the significant increase in the temperature-power profile above 0.84 kW power could be related to a possible exothermic reactions when the Ni-plated steel and Mg alloy are in contact. Further microstructural analyses, discussed in the subsequent sections, were performed to aid in studying this hypothesis.

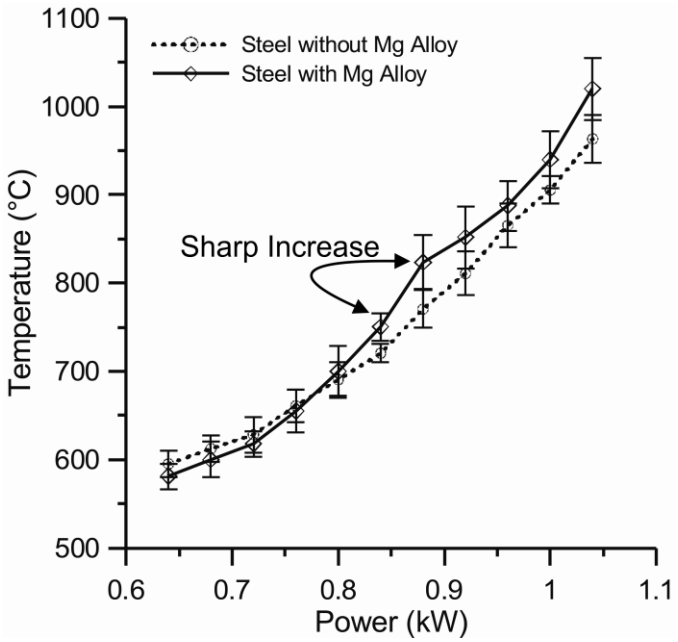

Figure 7-1: The peak temperature of the wetting tests versus laser beam power is shown.

7.2 Contact Angle *vs*. Temperature

The measured contact angle of the Mg alloy bead as a function of peak temperature for the AZ92 Mg alloy on Ni-plated steel is shown in Figure 7-2. The contact angle of the alloy started from an initial value of about 88º at peak temperature of 618 ºC. From this temperature, the contact angle remained almost constant for temperatures up to 750 ºC. This stage was denoted as the first wetting mode in this study (*i.e.*, Mode I). When the temperature was increased above 750 ºC, a sharp drop in the contact angle value was observed from around 85º to 47º and it again remained constant for increasing temperatures up to 1020 ºC. The wetting behaviour in this temperature range was denoted as the second wetting mode (*i.e.*, Mode II). Cross-sectional views of the wetting samples at laser beam powers of 0.72 kW (in Mode I) and 0.92 kW (in Mode II) are presented in Figure 7-2. Peak temperatures above this value in the wetting experiments resulted in evaporation of magnesium as well as oxidation of liquid magnesium with excessive expulsion. Therefore, higher powers and temperatures were not explored further.

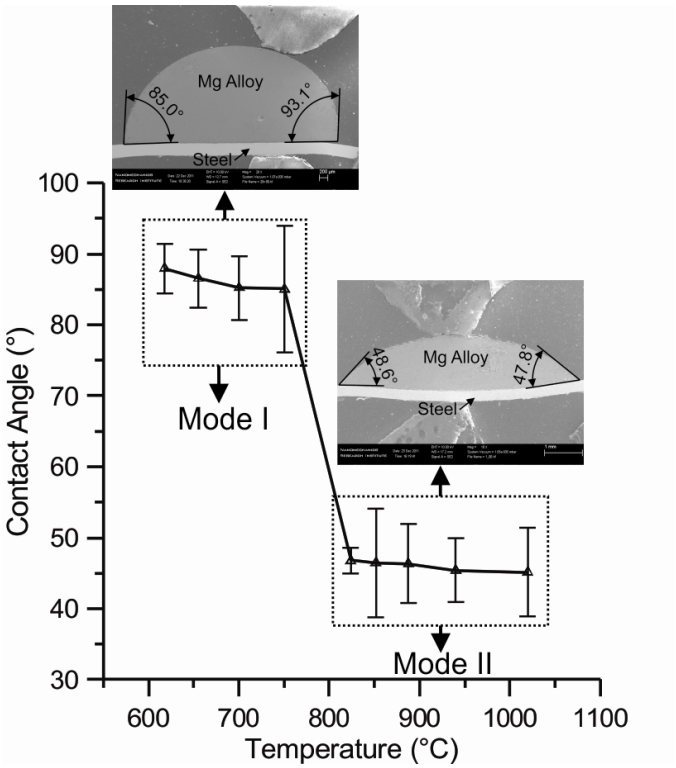

Figure 7-2: The contact angle as a function of the peak temperature during wetting experiments is shown.

As a general result, a slight decrease of the contact angle with increasing temperature in each wetting mode was also observed (~ 2.9º and 1.6º for Modes I and II, respectively), indicating the effect of temperature on the improvement of the wetting [48]. However, the temperature driven change in contact angle was not significant compared to the sharp drop of the contact angle from Mode I to Mode II (~ 38.3º).

7.3 Interfacial Reaction Products

To evaluate phases (reaction products) formed along the Mg alloy-steel interface in each wetting mode, microstructural analysis of the interfaces were performed.

7.3.1 Mode I (618-750 ºC)

Figure 7-3 shows the SEM micrographs of the Mg alloy-substrate interface of the wettability samples in the temperature range of 618-750 ºC (Mode I). In this mode, microstructural analysis of the interface (see Figure 7-3a-d) confirmed that an additional phase had formed along the Mg alloy-substrate interface. Figure 7-3e and f shows a TEM image and the selected area diffraction patterns (SADP) of the interfacial phase, respectively. The diffraction pattern showed a standard pattern of AlNi (with BCC crystal structure) with the [011] zone axis of the particle. According to the EDS analysis results, these faceted dendritic-shaped phases contained 49.6±1.3 at.% Ni, 45.4±4.7 at.% Al, and 5.0±2.5 at.% Mg, confirming that the phases identified in Figure 7-3a-d were mainly composed of the AlNi intermetallic compound. It has been reported that each of the Al-Ni binary intermetallic compounds have some solubility for substitutional magnesium atoms [90].

Continuous growth of the AlNi layer was found with increasing peak temperature. This phase formed as a result of a chemical reaction between Al from the molten Mg alloy and the Ni layer. When this AlNi phase formed, growth occurred via a diffusion mechanism at the interface from 0.5 µm thick at 618 ºC to 1.1 µm thick at 750 ºC. It is worth noting that the Ni layer still existed between the created AlNi layer and steel in this temperature range.

Figure 7-4 shows bright field TEM images of the Mg alloy-Ni interface in Mode I. The TEM analysis of the AlNi-Ni interface showed that the AlNi phase did not grow on the Ni, but instead nucleated and grew as a continuous layer adjacent to the interface. As shown in Figure 7-4a and b, a continuous interlayer (100-400 nm thick) phase was observed along the interface between the AlNi phase and Ni. Higher magnification of this layer (shown in Figure 7-4b) confirmed good bonding between this layer and AlNi as well as to the Ni. To analyze the composition of the interfacial phase, scanning transmission electron microscopy (STEM)-EDS was used. The results showed that the interfacial layer contained an average of 65.8 ± 7.1 at.% Mg and 34.2 ± 8.9 at.% Ni.

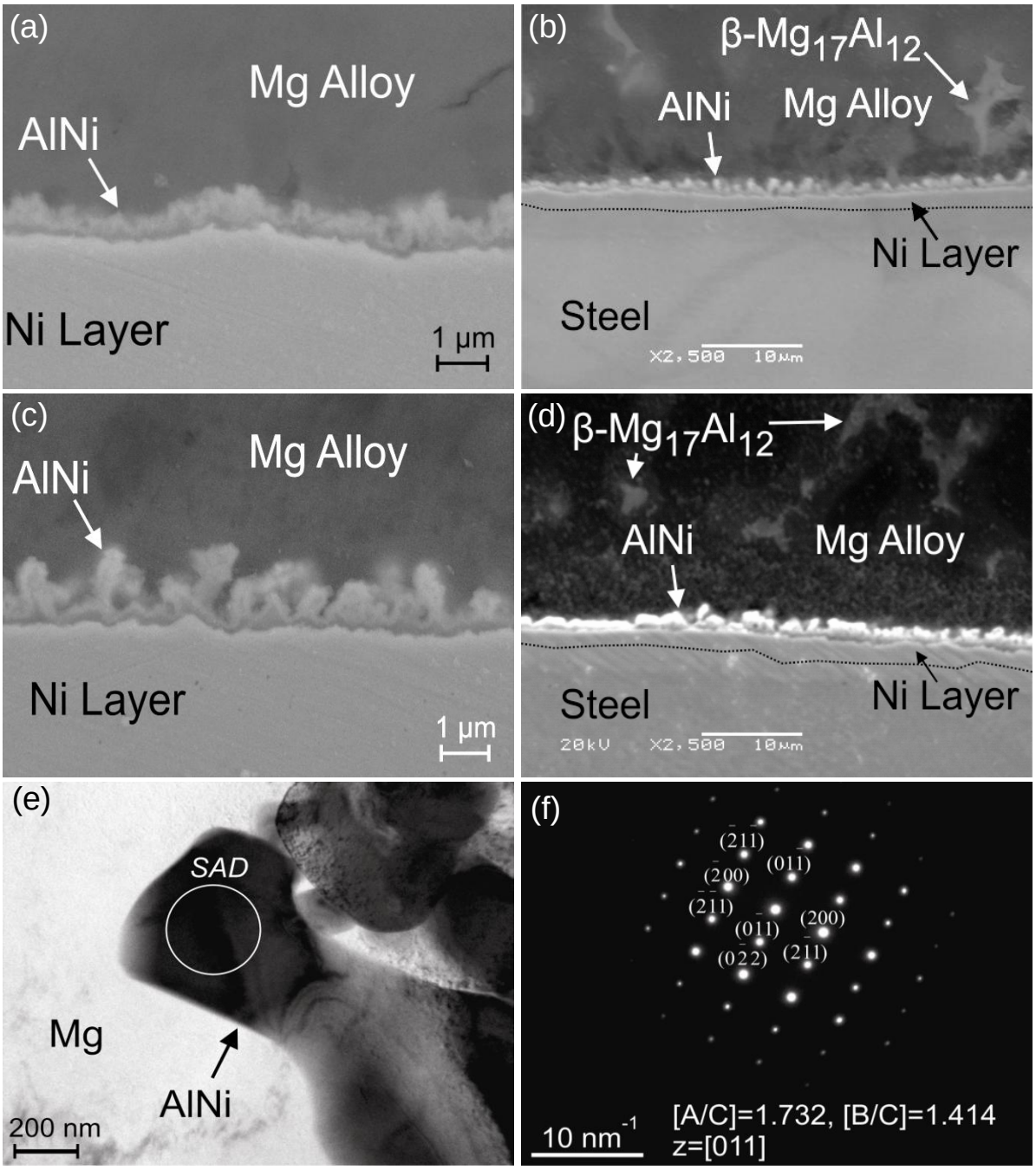

Figure 7-3: The SEM micrographs of the Mg alloy-steel interface of the wetting sample at peak temperatures of (a) 618 ºC, (b) 655 ºC, (c) 700 ºC, (d) 750 ºC, (e) TEM image of AlNi particle, and (f) SADP in the [011] zone axis of AlNi particle.

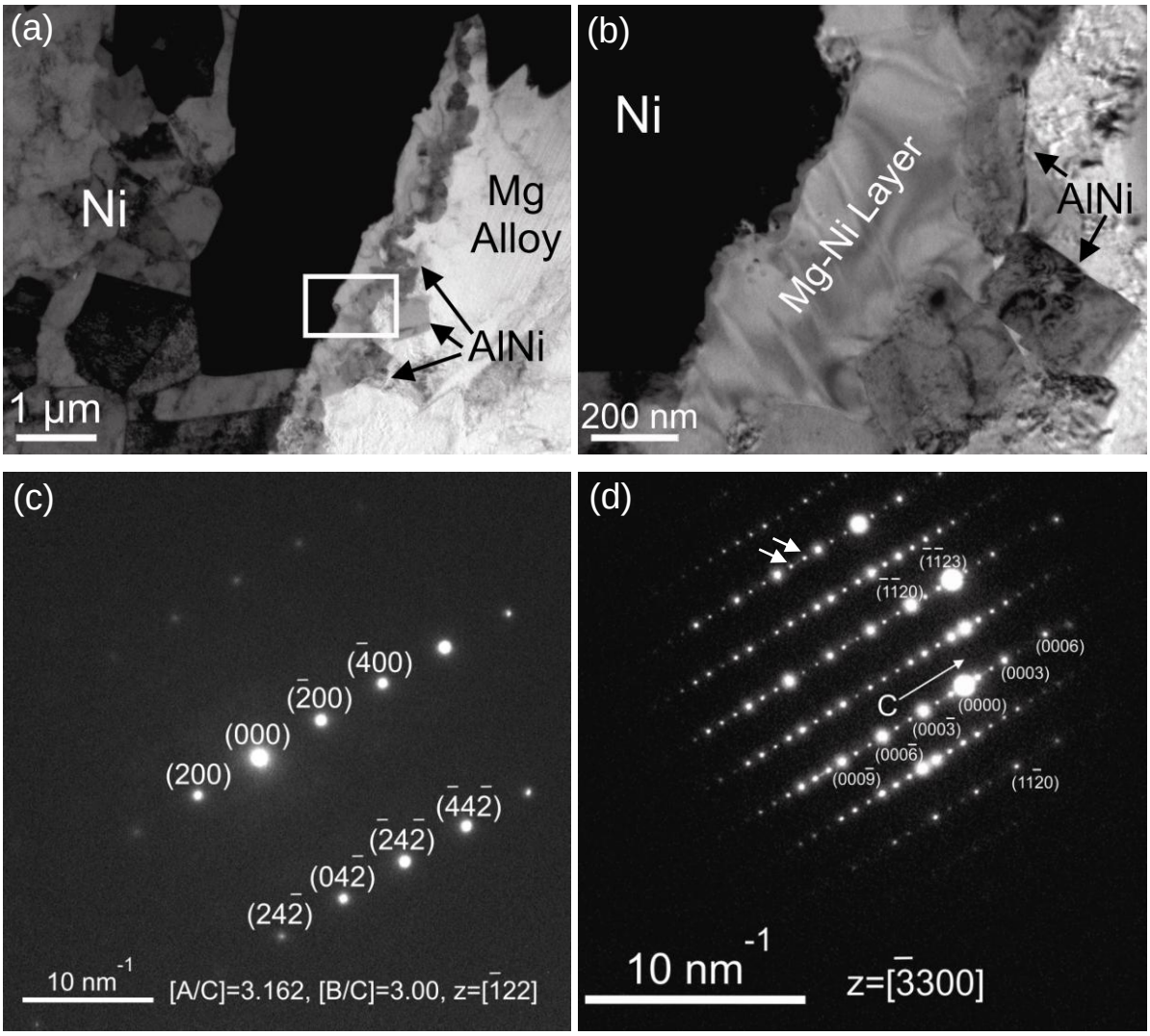

Figure 7-4: (a) and (b) TEM images of the Mg alloy-Ni coated steel interface at different magnifications, (c) the SADP of the Ni grain substrate, when incident beam was parallel to $[\bar{1}22]_{Ni}$ and (d) the corresponding SADP of the formed Mg-Ni phase at the interface, when the incident beam was parallel to $[\bar{3}300]_{Mg-Ni}$.

To identify this Mg-Ni layer, SADP analysis of this layer was performed. Figure 7-4c and d show the SADP analysis of the Ni grain and Mg-Ni phase, respectively, when the incident beam was parallel to $[\bar{3}300]$ zone axis of the Mg-Ni phase. The interfacial phase in between AlNi phase and Ni electro-deposited layer corresponded to Mg_2Ni with Hexagonal

Close-Packed (HCP) crystal structure. Therefore, in Mode I, nano-scale layers of AlNi + Mg_2Ni reaction products were produced between the Mg and steel. As a result, AlNi phase was identified as the reaction product in contact with the Mg alloy.

7.3.2 Mode II (824-1020 ºC)

Figure 7-5 shows the SEM photomicrographs of the Mg alloy-substrate interface for the temperature range of 824-1020 ºC (Mode II). In this mode, the Ni coating was not detected as a separate layer along the interface after the wetting test and it was completely melted and dissolved into the Mg alloy (see Figure 7-5). As a result, a high volume fraction of AlNi was formed close to the interface in the molten area. The continuous growth of the AlNi was observed at the interface. Formation of diamond shaped AlNi particles even far from the interface confirmed diffusion of Ni atoms into the Mg alloy (see Figure 7-5h). Therefore, the test duration and temperature were high enough for the entire Ni coating to melt and diffuse into the Mg alloy and as a result, AlNi particles crystallized even in the center of the molten region. For formation of AlNi, Al atoms from the Mg alloy react with the diffused Ni atoms from the interface. Therefore, AlNi particles are surrounded by Mg-Al alloy depleted in Al, shown as a dark gray phase around each AlNi particle.

Figure 7-6a shows a STEM image of the steel-Mg alloy interface from the specimen in Mode II. Growth of an intermediate phase was also found at the interface on the Fe grains. To identify the composition of the phase(s) formed along the Mg alloy-steel interface, EDS mapping and line scan analysis were used, as shown in Figure 7-6b and c, respectively. Representative concentration maps for Mg, Al, Ni, and Fe elements from the area shown in Figure 7-6a confirmed high concentrations of Al and Ni at the interface. The distribution of elements across the interface (Figure 7-6c) showed that the interfacial phase contained 40.6±0.7 at.% Ni, 51.1±2.5 at.% Al, and 8.1±2.6 at.% Fe, confirming that the interfacial phase in Figure 7-6a was mainly composed of AlNi intermetallic compound. The results also showed some diffusion of Ni and Al into the Fe as a result of high temperature experienced during the wetting experiment. SADP analysis also identified the phase as AlNi. Therefore, in Mode II, AlNi was the only reaction product between Mg and steel.

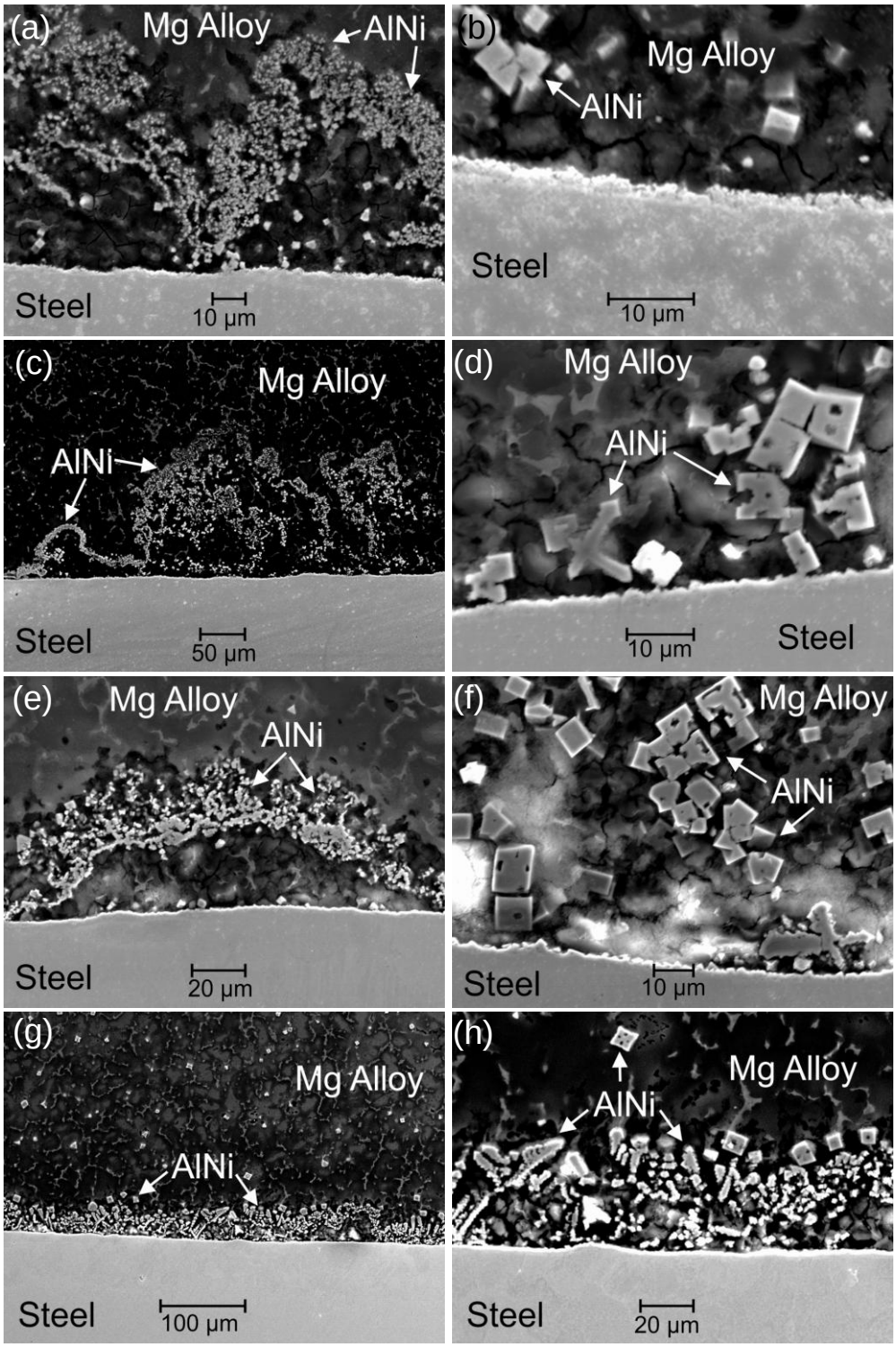

Figure 7-5: The SEM micrographs of the fusion zone-substrate interface of the wettability samples at peak temperatures of (a) and (b) 824 ºC, (c) and (d) 852 ºC, (e) and (f) 888 ºC, (g) and (h) 940 ºC.

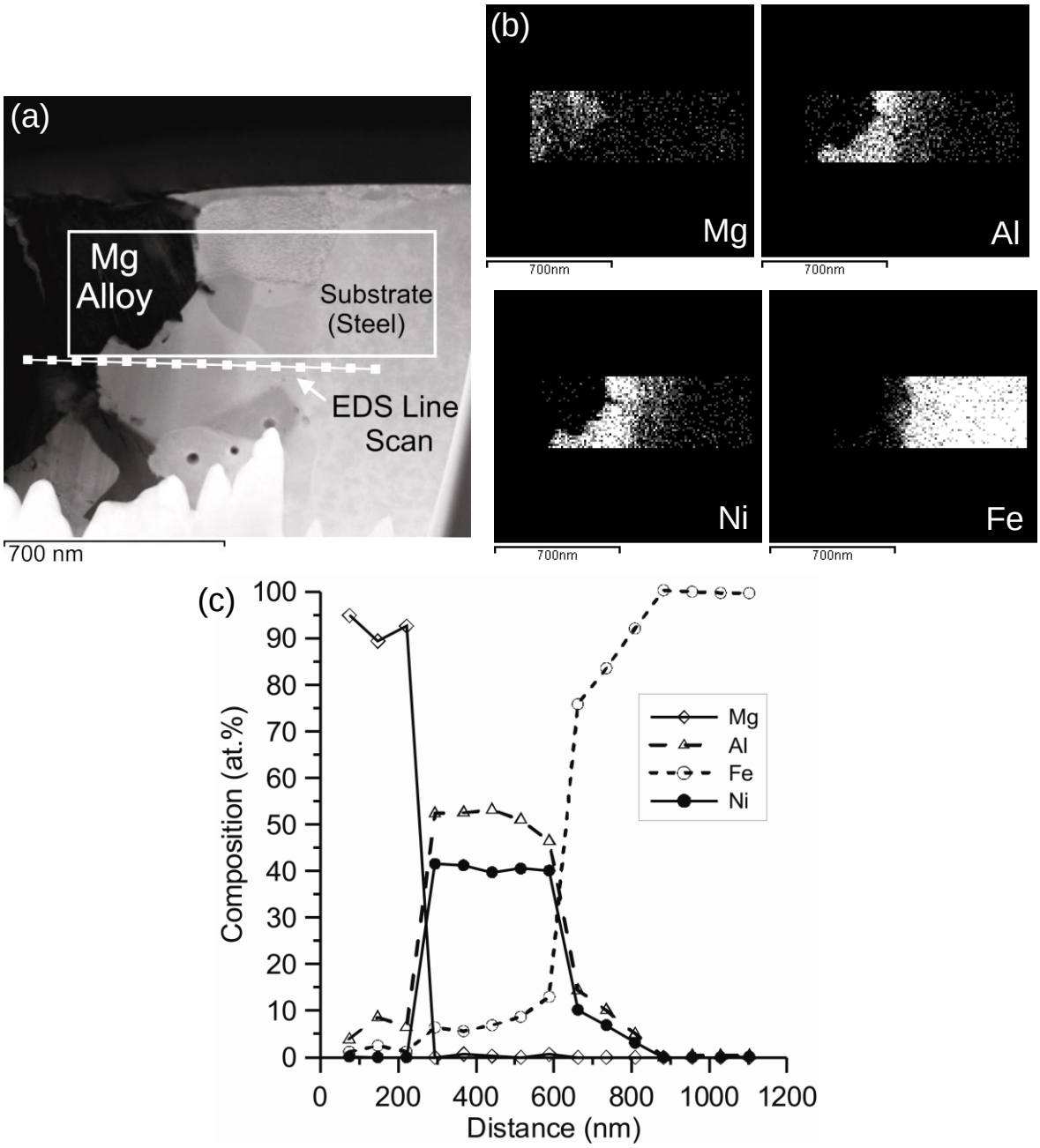

Figure 7-6: (a) STEM image of Mg alloy-steel interface showing grains of the interfacial phase, (b) representative concentration maps of Mg, Al, Ni, and Fe elements across the interface, and (c) STEM-EDS point analysis results across the shown line in b.

As discussed in Section 7.1.1, a significant increase of the temperature was observed in Figure 7-1 when the laser power was increased from 0.84 kW (with slight formation of AlNi) to 0.88 kW (with heavily nucleation of AlNi). Gasparyan and Shteinberg [109] used a specially designed differential thermal analysis (DTA) to show that reactions between Al and Ni are highly exothermic. The heat provided during these wetting tests by laser can initiate exothermic reactions. Therefore, the exothermic nature of the Al-Ni interaction was the mechanism behind the increase of the peak temperature when the laser power was high enough to initiate this reaction. The released heat is dependent on the volume fraction of the precipitated AlNi phase, which significantly increased when the laser powered increased from 0.84 kW to 0.88 kW (compare Figure 7-3 and Figure 7-5). In addition, the partial enthalpies of mixing of Al-Ni reactions are high [109]. These phenomena generate high local temperatures near the steel-Mg alloy interface leading to the sharp increase of the peak temperature recorded in Figure 7-1.

The reaction products formed in the temperature range of 618-1020 ºC are in agreement with the predicted phase stability map presented in Figure 5-5 [87]. AlNi+Mg_2Ni and AlNi were predicted to form along the Mg alloy-steel interface in the temperature range of 600-750 ºC and 750-1100 ºC, respectively [87]. In Mode I, peak temperature and time are just enough for partial melting of the Ni layer. As shown in Figure 5-5, nucleation and growth of the AlNi in the Mg alloy occur only where % $Ni_{0.9}Steel_{0.1}$ is less than 72%, leaving Mg-Ni rich liquid adjacent to the Ni surface. This follows by nucleation and growth of Mg_2Ni on the Ni at $T \leq 725$ °C that impacts on the AlNi at no particular OR. Similar reaction products (AlNi + Mg_2Ni) were observed at the bottom of a laser brazed Ni electro-plated steel-AZ92 Mg alloy joint interface, as shown in Figure 5-11. In Mode II, peak temperature and time are high enough for complete melting, mixing and diffusing of the Ni layer into the Mg alloy. Similar to the Mode I, solidification starts with nucleation and growth of the AlNi where % $Ni_{0.9}Steel_{0.1} \leq 72\%$, not just in the Mg alloy but also on the steel surface. This indicates that % $Ni_{0.9}Steel_{0.1}$ in the liquid adjacent to the interface is always less than 72%, even on the steel surface. Therefore, in Mode II, the condition for formation of Mg_2Ni (% $Ni_{0.9}Steel_{0.1} \geq 72\%$) during cooling is never satisfied. This was consistent with the observed

interfacial microstructure of the laser brazed Ni electro-plated steel-AZ92 Mg alloy joint, where just AlNi formed at the interface from the middle of the joint to the top side of the single flare bevel lap joint (see Figure 5-7).

In this study, different contact angles at temperatures higher than 618 ºC were associated with the formation of different reaction products between the Mg alloy and steel. In Mode I (618 ºC ≤ T_{max} ≤ 750 ºC), the Ni-plated steel was covered by a continuous layer of Mg_2Ni, which extended across the solid-liquid interface. However, the AlNi layer on top of Mg_2Ni was the phase in contact with the remaining liquid (Mg alloy). In comparison, in Mode II (824 ºC ≤ T_{max} ≤ 1020 ºC), the steel was covered by a continuous layer of the AlNi compound. Therefore, in both Modes I and II, the reaction product in contact with the Mg alloy was the AlNi phase, but the contact angle differed greatly in these two cases. Similar to the spreading behaviour observed by Saiz *et al*. [54], this phenomenon cannot be explained using previously proposed wetting mechanisms for metallic-metallic reactive systems. In the following section, the mechanism behind the two different wetting modes will be investigated in order to identify the factors that affect the reactive wetting in this metallic-metallic system.

7.4 Lattice Mismatching between Reaction Products and Substrates

7.4.1 Mode I (Mg-AlNi-Mg_2Ni-Ni-Fe)

For both Modes I and II, AlNi is the first precipitated phase from the liquid. Therefore, after formation of this phase along the interface, the remaining liquid will be in direct contact with AlNi and this phase plays the role of substrate for the remaining liquid. As a result, the Mg-AlNi interface will form after solidification in both wetting modes, meaning the energy of this interface cannot be the driving force for the wetting nor explain the observed difference in the wetting behaviour in this system.

The lattice matching and crystal orientations at the Mg-AlNi interface were studied using a series of SADP analyses as well as HR-TEM examinations. As shown in Figure 7-7, the SADP of the AlNi phase was taken in the direction along the zone axis of $[011]_{AlNi}$. The

diffraction pattern of the Mg phase with a ring pattern showed that the *d*-value of the $\{20\bar{2}0\}_{Mg}$ and $\{11\bar{2}2\}_{Mg}$ planes are the same as that of $(200)_{AlNi}$ and $(02\bar{2})_{AlNi}$, respectively (see Figure 7-7c). Figure 7-7d shows the HR-TEM image of Mg-AlNi interface. When $[001]_{AlNi}//[01\bar{1}1]_{Mg}$, the orientation relationship (OR) of AlNi phase and Mg was found to be $\{10\bar{1}1\}_{Mg}$ 113.1º from $\{110\}_{AlNi}$ (see Figure 7-7d). The measured interplanar spacings were 2.423 Å and 2.070 Å for $\{10\bar{1}1\}_{Mg}$ and $\{110\}_{AlNi}$, respectively, which provides 17 % interplanar mismatch at the interface.

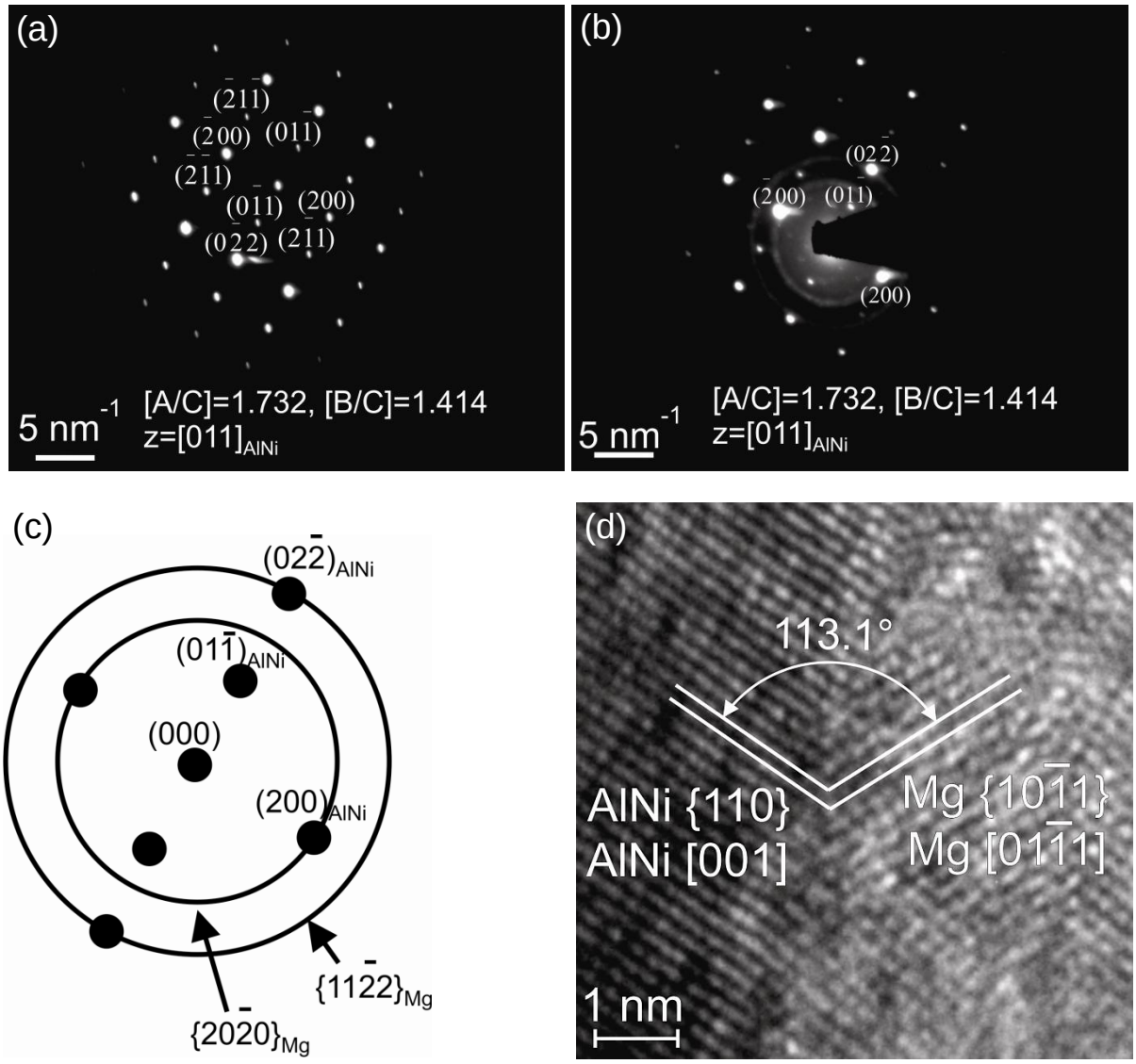

Figure 7-7: (a) The SADP of the AlNi grain, when incident beam was parallel to $[011]_{AlNi}$, (b) the corresponding SADP of the Mg-AlNi interface, (c) the schematic representing OR between Mg and AlNi grain at the interface, and (d) HR-TEM image of Mg-AlNi interface.

Moving from the Mg-AlNi interface to the substrate direction, the next interface formed during solidification was the AlNi-Mg_2Ni interface. SADP analysis of this interface did not show any overlapping diffraction spots, meaning no specific OR was found between these two phases at their interface. Figure 7-8 shows the HR-TEM image of the AlNi-Mg_2Ni

interface, when $[001]_{AlNi} // [0001]_{Mg_2Ni}$. The crystallographic orientation between the AlNi and Mg_2Ni phases in this site was determined to be $\{110\}_{AlNi}$ 25.0° from $\{10\bar{1}0\}_{Mg_2Ni}$ and the measured interplanar spacing for these planes were $d_{\{110\}AlNi}$ = 2.10 Å and $d_{\{10\bar{1}0\}Mg_2Ni} = 4.290$ Å, which provides 104.3 % interplanar mismatch at the interface. Therefore, the HR-TEM results did not show an OR with low mismatch strain in the AlNi-Mg_2Ni adjoining lattices.

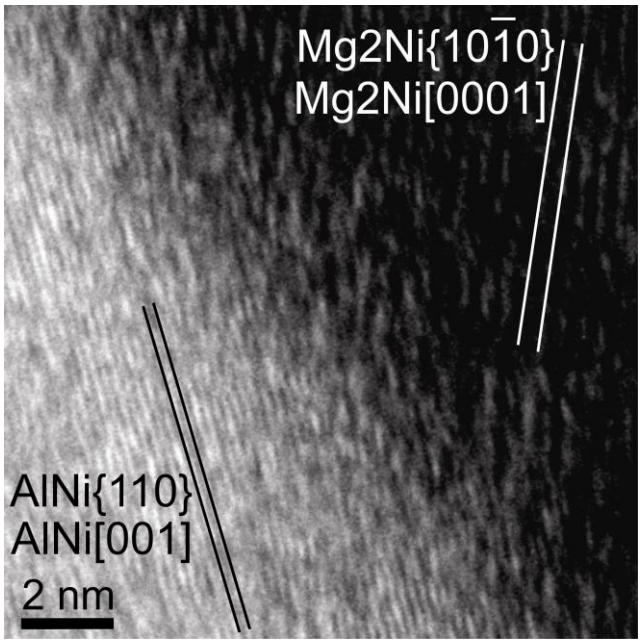

Figure 7-8: HR-TEM image of the AlNi-Mg_2Ni interface.

In Mode I, Mg_2Ni is also in contact with the Ni layer from the other side. The SADP analysis of the Mg_2Ni-Ni interface (shown in Figure 7-4d and Figure 7-9) confirmed that the lattice of the Ni was exactly located on the $[\bar{1}22]$ zone axis, when the Mg_2Ni phase was parallel to the $[\bar{3}300]$ zone axis. This result implies that the OR between the Ni grain and formed Mg_2Ni phase at the interface was $[\bar{3}300]_{Mg_2Ni} // [\bar{1}22]_{Ni}$. However, none of the Mg_2Ni diffraction spots were superimposed with Ni diffraction spots (see Figure 7-9b), meaning that none of the diffracted planes in Figure 7-9b were parallel to each other, when the electron beam was parallel to the $[\bar{1}22]$ zone axis of the Ni.

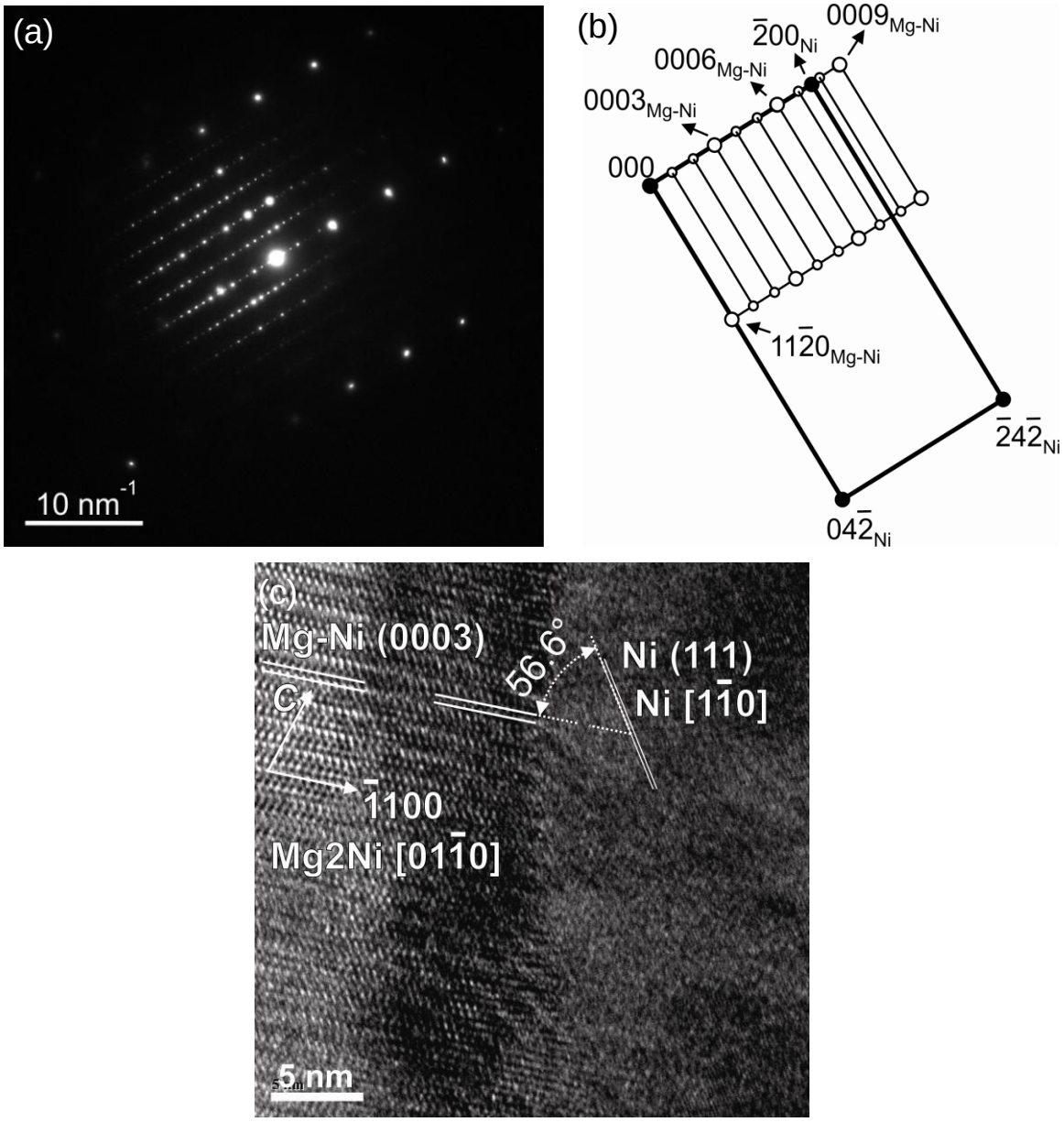

Figure 7-9: (a) SADP of the Mg_2Ni-Ni interface, (b) the schematic representing OR between Mg_2Ni phase and Ni grain at the interface ($[\bar{3}300]_{Mg_2Ni}$ // $[\bar{1}22]_{Ni}$), and (c) HR-TEM image of Mg_2Ni-Ni interface showing the matching planes and crystal orientation at the interface.

Figure 7-9c shows the HR-TEM image of the Mg_2Ni-Ni interface showing the matching planes and crystal orientation between Mg_2Ni and Ni, when $\left[01\bar{1}0\right]_{Mg_2Ni} // \left[1\bar{1}0\right]_{Ni}$. According to this HR analysis, reference to HCP crystal structure for the Mg_2Ni phase, the *d*-

spacing of the parallel planes of the Mg_2Ni phase shown in Figure 7-9c was measured to be 1.324 nm, which is close to the published *c*-value of the Mg_2Ni phase (at 44.2 at.% Ni, a_{Mg2Ni} = 0.518 nm, c_{Mg2Ni} = 1.319 nm [110]). Therefore, the parallel planes of Mg_2Ni phase in Figure 7-9c correspond to the (0001) planes (basal planes in HCP). However, the SADP of this phase shows extra reflection spots at positions of n/3 $(0003)_{HCP}$ (n is an integer), as marked with the arrow heads in Figure 7-4d. This diffraction pattern of the interfacial phase shows a Long Period Ordered (LPO) structure [111]. This phase has basically an ordered hexagonal crystal lattice, but the stacking order of the close-packed planes is modulated in the [0001] or [0003] direction at every third layer and the stacking sequence can thus be described as ABB (see Figure 7-10). Due to ABBABB… modulation, the original reciprocal lattice points are split into three in the direction of the modulation, [0003]. A characteristic of the split spots is that they always lie on the same levels in the direction of the [0001] axis of stacking and divide the distance between the origin and (0003) spot into three segments. An arrangement of bright dots in the HR-TEM image of Figure 7-10a clearly indicates the stacking sequence of ABBABB… with a period of 1.324 nm. Therefore, when considering the ordering of the atoms, the distribution of the superlattice spots in the Mg_2Ni interfacial phase did not agree with the distribution of the normal HCP lattice spots (see Figure 7-10). Considering the distortion from the 2H-type (ABAB…) period ordered structure, the present long-period ordered structure of the Mg_2Ni phase can be described by a hexagonal lattice with a_H = 0.518 nm and c_H = 1.324 nm, as shown in Figure 7-10b and the reflections have been indexed accordingly.

The HR-TEM image (Figure 7-9c) indicated that the crystallographic OR between the reaction product (Mg_2Ni phase) and the substrate (Ni layer) in this site was determined to be $\{0003\}_{Mg_2Ni}$ 56.6º from $\{111\}_{Ni}$ and the measured interplanar spacing for these planes were $d_{\{0003\}Mg2Ni}$ = 4.415 Å and $d_{\{111\}Ni}$ = 2.060 Å, which provides 114 % interplanar mismatch at the interface. Therefore, the SADP analysis and also HR-TEM results did not show an OR with low mismatch strain in the Mg_2Ni-Ni adjoining lattices.

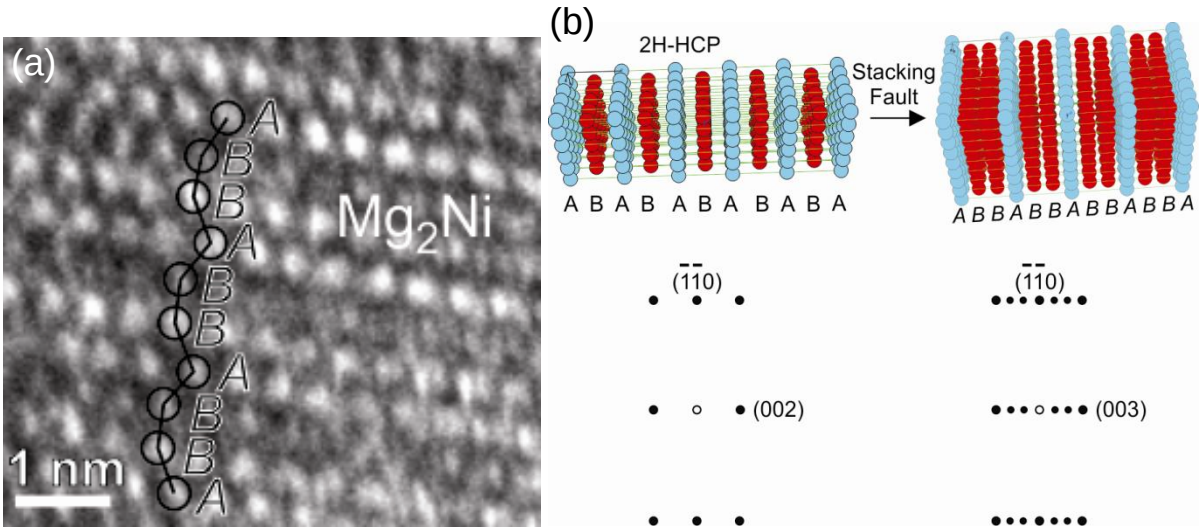

Figure 7-10: (a) HR-TEM image of Mg_2Ni phase and (b) schematic illustration showing a structural relationship between the HCP-Mg_2Ni (2H-type) and long period ordered Mg_2Ni observed in this study, together with the corresponding computed SADPs. The Mg_2Ni atomic structure model was constructed using Mg_2Ni lattice parameters (a_{HCP} = 0.518 nm and c_{HCP} = 1.324 nm).

Due to extensive solid solubility of Ni and Fe into each other (a continuous solid solution with unlimited solubility is formed between Ni and Fe at high temperature [110]), thus defining a distinct interface between the Ni layer and Fe, where their adjoining lattices meet, was not possible. This solubility minimizes the mismatch strain between Ni and Fe.

7.4.2 Mode II (Mg-AlNi-Fe)

Figure 7-11 shows a HR-TEM image of the Mg-AlNi interface in Mode II. In this mode, an OR similar to that between Mg and AlNi in Mode I was found (when $[001]_{AlNi} // [01\bar{1}1]_{Mg}$, $\{10\bar{1}1\}_{Mg}$ 95.3º from $\{110\}_{AlNi}$ (see Figure 7-11)). The measured interplanar spacings were 2.402 Å and 2.041 Å for $\{10\bar{1}1\}_{Mg}$ and $\{110\}_{AlNi}$, respectively, which provides 18 % interplanar mismatch at the interface.

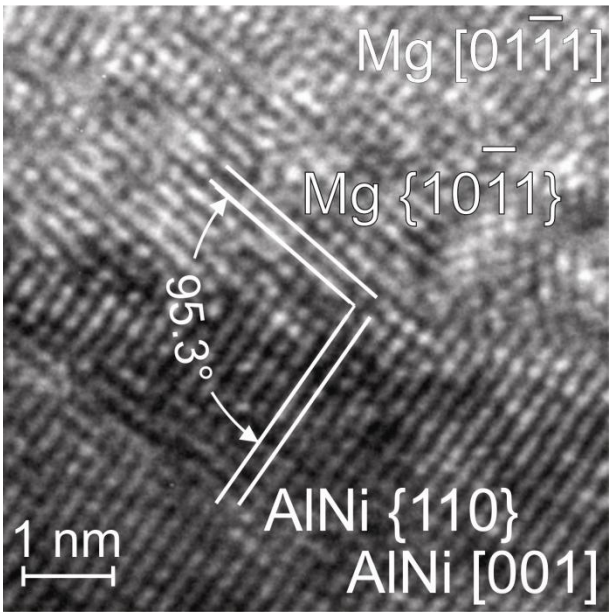

Figure 7-11: HR-TEM image of the Mg-AlNi interface in Mode II.

To analyze the AlNi-Fe interface, SADP and HR-TEM analysis of this interface were also performed. Figure 7-12 shows a TEM image of one AlNi grain formed as the reaction product at the interface surrounded by Fe grains from the substrate. In this area both AlNi and Fe were single crystals (one grain). In order to identify the OR between the AlNi phase and the Fe grain, first the TEM foil was tilted until the incident beam was parallel to the [011] zone axis of the Fe grain, as shown in Figure 7-12a and the SADP shown in Figure 7-12b was taken from the Fe grain. Then without changing the orientation of the beam and specimen with respect to each other, the SADP of the AlNi grain and also the AlNi-Fe interface were taken, as shown in Figure 7-12c and Figure 7-12d, respectively. These results showed that the grain of the AlNi phase was exactly located on the $[011]_{AlNi}$ zone axis, when Fe was parallel to $[011]_{Fe}$ zone axis. These results imply that the OR between the AlNi interfacial phase and Fe grain (both having BCC crystal structure) at their interface was $[011]_{AlNi} // [011]_{Fe}$. Furthermore, the diffraction spot of $(\bar{2}\bar{1}1)_{Fe}$ was superimposed with that

of $(\bar{2}00)_{AlNi}$, as shown in Figure 7-12d and Figure 7-12e. This indicates that the crystallographic plane relationship between the formed AlNi grain at the interface and Fe grain in this site was $(\bar{2}00)_{AlNi} // (\bar{2}\bar{1}1)_{Fe}$.

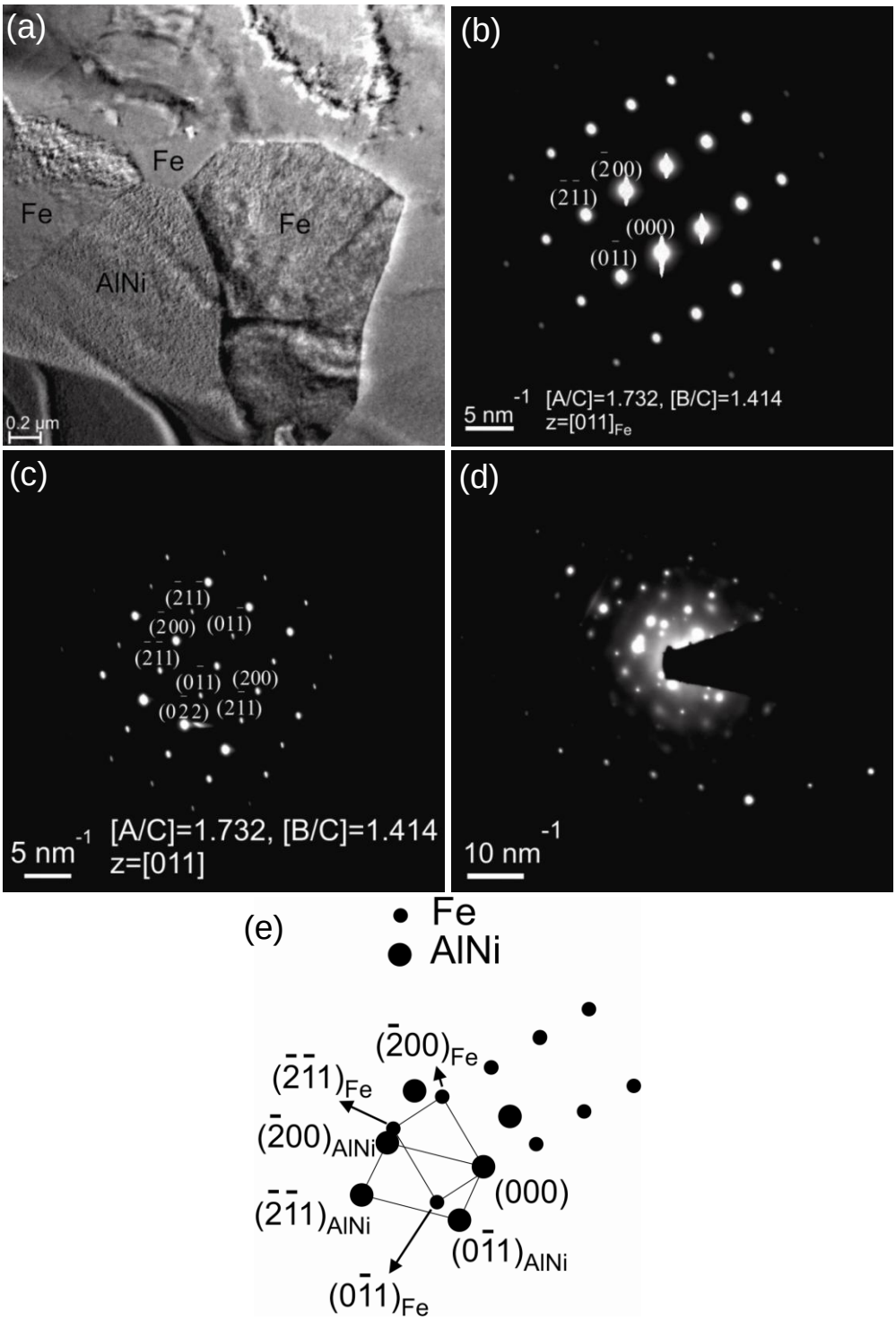

Figure 7-12: (a) TEM image of the AlNi and Fe grains at the interface of Mg alloy-steel, (b) SADP of Fe grain, (c) the corresponding SADP of AlNi grain, (d) SADP of the AlNi-Fe interface (incident beam was parallel to $[011]_{AlNi}$//$[011]_{Fe}$), and (e) the schematic showing the OR between AlNi and Fe grains at the interface.

Figure 7-13 shows the HR-TEM image of the AlNi-Fe interface. The boundary between these two phases was very smooth and difficult to distinguish due to good lattice plane matching between Fe and AlNi at the interface. This HR-TEM image also indicates that the crystallographic OR between the formed AlNi grain (reaction product) and Fe grain (substrate) at the interface in this site is $\{110\}_{AlNi}$ 99° from $\{110\}_{Fe}$, when $[001]_{AlNi} // [001]_{Fe}$.

The HR-TEM image indicated that the measured interplanar spacing for these planes were $d_{\{110\}Fe}$ = 2.151 Å and $d_{\{110\}AlNi}$ = 2.046 Å, which provides 5 % interplanar mismatch at the interface. Therefore, the SADP analysis and also HR-TEM results confirmed a low interfacial mismatch strain between AlNi phase and Fe.

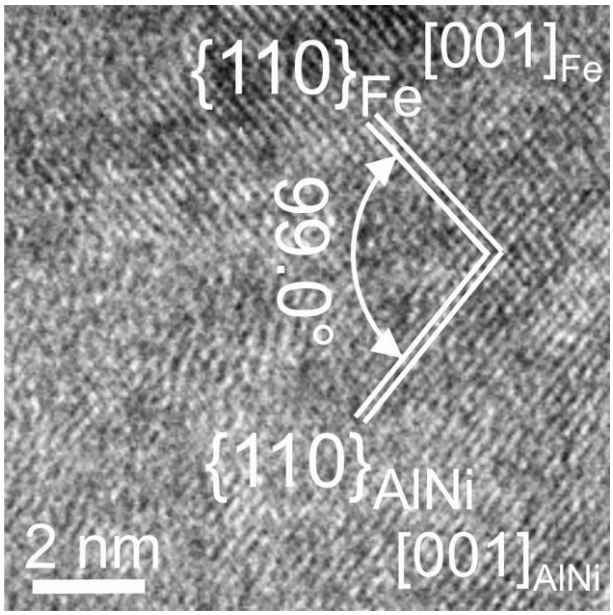

Figure 7-13: HR-TEM image of the AlNi-Fe interface.

7.5 Theoretical Edge-to-Edge Calculation Results

The edge-to-edge crystallographic model was used to analyze the interatomic spacing misfit along matching directions and interplanar spacing mismatch between matching planes for the

different interfaces formed. The calculation procedure and the results of the interatomic spacing misfits along matching directions and interplanar spacing mismatches between matching planes for different formed interfaces in this study are given in the Appendix (see Section A.4).

In Mode I, the calculated minimum interplanar mismatch was found to be 16.4% $_{\{Mg\text{-}AlNi\}}$-108.3% $_{\{AlNi\text{-}Mg2Ni\}}$-17.2% $_{\{Mg2Ni\text{-}Ni\}}$. These results showed that no possible pair of planes between Mg_2Ni phase and Ni from one side and AlNi from the other side was found to form an OR with low mismatch strain in their adjoining lattices. These predicted results are in agreement with the observed interplanar mismatch for the different interfaces formed in Mode I, as shown in Figure 7-7, Figure 7-9 and Figure 7-10 (17% $_{\{Mg\text{-}AlNi\}}$-104.3% $_{\{AlNi\text{-}Mg2Ni\}}$-114% $_{\{Mg2Ni\text{-}Ni\}}$). Therefore, the Mg_2Ni phase tolerates high interfacial mismatch strain energy at both interfaces. This causes poor wetting of Ni by Mg when Mg_2Ni phase forms as the reaction product between the AlNi and Ni. The results of the AlNi (BCC)-Mg (HCP) interface also showed that there is no close-packed plane pair between AlNi and Mg with low mismatch strain.

In Mode II, the calculated minimum interplanar mismatch was found to be 16.4% $_{\{Mg\text{-}AlNi\}}$-0.6% $_{\{AlNi\text{-}Fe\}}$. This leads to a low interfacial energy that promoted the wetting of the Fe substrate by the Mg when AlNi phase forms as the reaction product on the substrate. The experimental results presented in Figure 7-11 and Figure 7-13 also confirmed that low mismatch strain exists between the Fe substrate and AlNi phase at the interface (18% $_{\{Mg\text{-}AlNi\}}$-5% $_{\{AlNi\text{-}Fe\}}$).

Table 7-1 summarizes the wetting behaviour of the Ni electro-plated steel by the molten Mg alloy in the different wetting modes analyzed in the current study. The results presented in this study for a strong interaction metallic-metallic system proved that the wetting behaviour can be very much affected by the reaction products, which are not even in direct contact with the liquid phase; *i.e.*, Mg_2Ni in this study. More specifically, the lattice mismatching between the different reaction products, and the reaction product and the substrate play a major role in the reactive wetting process. Lattice mismatch between the

reaction products themselves or a reaction product and a substrate might prevent the wetting of the substrate by the liquid.

Table 7-1: Wetting behaviour of the Ni plated steel by the Mg alloy in the different wetting modes

Temperature Range (ºC)	$618 \leq T \leq 750$ (Mode I)	$824 \leq T \leq 1020$ (Mode II)
Contact Angle (º)	86	46
Mg-Reaction Product(s)-Substrate	Mg-AlNi-Mg_2Ni-Ni-Fe	Mg-AlNi-Fe
Interplanar Mismatch from HR-TEM	17% $_{\{Mg\text{-}AlNi\}}$-104.3% $_{\{AlNi\text{-}Mg2Ni\}}$-114% $_{\{Mg2Ni\text{-}Ni\}}$	18% $_{\{Mg\text{-}AlNi\}}$-5% $_{\{AlNi\text{-}Fe\}}$
Minimum Interplanar Mismatch from Edge-to-Edge Model	16.4% $_{\{Mg\text{-}AlNi\}}$-108.3% $_{\{AlNi\text{-}Mg2Ni\}}$-17.2% $_{\{Mg2Ni\text{-}Ni\}}$	16.4% $_{\{Mg\text{-}AlNi\}}$-0.6% $_{\{AlNi\text{-}Fe\}}$

Possible Matching Plane Pairs (Mismatch < 6 %) from Edge-to-Edge Model	None	$\{110\}_{AlNi} // \{110\}_{Fe}$
		$\{200\}_{AlNi} // \{200\}_{Fe}$
		$\{111\}_{AlNi} // \{111\}_{Fe}$

7.6 Chapter Summary

In this chapter, the effect of interfacial lattice mismatching between reaction products and the substrate on wetting of the molten Mg alloy on the Ni-plated steel was investigated. The wetting has been characterized by measuring the contact angles of AZ92 Mg alloy on Ni electro-plated steel as a function of peak temperature reached during laser heating. Reactions between the molten Mg and Ni led to a contact angle of about 86º in the peak temperature range of 618-750 ºC (denoted as Mode I) and a dramatic decrease to about 46º in the peak temperature range of 824-1020 ºC (denoted as Mode II).

SEM and TEM results indicated that AlNi + Mg_2Ni reaction products were produced between the Mg alloy and steel in Mode I, and just AlNi between Mg and steel in Mode II. From HR-TEM analysis, the measured interplanar mismatches for the different interfaces formed in Modes I and II were 17% $_{\{Mg\text{-}AlNi\}}$-104% $_{\{AlNi\text{-}Mg2Ni\}}$-114% $_{\{Mg2Ni\text{-}Ni\}}$ and 18% $_{\{Mg\text{-}AlNi\}}$-5% $_{\{AlNi\text{-}Fe\}}$, respectively. An edge-to-edge crystallographic model analysis confirmed that Mg_2Ni produced larger lattice mismatching between interfaces with calculated minimum interplanar mismatches of 16.4% $_{\{Mg\text{-}AlNi\}}$-108.3% $_{\{AlNi\text{-}Mg2Ni\}}$-17.2% $_{\{Mg2Ni\text{-}Ni\}}$ for Mode I and

16.4% $_{\{Mg\text{-}AlNi\}}$-0.6% $_{\{AlNi\text{-}Fe\}}$ for Mode II. Therefore, it is suggested that the poor wettability in Mode I was caused by the existence of Mg_2Ni since AlNi was the immediate layer contacting molten Mg in both Modes I and II and the presence of Mg_2Ni increases the interfacial strain energy of the system. This study has clearly demonstrated that the lattice mismatching at the interfaces between reaction product(s) and substrate, which are not in direct contact with the liquid, can greatly influence the wetting of the liquid.

Chapter 8
CONCLUSIONS AND OUTLOOK

In the current thesis, the brazeability of magnesium to steel sheet has been explored. More specifically, development of the laser brazing technology, prediction of early stage phase formation in the steel-interlayer-Mg alloy system during laser brazing, bonding mechanisms in the steel-interlayer-Mg alloy joints, and the mechanism of wetting in steel-interlayer-Mg alloy system were investigated. The benefits of using Al-12Si, Ni and Sn interlayers were explored.

The following sections contain the conclusions of this work and recommendations for future research.

8.1 Conclusions

The conclusions are grouped in accordance to the results and discussion presented in Chapters 4-7.

8.1.1 Laser Brazing of AZ31B to Al Coated Steel Sheet

Brazed joints between AZ31B-H24 Mg alloy and Al-12Si coated steel sheet have been made by a laser brazing process using a Mg-Al-Zn based filler wire in a single flare bevel lap joint configuration. The major conclusions of this study can be summarized as follows:

1. A uniform brazed area with good wetting of base metals was obtained between the AZ31B and Al-Si coated steel sheets using 2.2 kW laser power, 8 mm/s travel speed, 0.2 mm beam offset to the steel side with using He shielding gas with flow rate of 30 l/min.
2. A θ-Fe(Al,Si)$_3$ IMC layer was found at the interface between the steel and its Al-12Si coating layer before brazing. During brazing, the high temperature of the process caused this IMC layer in contact with the coating layer to grow in the form of compact plate-like θ-Fe(Al,Si)$_3$ on the steel side and needle-like τ_5-$Al_{7.2}Fe_{1.8}Si$ phase on the coating layer side.

3. The entire Al-12Si coating layer was melted and taken into solution by the molten brazing alloy, thereby promoting good wetting by the Mg-Al filler metal. However, a non-uniform thickness θ-$FeAl_3$ IMC layer was observed at the steel/braze interface after the process. Formation of this layer confirmed the occurrence of metallurgical bonding between the steel and Mg alloy.
4. The average fracture load of 5 mm wide tensile shear specimens taken form the laser brazed AZ31B-steel joints using Mg-Al filler metal was 767±138 N; representing a 29±5% joint efficiency with respect to shear strength of the AZ31B-H24 Mg alloy. Cracks formed in the thick IMC layer at the bottom of the joints where there was a stress concentration due to the joint geometry. Cracking then moved into the FZ at the upper part of the joint where the IMC layer was thinner or nonexistent.
5. Formation of $FeAl_3$ phase as the reaction product between Mg and Fe resulted in calculated minimum interplanar mismatches of 16.2% $_{\{Mg\text{-}FeAl3\}}$-1.5% $_{\{FeAl3\text{-}Fe\}}$. Therefore, high mismatch strain energy along the Mg-$FeAl_3$ interface, meaning a weak interface, and very low mismatch strain energy along the $FeAl_3$-Fe interface, meaning a strong interface were found.

8.1.2 Laser Brazing of AZ31B to Ni Electro-Plated Steel Sheet

1. A computational thermodynamic analysis using FactSage thermochemical software was used to predict the phases most likely to form along the interface between Ni electro-plated steel and AZ92 Mg alloy (filler metal composition) sheets during the laser brazing process. Calculations were made over a wide temperature and composition range. It was concluded that the addition of the Ni interlayer between the steel and the AZ92 Mg alloy may lead to the formation of the AlNi, Mg_2Ni, and Al_3Ni_2 intermetallic compounds along the steel/fusion zone interface, where the AlNi and Mg_2Ni are most likely to form under non-equilibrium conditions present during laser brazing.
2. With the addition of an electro-deposited Ni interlayer on steel sheet, single flare bevel lap joints of AZ31B-H24 Mg alloy to steel sheet were rendered possible by the laser brazing

process and a uniform brazed area with good wetting and bonding of both base metals was achieved.

3. Dissolution of the Ni coating layer during the laser brazing process led to the formation of new AlNi IMC phases and also a Mg-Ni eutectic zone along the interface. The AlNi intermetallic layers at the steel-FZ interface formed in the sequence of diamond shaped, dendritic, and nodules from the bottom to the top portion of the joint. These experimental results have confirmed the thermochemical predictions.
4. The formation of a nano-scale Fe(Ni) transition layer on the steel by solid-state interdiffusion between Fe and Ni during laser brazing was found to be responsible for the formation of a metallurgical bond between the steel and the Mg-Al brazing alloy.
5. Formation of Fe(Ni) along the interface led to formation of interfaces with calculated minimum interplanar mismatches of 1% $_{\{Mg\text{-}Fe(Ni)\}}$-4.4% $_{\{Fe(Ni)\text{-}Fe\}}$, thereby improving such properties as the interfacial strength and the bond strength.
6. The average fracture load of 5 mm wide transverse tensile shear specimens taken from the joints reached 1506.3±24.5 N, representing 56.5% joint efficiency with respect to the base metal of AZ31B Mg alloy and 94.8% higher than that of laser brazed joint using Al-12Si interlayer. Fracture surface analysis showed that fracture occurred in the FZ close to the steel-FZ interface.

8.1.3 Laser Brazing of AZ31B to Sn Electro-Plated Steel Sheet

1. It has been shown that diode laser brazing can be successfully performed between 2 mm thick AZ31B-H24 Mg alloy sheet and 0.6 mm thick Sn-coated plain carbon steel sheet in the lap joint configuration using a Mg-Al-Zn brazing alloy wire. Visually acceptable braze joints were produced using 2.2 kW diode laser beam power moving at 8 mm/s travel speed along the joint.
2. In all cases, tensile shear tests failed in the steel sheet indicating that the Mg-Al-Zn brazing alloy-to-steel sheet interface and braze joint were always stronger than the steel sheet.

3. At the steel surface, there was no evidence of the Sn-coating. There was instead a thin layer of Fe(Al) which exhibited a band of Kirkendall porosity. This porosity is known to be caused by the large differences in intrinsic diffusion coefficients in Fe-Al diffusion couples. A nano-scale layer of $Al_8(Mn,Fe)_5$ intermetallic was also observed to have grown on the surface of the Fe(Al) layer.
4. HR-TEM analysis of the Fe(Al)-Al_8Mn_5-Mg interfaces showed that a crystallographic orientation relationship with low angle rotation of the matching planes and low interplanar mismatch existed at the Fe(Al)-Al_8Mn_5 interface, *i.e.*, $\{110\}_{Fe(Al)}$ 4.2° from $\{30\bar{3}3\}_{Al_8Mn_5}$ with 5.2 % interplanar mismatch. These results were further confirmed by the predictions of an edge-to-edge crystallographic matching model of the Fe(Al)-Al_8Mn_5 and Al_8Mn_5-Mg interfaces. These conditions will result in an interface with low interfacial energy densities, good wetting and strong bonds between the phases.
5. The Sn coating on the steel sheet does not appear to contribute to the final bonding of the steel to the AZ92 filler alloy. Instead, its primary role is to prevent contamination and oxidation of the steel surface until molten Mg-Al-Zn brazing alloy can come into direct contact with the steel surface.

As a general conclusion, when Al-12Si was used as the interlayer between steel and magnesium during laser brazing process, despite low interfacial strength of the Mg-$FeAl_3$ interface, the low fracture toughness (brittleness) of $FeAl_3$ reaction product dictated the fracture of the joint, resulted in a low joint efficiency. Therefore, using Al-12Si interlayer for joining steel sheet to magnesium sheet is not recommended. Using Ni and Sn interlayers, which led to formation of the Fe(Ni) and Al_8Mn_5-Fe(Al) reaction products along the α-Mg-Fe interface, respectively, resulted in formation of strong interfaces with low mismatch strain energy and strong bonds. Therefore, using both Ni and Sn interlayers are recommended for dissimilar joining of steel sheet to magnesium sheet.

8.1.4 Wetting Mechanism of Ni-plated steel by molten magnesium alloy

Reactions between molten Mg alloy and Ni electro-plated steel led to the reduction of contact angle from 86º in the temperature range of 618-750 ºC (Mode I) to only 46º in the temperature range of 824-1020 ºC (Mode II) and improvement of the wetting. In Mode I, formation of AlNi and Mg_2Ni reaction products along the Mg-Ni interface with the measured interplanar mismatches of 17% $_{\{Mg\text{-}AlNi\}}$-104.3% $_{\{AlNi\text{-}Mg2Ni\}}$-114% $_{\{Mg2Ni\text{-}Ni\}}$ were observed. In comparison, in Mode II, AlNi was the only formed reaction product along the Mg-Fe interface with the measured interplanar mismatches of 18% $_{\{Mg\text{-}AlNi\}}$-5% $_{\{AlNi\text{-}Fe\}}$. Also, the calculated minimum interplanar mismatches using the edge-to-edge matching model were 16.4% $_{\{Mg\text{-}AlNi\}}$-108.3% $_{\{AlNi\text{-}Mg2Ni\}}$-17.2% $_{\{Mg2Ni\text{-}Ni\}}$ for Mode I and 16.4% $_{\{Mg\text{-}AlNi\}}$-0.6% $_{\{AlNi\text{-}Fe\}}$ for Mode II. Therefore, the results presented in this study confirmed that formation of Mg_2Ni reaction product between AlNi and Ni substrate produced a large lattice mismatch between interfaces which results in an increase in the interfacial strain energy of the system and therefore deteriorates the wetting. It follows from this finding that the lattice mismatching at the interfaces between reaction product(s) and substrate, which are not in direct contact with liquid phase, can greatly influence the wetting of the liquid.

8.2 Outlook

The following topics are suggested for future research:

1. The presented results in this study indicated that a low melting point temperature interlayer, such as Sn, can provide the condition for formation of a strong metallurgical bond in between steel and Mg alloy, just by maintaining a clean, oxide-free steel surface until the molten Mg filler alloy could come in direct contact with the steel surface. As a new interlayer element, Zn may also show similar behaviour due to the low melting and boiling point temperatures, 420 ºC and 907 ºC, respectively. To confirm this new role of the interlayer element, laser brazing of AZ31B-Mg alloy to Zn electro-plated steel sheet is suggested.

2. Prediction of early stage phase formation in the steel-Ni-Mg alloy system during laser brazing was detailed in the current thesis. Using the same method, thermochemical analysis of phases formed at the interface of a Mg alloy-Sn plated steel joint during laser brazing using FactSage thermochemical software is suggested.

3. Laser brazing experiments confirmed good wetting of the Sn electro-plated steel substrate by the Mg alloy (the average contact angle of the fusion zone on the steel substrate was measured to be $35.5^{o} \pm 5^{o}$). It is suggested that further quantitative studies be carried out to enhance the understanding of the effect of interfacial reactions on wettability of Sn electro-plated steel by molten magnesium alloy.

4. Although the current thesis discovers and details the effect of lattice mismatching on wettability of Ni-plated steel by molten magnesium alloy in inherent non-equilibrium thermodynamic conditions, performing the wetting experiments in a controlled-atmosphere furnace and measuring the contact angles of AZ92 Mg alloy on Ni electro-plated steel as a function of time and temperature in fully isothermal conditions can provide very valuable insight into the relation between the interfacial reaction(s) and wettability. Further study on the effect of interfacial reaction on wettability of Ni-plated steel by molten magnesium alloy in isothermal conditions is recommended.

Appendix A
Lattice Matching Calculations Using the Edge-to-Edge Model

To further study the interatomic spacing misfit along matching directions and the interplanar spacing mismatch between matching planes for the different interfaces, the edge-to-edge crystallographic model developed by Zhang and Kelly [85,86] was used. In this matching model, the matching directions and matching planes are the close or nearly close-packed directions and planes [85,86]. The interatomic misfit and interplanar mismatch between two phases were calculated using Equation 4.1. The calculation procedure and the results of the interatomic spacing misfits along matching directions and interplanar spacing mismatches between matching planes for different formed interfaces in this study are given in this Appendix. Table A-1 shows the close-packed directions and planes together with their interatomic or interplanar spacings as a function of lattice parameters for HCP, FCC and BCC crystal structures.

Table A-1: The most close-packed directions and planes and their interatomic and interplanar spacings for HCP, FCC, and BCC crystal structures

Crystal Structure	Close-Packed Direction	Interatomic Spacing	Close-Packed Plane	Interplanar Spacing
HCP (a_H, c_H)*	$<11\bar{2}0>$	a_H	{0002}	$c_H/2$
	$<10\bar{1}0>$	$0.5a_H\sqrt{3}$	$\{10\bar{1}1\}$	$\frac{a_H c_H \sqrt{3}}{\sqrt{4c_H^2+3a_H^2}}$
	$<11\bar{2}3>$	$0.5\left(a_H{}^2+c_H{}^2\right)^{0.5}$	$\{10\bar{1}0\}$	$\sqrt{3}a_H/2$
FCC (a_F)*	$<110>$	$\sqrt{2}/2\ a_F$	{111}	$\sqrt{3}/3\ a_F$
	$<100>$	a_F	{110}	$\sqrt{2}/2\ a_F$
	$<111>$	$\sqrt{3}a_F$	{100}	a_F
BCC (a_B)*	$<111>$	$\sqrt{3}/2\ a_B$	{110}	$\sqrt{2}/2\ a_B$
	$<100>$	a_B	{200}	$0.5a_B$
	$<110>$	$\sqrt{2}a_B$	{111}	$\sqrt{3}/3\ a_B$
	$<113>$	$0.25\sqrt{11}a_B$		

* Lattice Parameters

A.1 Al-12Si Interlayer

A.1.1 Mg (HCP)-$FeAl_3$ (Monoclinic)

According to the edge-to-edge model [85,86], in order to predict the lattice matching between Mg with Hexagonal close-packed (HCP) crystal structure and the $FeAl_3$ phase with monoclinic crystal structure, the close-packed or nearly close-packed planes must be identified. Due to the complexity of the $FeAl_3$ crystal structure, we were not able to identify its close-packed or nearly close-packed directions. The closest-packed planes can be identified by calculation of structure factors or by looking at the powder X-ray diffraction intensities available from the pulished XRD databases [85,86]. The biggest structure factor or the highest intensity of the X-ray diffraction corresponds to the closest-packed plane. The closest-packed planes of $FeAl_3$ with monoclinic crystal structure were identified by looking at the powder X-ray diffraction intensities, which are $\{332\}_{FeAl_3}$, $\{025\}_{FeAl_3}$ and $\{620\}_{FeAl_3}$. The interplanar spacing along (*hkl*) planes (*d*) can be expressed in terms of the monoclinic lattice parameters, a_m, b_m, c_m, and β [112] using the equation:

$$\frac{1}{d^2} = \frac{1}{Sin^2\beta}\left(\frac{h^2}{a_m^2} + \frac{k^2 Sin^2\beta}{b_m^2} + \frac{l^2}{c_m^2} - \frac{2hlCos\beta}{a_m c_m}\right) \qquad \text{(A.1)}$$

Using $FeAl_3$ lattice parameters (a_m = 1.5489 nm b_m = 0.80831 nm, c_m = 1.2476 nm and β = 107.72º [115]), the *d*-values between adjacent $\{332\}_{FeAl_3}$, $\{025\}_{FeAl_3}$ and $\{620\}_{FeAl_3}$ planes were calculated.

In the HCP crystal structure, there are three close-packed or nearly close-packed planes (see Table A-1) [85,86]. Thus, there are a total of nine possible plane pairs between Mg (HCP) and $FeAl_3$ (monoclinic) that are potential matching planes. The variation of interplanar spacing mismatch along the nine possible close-packed or nearly close-packed plane pairs between Mg phase and $FeAl_3$ substrate with the lattice parameters of a_H, c_H, and a_m, b_m, c_m, β for the HCP and monoclinic structures, respectively, were calculated (see Table A-2). The lattice parameters of Mg used in the current study are a_{Mg} = 0.320 nm and c_{Mg} = 0.520 nm [115].

Table A-2: Calculated interplanar spacing for α-Mg and $FeAl_3$ substrate and interplanar spacing mismatch between possible matching planes of Mg and $FeAl_3$

Matching Planes	Mg Interplanar Spacing, nm	$FeAl_3$ Interplanar Spacing, nm	Interplanar Mismatch (%)
$\{0002\}_{Mg} // \{332\}_{FeAl_3}$	0.260	0.209	24.4
$\{10\bar{1}1\}_{Mg} // \{332\}_{FeAl_3}$	0.244	0.209	16.7
$\{10\bar{1}0\}_{Mg} // \{332\}_{FeAl_3}$	0.277	0.209	32.5
$\{0002\}_{Mg} // \{025\}_{FeAl_3}$	0.260	0.205	26.8
$\{10\bar{1}1\}_{Mg} // \{025\}_{FeAl_3}$	0.244	0.205	19.0
$\{10\bar{1}0\}_{Mg} // \{025\}_{FeAl_3}$	0.277	0.205	35.1
$\{0002\}_{Mg} // \{620\}_{FeAl_3}$	0.260	0.210	23.8
$\{10\bar{1}1\}_{Mg} // \{620\}_{FeAl_3}$	0.244	0.210	16.2
$\{10\bar{1}0\}_{Mg} // \{620\}_{FeAl_3}$	0.277	0.210	31.9

To form an orientation relationship, the edge-to-edge matching model requires a critical interplanar spacing mismatch value (*d*-value) between matching planes. It has been reported that the approximate critical *d*-value mismatch is less than 6 %, which is based on reported ORs in known systems [113]. Using 6 % as the approximate critical *d*-value mismatch to form an orientation relationship with low mismatch strain, the calculated data reported in Table A-2 show that all the close-packed or nearly close-packed plane pairs of Mg and $FeAl_3$ are out of this range. Therefore, no plane pair was found to be potential matching planes with an OR with low strain energy to form a metallurgical bond between the two phases. As a result, an interface with high interfacial energy and low bond strength forms in between the Mg and $FeAl_3$ phases. However, tensile shear test of the laser brazed joints showed that the brittle nature of $FeAl_3$ phase dictated the bond strength rather than Mg-$FeAl_3$ interfacial strength [69].

A.1.2 $FeAl_3$ (Monoclinic)-Fe (BCC) Interface

Similar to the Mg-$FeAl_3$ interface, for the other side of the interface, in which $FeAl_3$ is in contact with the Fe ($FeAl_3$–Fe interface), the same crystallographic matching model was applied. In the BCC crystal structure, there are three close-packed or nearly close-packed planes (see Table A-1) [85,86]. Thus, there are a total of nine possible plane pairs between $FeAl_3$ (monoclinic) and Fe (BCC) as the potential matching planes. Table A-3 shows the calculated interplanar spacing for the $FeAl_3$ phase and Fe substrate and interplanar spacing mismatches. The lattice parameter of Fe used in the current study is a_{Fe} = 0.286 nm [115].

Table A-3: Calculated interplanar spacing for $FeAl_3$ phase and Fe substrate and interplanar spacing mismatch between possible matching planes of $FeAl_3$ and Fe

Matching Planes	$FeAl_3$ Interplanar Spacing, nm	Fe Interplanar Spacing, nm	Interplanar Mismatch (%)
$\{332\}_{FeAl_3} // \{110\}_{Fe}$	0.209	0.202	3.5
$\{025\}_{FeAl_3} // \{110\}_{Fe}$	0.205	0.202	1.5
$\{620\}_{FeAl_3} // \{110\}_{Fe}$	0.210	0.202	4.0
$\{332\}_{FeAl_3} // \{200\}_{Fe}$	0.209	0.143	46.1
$\{025\}_{FeAl_3} // \{200\}_{Fe}$	0.205	0.143	43.3
$\{620\}_{FeAl_3} // \{200\}_{Fe}$	0.210	0.143	46.8
$\{332\}_{FeAl_3} // \{111\}_{Fe}$	0.209	0.165	26.7
$\{025\}_{FeAl_3} // \{111\}_{Fe}$	0.205	0.165	24.2
$\{620\}_{FeAl_3} // \{111\}_{Fe}$	0.210	0.165	27.3

If 6 % is used as the critical data of the *d*-value mismatch to form an OR [113], the calculated data reported in Table A-3 show that there are three plane pairs with the interplanar spacing mismatch less than the critical value of 6 %; $\{332\}_{FeAl_3} // \{110\}_{Fe}$, $\{025\}_{FeAl_3} // \{110\}_{Fe}$, and $\{620\}_{FeAl_3} // \{110\}_{Fe}$. Therefore, the $FeAl_3$ phase has very low *d*-value mismatches between the matching planes with Fe, which leads to a low strain energy at their interface and strong metallurgical bond.

A.2 Ni Interlayer (Laser Brazing Process)

A.2.1 Mg (HCP)-Fe(Ni) (FCC) Interface

To study the lattice matching along the Mg-Fe(Ni) interface, the close-packed or nearly close-packed atom rows in each of two phases, together with the relatively close-packed or nearly close-packed planes were identified. For the HCP and FCC crystal structures, there are three close-packed or nearly close-packed directions (see Table A-1). Therefore, there are a total of nine possible matching direction pairs between Mg (HCP) and Fe(Ni) (FCC). With this assumption that the Fe(Ni) is the parent phase (substrate), and Mg is solidified on the Fe(Ni), the variation of interatomic spacing misfit along these nine direction pairs using the parameters of a_H, c_H, and a_F for each direction pairs can be calculated (see Table A-4). The lattice parameter used in the current study is $a_{Fe(Ni)}$ = 0.365 nm [115].

Table A-4: Interatomic spacing misfits along possible matching directions between Mg phase and Fe(Ni) substrate

Matching Directions	Mg Interatomic Spacing, nm	Fe(Ni) Interatomic Spacing, nm	Interatomic Misfit (%)
$<11\bar{2}0>_{Mg}//<110>_{Fe(Ni)}$	0.320	0.258	24.0
$<11\bar{2}0>_{Mg}//<100>_{Fe(Ni)}$	0.320	0.365	12.3
$<11\bar{2}0>_{Mg}//<111>_{Fe(Ni)}$	0.320	0.632	49.4
$<10\bar{1}0>_{Mg}//<110>_{Fe(Ni)}$	0.277	0.258	7.4
$<10\bar{1}0>_{Mg}//<100>_{Fe(Ni)}$	0.277	0.365	24.1
$<10\bar{1}0>_{Mg}//<111>_{Fe(Ni)}$	0.277	0.632	56.2
$<11\bar{2}3>_{Mg}//<110>_{Fe(Ni)}$	0.305	0.258	18.2
$<11\bar{2}3>_{Mg}//<100>_{Fe(Ni)}$	0.305	0.365	16.4
$<11\bar{2}3>_{Mg}//<111>_{Fe(Ni)}$	0.305	0.632	51.7

Table A-4 shows that the potential matching directions with the interatomic spacing misfit less than the critical value of 10 % is along $<10\bar{1}0>_{Mg\ //}<110>_{Fe(Ni)}$ between the Mg and the Fe(Ni) phase. The selection of 10 % as the critical value for the interatomic spacing misfit is based on van der Merwe's energy calculation, which was done along the close-packed directions between FCC and Body Centered Cubic (BCC) [85,86,114].

Once the matching directions are defined, the interplanar mismatches between the possible matching planes need to be identified. There are nine possible plane pairs between HCP and FCC crystal structures. Table A-5 shows the calculated results for the interplanar spacing mismatches along possible matching planes between Mg and Fe(Ni). If 6 % is used as the critical data of the *d*-value mismatch [85,86], then the plane pairs of $\{0002\}_{Mg\ //}$ $\{110\}_{Fe(Ni)}$ and $\{10\bar{1}1\}_{Mg\ //}\{110\}_{Fe(Ni)}$ have the potential to be the matching planes to form an OR with low mismatch strain. Therefore, the contribution of the strain energy to the total Mg-Fe(Ni) interfacial energy is low.This leads to a strong metallurgical bond at Mg-Fe(Ni) interface.

Table A-5: Calculated interplanar spacing for Mg and Fe(Ni) substrate and interplanar spacing mismatch between possible matching planes of Mg and Fe(Ni)

Matching Planes	Mg Interplanar Spacing, nm	Fe(Ni) Interplanar Spacing, nm	Interplanar Mismatch (%)
$\{0002\}_{Mg}//\{111\}_{Fe(Ni)}$	0.260	0.211	23.2
$\{0002\}_{Mg}//\{110\}_{Fe(Ni)}$	0.260	0.258	1.0
$\{0002\}_{Mg}//\{100\}_{Fe(Ni)}$	0.260	0.365	28.8
$\{10\bar{1}1\}_{Mg}//\{111\}_{Fe(Ni)}$	0.244	0.211	15.6
$\{10\bar{1}1\}_{Mg}//\{110\}_{Fe(Ni)}$	0.244	0.258	5.4
$\{10\bar{1}1\}_{Mg}//\{100\}_{Fe(Ni)}$	0.244	0.365	33.1
$\{10\bar{1}0\}_{Mg}//\{111\}_{Fe(Ni)}$	0.277	0.211	31.3
$\{10\bar{1}0\}_{Mg}//\{110\}_{Fe(Ni)}$	0.277	0.258	7.4
$\{10\bar{1}0\}_{Mg}//\{100\}_{Fe(Ni)}$	0.277	0.365	24.1

A.2.2 Fe(Ni) (FCC)-Fe (BCC) Interface

Analysis of the Mg-Fe(Ni) interface confirmed good lattice matching at the interface. For the other side of the interface (Fe(Ni)-Fe), the same procedure was adapted. For the BCC crystal structure, there are four close-packed or nearly close-packed directions (see Table A-1). Therefore, there are a total of twelve possible matching direction pairs between Fe(Ni) (FCC) and Fe (BCC). The calculated interatomic spacing for Fe(Ni) phase and Fe and interatomic misfits along possible matching directions between them are shown in Table A-6.

Table A-6: Interatomic spacing misfits along possible matching directions between Fe(Ni) phase and Fe

Matching Directions	Fe(Ni) Interatomic Spacing, nm	Fe Interatomic Spacing, nm	Interatomic Misfit (%)
$<110>_{Fe(Ni)}//<111>_{Fe}$	0.258	0.248	4.0
$<100>_{Fe(Ni)}//<111>_{Fe}$	0.365	0.248	47.2
$<111>_{Fe(Ni)}//<111>_{Fe}$	0.632	0.248	154.8
$<110>_{Fe(Ni)}//<100>_{Fe}$	0.258	0.286	9.8
$<100>_{Fe(Ni)}//<100>_{Fe}$	0.365	0.286	27.6
$<111>_{Fe(Ni)}//<100>_{Fe}$	0.632	0.286	121.0
$<110>_{Fe(Ni)}//<110>_{Fe}$	0.258	0.404	36.1
$<100>_{Fe(Ni)}//<110>_{Fe}$	0.365	0.404	9.6
$<111>_{Fe(Ni)}//<110>_{Fe}$	0.632	0.404	56.4
$<110>_{Fe(Ni)}//<113>_{Fe}$	0.258	0.237	8.9
$<100>_{Fe(Ni)}//<113>_{Fe}$	0.365	0.237	54.0
$<111>_{Fe(Ni)}//<113>_{Fe}$	0.632	0.237	166.7

Table A-6 shows that the potential matching directions with the interatomic spacing misfit less than the critical value of 10 % are along $<110>_{Fe(Ni)}//<111>_{Fe}$, $<110>_{Fe(Ni)}//<100>_{Fe}$, $<100>_{Fe(Ni)}//<110>_{Fe}$, and $<110>_{Fe(Ni)}//<113>_{Fe}$ between the Fe(Ni) phase and Fe at the interface.

Identification of matching planes is the next step. Table A-7 shows that there are nine possible plane pairs between Fe(Ni) and Fe as the potential matching plane pairs. The only plane pair with the interplanar mismatch less than the critical value of 6 % is $\{111\}_{Fe(Ni)}//\{110\}_{Fe}$. Existence of this pair confirms that the Fe(Ni)-Fe interface can form a low energy interface and a strong bond.

Table A-7: Calculated interplanar spacing for Fe(Ni) phase and Fe substrate and interplanar spacing mismatch between possible matching planes of Fe(Ni) and Fe

Matching Planes	Fe(Ni) Interplanar Spacing, nm	Fe Interplanar Spacing, nm	Interplanar Mismatch (%)
$\{111\}_{Fe(Ni)} // \{110\}_{Fe}$	0.211	0.202	4.4
$\{110\}_{Fe(Ni)} // \{110\}_{Fe}$	0.258	0.202	27.7
$\{100\}_{Fe(Ni)} // \{110\}_{Fe}$	0.365	0.202	80.7
$\{111\}_{Fe(Ni)} // \{200\}_{Fe}$	0.211	0.143	47.5
$\{110\}_{Fe(Ni)} // \{200\}_{Fe}$	0.258	0.143	80.4
$\{100\}_{Fe(Ni)} // \{200\}_{Fe}$	0.365	0.143	155.2
$\{111\}_{Fe(Ni)} // \{111\}_{Fe}$	0.211	0.165	27.9
$\{110\}_{Fe(Ni)} // \{111\}_{Fe}$	0.258	0.165	56.4
$\{100\}_{Fe(Ni)} // \{111\}_{Fe}$	0.365	0.165	121.2

A.3 Sn Interlayer

A.3.1 Mg (HCP)-Al_8Mn_5 (Rhombohedral)

$Al_8(Mn,Fe)_5$ is a substitutional solid solution of Al_8Mn_5, in which some Mn atoms are replaced by Fe. Solution of the Fe atoms into Al_8Mn_5 and replacement of the Mn atoms by Fe atoms do not cause significant variation in the lattice parameters, since the atomic radius of Mn and Fe are very close (0.112 nm and 0.124 nm, respectively) [115]. Therefore, $Al_8(Mn,Fe)_5$ can be treated as Al_8Mn_5 with Al_8Cr_5 type of rhombohedral structure. In this case, the lattice parameters for Al_8Mn_5 are a = 1.2645 nm and c = 1.5855 nm [115].

The unit cell of Al_8Mn_5 (or $Al_8(Mn,Fe)_5$) contains 48 Al atoms and 30 Mn/Fe atoms. From these atoms' positions in the unit cell of Al_8Mn_5 together with the X-ray diffraction intensity data [45], the close-packed or nearly close-packed planes of $Al_8(Mn,Fe)_5$ were identified to be $\{30\bar{3}3\}_{Al_8Mn_5}$ and $\{33\bar{6}0\}_{Al_8Mn_5}$. Similarly, the close-packed or nearly close-packed directions are $\langle 11\bar{2}0\rangle_{Al_8Mn_5}$, $\langle 0001\rangle_{Al_8Mn_5}$, $\langle 1\bar{1}02\rangle_{Al_8Mn_5}$, and $\langle 10\bar{1}1\rangle_{Al_8Mn_5}$ [45].

If it is assumed that during cooling, the Mg (HCP) nucleates and grows onto the pre-existing Al_8Mn_5 surface layer, the variation of interatomic spacing misfit along twelve possible close-packed or nearly close-packed directions pairs and also the variation of interplanar spacing mismatch along six possible close-packed or nearly close-packed plane pairs between Mg phase and Al_8Mn_5 substrate can be calculated (see Tables A-8 and A-9). If 10 % is selected as the critical value of the interatomic spacing misfit, then three direction pairs satisfy this condition; $<10\bar{1}0>_{Mg}//<1\bar{1}02>_{Al_8Mn_5}$, $<11\bar{2}3>_{Mg}//<1\bar{1}02>_{Al_8Mn_5}$ and $<10\bar{1}0>_{Mg}//<10\bar{1}1>_{Al_8Mn_5}$.

Table A-8: Interatomic spacing misfits along possible matching directions between Mg phase and Al_8Mn_5 substrate

Matching Directions	Mg Interatomic Spacing, nm	Al_8Mn_5 Interatomic Spacing, nm	Interatomic Misfit (%)
$<11\bar{2}0>_{Mg}//<11\bar{2}0>_{Al_8Mn_5}$	0.320	0.244	31.1
$<10\bar{1}0>_{Mg}//<11\bar{2}0>_{Al_8Mn_5}$	0.277	0.244	13.5
$<11\bar{2}3>_{Mg}//<11\bar{2}0>_{Al_8Mn_5}$	0.305	0.244	25.0
$<11\bar{2}0>_{Mg}//<1\bar{1}02>_{Al_8Mn_5}$	0.320	0.289	10.7
$<10\bar{1}0>_{Mg}//<1\bar{1}02>_{Al_8Mn_5}$	0.277	0.289	4.2
$<11\bar{2}3>_{Mg}//<1\bar{1}02>_{Al_8Mn_5}$	0.305	0.289	5.5
$<11\bar{2}0>_{Mg}//<0001>_{Al_8Mn_5}$	0.320	0.401	20.2
$<10\bar{1}0>_{Mg}//<0001>_{Al_8Mn_5}$	0.277	0.401	30.9
$<11\bar{2}3>_{Mg}//<0001>_{Al_8Mn_5}$	0.305	0.401	23.9
$<11\bar{2}0>_{Mg}//<10\bar{1}1>_{Al_8Mn_5}$	0.320	0.264	21.1
$<10\bar{1}0>_{Mg}//<10\bar{1}1>_{Al_8Mn_5}$	0.277	0.264	4.9
$<11\bar{2}3>_{Mg}//<10\bar{1}1>_{Al_8Mn_5}$	0.305	0.264	15.5

Again, if 6 % is used as the critical data of the *d*-value mismatch [85,86], all the close-packed or nearly close-packed plane pairs of Mg and Al_8Mn_5 are predicted to be outside of this range.

Table A-9: Calculated interplanar spacing for Mg phase and Al_8Mn_5 substrate and interplanar spacing mismatch between possible matching planes of Mg and Al_8Mn_5

Matching Planes	Mg Interplanar Spacing, nm	Al_8Mn_5 Interplanar Spacing, nm	Interplanar Mismatch (%)
$\{0002\}_{Mg} // \{30\bar{3}3\}_{Al_8Mn_5}$	0.260	0.221	17.6
$\{10\bar{1}1\}_{Mg} // \{30\bar{3}3\}_{Al_8Mn_5}$	0.244	0.221	10.4
$\{10\bar{1}0\}_{Mg} // \{30\bar{3}3\}_{Al_8Mn_5}$	0.277	0.221	25.3
$\{0002\}_{Mg} // \{33\bar{6}0\}_{Al_8Mn_5}$	0. 260	0.217	19.8
$\{10\bar{1}1\}_{Mg} // \{33\bar{6}0\}_{Al_8Mn_5}$	0.244	0.217	12.4
$\{10\bar{1}0\}_{Mg} // \{33\bar{6}0\}_{Al_8Mn_5}$	0. 277	0.217	27.6

It was reported by Zhang *et al*. [45] that the metastable τ-AlMn phase possesses significantly better crystallographic matching with the Mg matrix than the other Al-Mn intermetallic phases, such as $Al_8(Mn,Fe)_5$ phase. In another study, Emley [14] reported that Fe-containing intermetallic compounds may be inoculant particles for Mg grains. Also, Byun *et al*. [116] studied the effect of different Mn addition levels on the microstructure of the AZ91 alloy and proposed that $Al_8(Mn,Fe)_5$ particles behaved as effective nucleation sites [116]. Tiner [117] also confirmed that Mg-Al alloy containing 0.19 % up to 0.98 % Mn exhibited grain refinement. Grain refinement of AZ31 alloys by Al_8Mn_5 particles was also reported by Laser *et al*. [118] and Xiao *et al*. [107], even though Qui *et al*. [119] reported that Al_8Mn_5 has a high atomic mismatch energy against α-Mg. Kim *et al*. [99] reported that the

addition of 0.3 wt.% Mn into Mg-9 wt.% Al alloy leaded to a dramatic grain refinement from 340 μm to 87 μm, resulting from the formation of $Al_8(Mn,Fe)_5$.

A.3.2 Al_8Mn_5 (Rhombohedral)-Fe(Al) (BCC)

The lattice parameter of Fe(Al) used in this study was $a_{Fe(Al)}$ = 0.2885 nm (measured from the SADP of Fe(Al) phase in Figure 6-5b). There are sixteen direction pairs between Al_8Mn_5 (rhombohedral) and Fe(Al) (BCC) as the potential matching directions. If we assumed that the Fe(Al) phase is the substrate and Al_8Mn_5 is the reaction product on the Fe(Al), the variation of interatomic spacing misfit along these direction pairs can be calculated. Table A-10 shows the calculated results for the relative interatomic spacing misfits along possible matching directions between Al_8Mn_5 and Fe(Al).

According to the data shown in Table A-10, the matching directions with interatomic spacing misfits less than the critical value of 10 % between the Fe(Al) substrate and Al_8Mn_5 phase at the interface are: $<11\bar{2}0>_{Al_8Mn_5}//<111>_{Fe(Al)}$, $<10\bar{1}1>_{Al_8Mn_5}//<111>_{Fe(Al)}$, $<1\bar{1}02>_{Al_8Mn_5}//<100>_{Fe(Al)}$, $<10\bar{1}1>_{Al_8Mn_5}<100>_{Fe(Al)}//$, $<0001>_{Al_8Mn_5}<110>_{Fe(Al)}//$, and $<11\bar{2}0>_{Al_8Mn_5}//<113>_{Fe(Al)}$.

Table A-10: Interatomic spacing misfits along possible matching directions between Al_8Mn_5 phase and Fe(Al) substrate

Matching Directions	Al_8Mn_5 Interatomic Spacing, nm	Fe(Al) Interatomic Spacing, nm	Interatomic Misfit (%)
$<11\bar{2}0>_{Al_8Mn_5} // <111>_{Fe(Al)}$	0.244	0.250	2.4
$<1\bar{1}02>_{Al_8Mn_5} // <111>_{Fe(Al)}$	0.289	0.250	15.6
$<0001>_{Al_8Mn_5} // <111>_{Fe(Al)}$	0.401	0.250	60.4
$<10\bar{1}1>_{Al_8Mn_5} // <111>_{Fe(Al)}$	0.264	0.250	3.3
$<11\bar{2}0>_{Al_8Mn_5} // <100>_{Fe(Al)}$	0.244	0.288	15.3
$<1\bar{1}02>_{Al_8Mn_5} // <100>_{Fe(Al)}$	0.289	0.288	0.3
$<0001>_{Al_8Mn_5} // <100>_{Fe(Al)}$	0.401	0.288	39.2
$<10\bar{1}1>_{Al_8Mn_5} // <100>_{Fe(Al)}$	0.264	0.288	8.3
$<11\bar{2}0>_{Al_8Mn_5} // <110>_{Fe(Al)}$	0.244	0.408	40.2
$<1\bar{1}02>_{Al_8Mn_5} // <110>_{Fe(Al)}$	0.289	0.408	29.2
$<0001>_{Al_8Mn_5} // <110>_{Fe(Al)}$	0.401	0.408	1.7
$<10\bar{1}1>_{Al_8Mn_5} // <110>_{Fe(Al)}$	0.264	0.408	35.3
$<11\bar{2}0>_{Al_8Mn_5} // <113>_{Fe(Al)}$	0.244	0.239	2.1
$<1\bar{1}02>_{Al_8Mn_5} // <113>_{Fe(Al)}$	0.289	0.239	20.9
$<0001>_{Al_8Mn_5} // <113>_{Fe(Al)}$	0.401	0.239	67.8
$<10\bar{1}1>_{Al_8Mn_5} // <113>_{Fe(Al)}$	0.264	0.239	10.5

Table A-11 shows the calculated interplanar spacing for Al_8Mn_5 phase and Fe(Al) substrate and interplanar spacing mismatches. Using 6 % as the approximate critical *d*-value mismatch [85,86], calculated data reported in Table A-11 indicate that there are two plane pairs with the interplanar spacing mismatch close to the critical value of 6 %; $\{30\bar{3}3\}_{Al_8Mn_5} // \{110\}_{Fe(Al)}$ and $\{33\bar{6}0\}_{Al_8Mn_5} // \{110\}_{Fe(Al)}$. The HR-TEM experimental results in this study also

showed that the OR at the interface between the Al_8Mn_5 and Fe(Al) was $\{30\bar{3}3\}_{Al_8Mn_5}$ // $\{110\}_{Fe(Al)}$ with 1.3 % interplanar mismatch between them (see Figure 6-6a). This is in good agreement with the predictions of the edge-to-edge model. Both results suggest that the Fe(Al) phase has quite small interatomic spacing misfits along the matching direction and very low *d*-value mismatches between the matching planes with Al_8Mn_5 phase. These conditions lead to low interfacial mismatch strain energy and a strong interface.

Table A-11: Calculated interplanar spacing for Al_8Mn_5 phase and Fe(Al) substrate and interplanar spacing mismatch between possible matching planes of Al_8Mn_5 and Fe(Al)

Matching Planes	Al_8Mn_5 Interplanar Spacing, nm	Fe(Al) Interplanar Spacing, nm	Interplanar Mismatch (%)
$\{30\bar{3}3\}_{Al_8Mn_5}$ // $\{110\}_{Fe(Al)}$	0.221	0.204	8.3
$\{33\bar{6}0\}_{Al_8Mn_5}$ // $\{110\}_{Fe(Al)}$	0.217	0.204	6.3
$\{30\bar{3}3\}_{Al_8Mn_5}$ // $\{200\}_{Fe(Al)}$	0.221	0.144	53.5
$\{33\bar{6}0\}_{Al_8Mn_5}$ // $\{200\}_{Fe(Al)}$	0. 217	0.144	50.7
$\{30\bar{3}3\}_{Al_8Mn_5}$ // $\{111\}_{Fe(Al)}$	0.221	0.166	33.1
$\{33\bar{6}0\}_{Al_8Mn_5}$ // $\{111\}_{Fe(Al)}$	0. 217	0.166	30.7

A.4 Ni Interlayer (Wetting Experiment)

A.4.1 Mg (HCP)-AlNi (BCC) Interface (Modes I & II)

There are a total of twelve possible matching direction pairs between HCP and BCC. Table A-12 shows the calculated interatomic spacings for Mg and AlNi and interatomic misfits along possible matching directions between them. The lattice parameter used in the current study is a_B = 0.288 nm for AlNi [110]. The calculated results (Table A-12) indicate that if 10 % is selected as the critical value of the interatomic spacing misfit, three direction

pairs satisfy this condition, which are $<11\bar{2}0>_{Mg}//<100>_{AlNi}$, $<10\bar{1}0>_{Mg}//<100>_{AlNi}$, and $<11\bar{2}3>_{Mg}//<100>_{AlNi}$.

Table A-12: Interatomic spacing misfits along possible matching directions between Mg and AlNi

Matching Directions	Mg Interatomic Spacing, nm	AlNi Interatomic Spacing, nm	Interatomic Misfit (%)
$<11\bar{2}0>_{Mg}//<111>_{AlNi}$	0.320	0.249	22.2
$<10\bar{1}0>_{Mg}//<111>_{AlNi}$	0.277	0.249	10.1
$<11\bar{2}3>_{Mg}//<111>_{AlNi}$	0.305	0.249	18.4
$<11\bar{2}0>_{Mg}//<100>_{AlNi}$	0.320	0.288	10.0
$<10\bar{1}0>_{Mg}//<100>_{AlNi}$	0.277	0.288	4.0
$<11\bar{2}3>_{Mg}//<100>_{AlNi}$	0.305	0.288	5.6
$<11\bar{2}0>_{Mg}//<110>_{AlNi}$	0.320	0.407	27.2
$<10\bar{1}0>_{Mg}//<110>_{AlNi}$	0.277	0.407	46.9
$<11\bar{2}3>_{Mg}//<110>_{AlNi}$	0.305	0.407	33.4
$<11\bar{2}0>_{Mg}//<113>_{AlNi}$	0.320	0.239	25.3
$<10\bar{1}0>_{Mg}//<113>_{AlNi}$	0.277	0.239	13.7
$<11\bar{2}3>_{Mg}//<113>_{AlNi}$	0.305	0.239	21.6

Identification of matching planes is the next step. Table A-13 shows the calculated results for the interplanar spacing mismatches along possible matching planes between Mg and AlNi. Using 6 % as the critical value, it can be concluded that there are no potential matching planes between Mg and AlNi with an OR with low strain energy (see Table A-13).

As a result, an interface with high interfacial energy and low bond strength forms in between the Mg and AlNi phase.

Table A-13: Calculated interplanar spacing for Mg and AlNi and interplanar spacing mismatch between possible matching planes of Mg and AlNi

Matching Planes	Mg Interplanar Spacing, nm	AlNi Interplanar Spacing, nm	Interplanar Mismatch (%)
$\{0002\}_{Mg} // \{110\}_{AlNi}$	0.260	0.204	21.5
$\{10\bar{1}1\}_{Mg} // \{110\}_{AlNi}$	0.244	0.204	16.4
$\{10\bar{1}0\}_{Mg} // \{110\}_{AlNi}$	0.277	0.204	26.3
$\{0002\}_{Mg} // \{200\}_{AlNi}$	0.260	0.144	44.6
$\{10\bar{1}1\}_{Mg} // \{200\}_{AlNi}$	0.244	0.144	41.0
$\{10\bar{1}0\}_{Mg} // \{200\}_{AlNi}$	0.277	0.144	48.0
$\{0002\}_{Mg} // \{111\}_{AlNi}$	0.260	0.166	36.1
$\{10\bar{1}1\}_{Mg} // \{111\}_{AlNi}$	0.244	0.166	32.0
$\{10\bar{1}0\}_{Mg} // \{111\}_{AlNi}$	0.277	0.166	40.1

A.4.2 AlNi (BCC)-Mg_2Ni (HCP) Interface (Mode I)

The lattice parameters used in the current study are a_H = 0.518 nm and c_H = 1.319 nm for Mg_2Ni [110]. Table A-14 shows the calculated results for the relative interatomic spacing misfits along possible matching directions between AlNi and Mg_2Ni. Table A-15 shows the calculated interplanar spacings for AlNi and Mg_2Ni and interplanar spacing mismatches. No potential matching direction was found between AlNi and Mg_2Ni with δ less than the critical value of 10 % (see Table A-14). Also, there are no potential matching planes between AlNi and Mg_2Ni with interplanar spacing mismatch less than the critical value of 6 % (see

Table A-15). Therefore, similar to the Mg-AlNi interface, an interface with high interfacial energy and low bond strength forms in between the AlNi and Mg_2Ni phases.

Table A-14: Interatomic spacing misfits along possible matching directions between AlNi and Mg_2Ni

Matching Directions	AlNi Interatomic Spacing, nm	Mg_2Ni Interatomic Spacing, nm	Interatomic Misfit (%)
$<111>_{AlNi} // <11\bar{2}0>_{Mg_2Ni}$	0.249	0.518	108.0
$<111>_{AlNi} // <10\bar{1}0>_{Mg_2Ni}$	0.249	0.449	80.3
$<111>_{AlNi} // <11\bar{2}3>_{Mg_2Ni}$	0.249	0.622	149.8
$<100>_{AlNi} // <11\bar{2}0>_{Mg_2Ni}$	0.288	0.518	79.9
$<100>_{AlNi} // <10\bar{1}0>_{Mg_2Ni}$	0.288	0.449	55.9
$<100>_{AlNi} // <11\bar{2}3>_{Mg_2Ni}$	0.288	0.622	116.0
$<110>_{AlNi} // <11\bar{2}0>_{Mg_2Ni}$	0.407	0.518	27.3
$<110>_{AlNi} // <10\bar{1}0>_{Mg_2Ni}$	0.407	0.449	10.3
$<110>_{AlNi} // <11\bar{2}3>_{Mg_2Ni}$	0.407	0.622	52.8
$<113>_{AlNi} // <11\bar{2}0>_{Mg_2Ni}$	0.239	0.518	116.7
$<113>_{AlNi} // <10\bar{1}0>_{Mg_2Ni}$	0.239	0.449	87.9
$<113>_{AlNi} // <11\bar{2}3>_{Mg_2Ni}$	0.239	0.622	160.2

Table A-15: Calculated interplanar spacing for AlNi and Mg_2Ni and interplanar spacing mismatch between possible matching planes of AlNi and Mg_2Ni

Matching Planes	AlNi Interplanar Spacing, nm	Mg_2Ni Interplanar Spacing, nm	Interplanar Mismatch (%)
$\{110\}_{AlNi} // \{0002\}_{Mg_2Ni}$	0.204	0.659	223.0
$\{110\}_{AlNi} // \{10\bar{1}1\}_{Mg_2Ni}$	0.204	0.425	108.3
$\{110\}_{AlNi} // \{10\bar{1}0\}_{Mg_2Ni}$	0.204	0.449	120.1
$\{200\}_{AlNi} // \{0002\}_{Mg_2Ni}$	0.144	0.659	357.6
$\{200\}_{AlNi} // \{10\bar{1}1\}_{Mg_2Ni}$	0.144	0.425	195.1
$\{200\}_{AlNi} // \{10\bar{1}0\}_{Mg_2Ni}$	0.144	0.449	211.8
$\{111\}_{AlNi} // \{0002\}_{Mg_2Ni}$	0.166	0.659	297.0
$\{111\}_{AlNi} // \{10\bar{1}1\}_{Mg_2Ni}$	0.166	0.425	156.0
$\{111\}_{AlNi} // \{10\bar{1}0\}_{Mg_2Ni}$	0.166	0.449	170.5

A.4.3 Mg_2Ni (HCP)-Ni (FCC) Interface (Mode I)

With the assumption that the Ni (FCC) is the parent phase (substrate), and Mg_2Ni phase (HCP) is formed on the substrate as the product, Table A-16 shows the calculated interatomic spacings for Mg_2Ni and Ni and interatomic misfits along possible matching directions between them (a_F = 0.352 nm for Ni [110]). Calculated results show that the only potential matching directions with the interatomic spacing misfit less than the critical value of 10 % is along $<11\bar{2}3>_{Mg_2Ni} // <111>_{Ni}$ between the Ni electro-plated layer and the Mg_2Ni phase at the interface. Table A-17 shows the calculated results for the interplanar spacing mismatches between possible matching planes between Mg_2Ni phase and Ni. Using 6 % as the critical value, it can be concluded that there are no potential matching planes between Mg_2Ni and Ni to form a low energy interface (see Table A-17).

Table A-16: Interatomic spacing misfits along possible matching directions between Mg_2Ni phase and Ni substrate

Matching Directions	Mg_2Ni Interatomic Spacing, nm	Ni Interatomic Spacing, nm	Interatomic Misfit (%)
$<11\bar{2}0>_{Mg_2Ni} // <110>_{Ni}$	0.518	0.249	51.9
$<11\bar{2}0>_{Mg_2Ni} // <100>_{Ni}$	0.518	0.352	32.0
$<11\bar{2}0>_{Mg_2Ni} // <111>_{Ni}$	0.518	0.610	17.8
$<10\bar{1}0>_{Mg_2Ni} // <110>_{Ni}$	0.449	0.249	44.5
$<10\bar{1}0>_{Mg_2Ni} // <100>_{Ni}$	0.449	0.352	21.6
$<10\bar{1}0>_{Mg_2Ni} // <111>_{Ni}$	0.449	0.610	35.8
$<11\bar{2}3>_{Mg_2Ni} // <110>_{Ni}$	0.622	0.249	60.0
$<11\bar{2}3>_{Mg_2Ni} // <100>_{Ni}$	0.622	0.352	43.4
$<11\bar{2}3>_{Mg_2Ni} // <111>_{Ni}$	0.622	0.610	1.9

Table A-17: Calculated interplanar spacing for Mg_2Ni phase and Ni substrate and interplanar spacing mismatch between possible matching planes of Mg_2Ni and Ni

Matching Planes	Mg_2Ni Interplanar Spacing, nm	Ni Interplanar Spacing, nm	Interplanar Mismatch (%)
$\{0002\}_{Mg_2Ni} // \{111\}_{Ni}$	0.659	0.203	69.2
$\{0002\}_{Mg_2Ni} // \{110\}_{Ni}$	0.659	0.249	62.2
$\{0002\}_{Mg_2Ni} // \{100\}_{Ni}$	0.659	0.352	46.6
$\{10\bar{1}1\}_{Mg_2Ni} // \{111\}_{Ni}$	0.425	0.203	52.2
$\{10\bar{1}1\}_{Mg_2Ni} // \{110\}_{Ni}$	0.425	0.249	41.4
$\{10\bar{1}1\}_{Mg_2Ni} // \{100\}_{Ni}$	0.425	0.352	17.2
$\{10\bar{1}0\}_{Mg_2Ni} // \{111\}_{Ni}$	0.449	0.203	54.8
$\{10\bar{1}0\}_{Mg_2Ni} // \{110\}_{Ni}$	0.449	0.249	44.5
$\{10\bar{1}0\}_{Mg_2Ni} // \{100\}_{Ni}$	0.449	0.352	21.6

A.4.4 AlNi (BCC)-Fe (BCC) Interface (Mode II)

With the assumption that the Fe is the substrate and AlNi is the formed phase (product), Table A-18 and Table A-19 show the calculated results for the relative interatomic spacing misfits and interplanar spacing mismatches between Fe and AlNi, respectively. The interatomic spacing misfits less than the critical value of 10 % between the AlNi phase and Fe substrate at the interface were found along $<111>_{AlNi} // <111>_{Fe}$, $<113>_{AlNi} // <111>_{Fe}$, $<100>_{AlNi} // <100>_{Fe}$, $<110>_{AlNi} // <110>_{Fe}$, $<111>_{AlNi} // <113>_{Fe}$ and $<113>_{AlNi} // <113>_{Fe}$ (see Table A-18). Also, the interplanar spacing mismatches less than the critical value of 6 % are for $\{110\}_{Fe} // \{110\}_{AlNi}$, $\{200\}_{Fe} // \{200\}_{AlNi}$, and $\{111\}_{Fe} // \{111\}_{AlNi}$ (see Table A-19). These conditions lead to low interfacial mismatch strain energy and a strong AlNi-Fe interface.

Table A-18: Interatomic spacing misfits along possible matching directions between AlNi phase and Fe substrate

Matching Directions	AlNi Interatomic Spacing, nm	Fe Interatomic Spacing, nm	Interatomic Misfit (%)
$<111>_{AlNi}//<111>_{Fe}$	0.249	0.248	0.4
$<100>_{AlNi}//<111>_{Fe}$	0.288	0.248	13.9
$<110>_{AlNi}//<111>_{Fe}$	0.407	0.248	39.1
$<113>_{AlNi}//<111>_{Fe}$	0.239	0.248	3.3
$<111>_{AlNi}//<100>_{Fe}$	0.249	0.286	14.8
$<100>_{AlNi}//<100>_{Fe}$	0.288	0.286	0.7
$<110>_{AlNi}//<100>_{Fe}$	0.407	0.286	29.7
$<113>_{AlNi}//<100>_{Fe}$	0.239	0.286	19.7
$<111>_{AlNi}//<110>_{Fe}$	0.249	0.404	62.2
$<100>_{AlNi}//<110>_{Fe}$	0.288	0.404	40.3
$<110>_{AlNi}//<110>_{Fe}$	0.407	0.404	0.7
$<113>_{AlNi}//<110>_{Fe}$	0.239	0.404	69.0
$<111>_{AlNi}//<113>_{Fe}$	0.249	0.237	4.8
$<100>_{AlNi}//<113>_{Fe}$	0.288	0.237	17.7
$<110>_{AlNi}//<113>_{Fe}$	0.407	0.237	41.8
$<113>_{AlNi}//<113>_{Fe}$	0.239	0.237	0.8

Table A-19: Calculated interplanar spacing for AlNi phase and Fe substrate and interplanar spacing mismatch between possible matching planes of AlNi and Fe

Matching Planes	AlNi Interplanar Spacing, nm	Fe Interplanar Spacing, nm	Interplanar Mismatch (%)
$\{110\}_{AlNi} // \{110\}_{Fe}$	0.204	0.202	1.0
$\{200\}_{AlNi} // \{110\}_{Fe}$	0.144	0.202	40.3
$\{111\}_{AlNi} // \{110\}_{Fe}$	0.166	0.202	21.7
$\{110\}_{AlNi} // \{200\}_{Fe}$	0.204	0.143	29.9
$\{200\}_{AlNi} // \{200\}_{Fe}$	0.144	0.143	0.7
$\{111\}_{AlNi} // \{200\}_{Fe}$	0.166	0.143	13.8
$\{110\}_{AlNi} // \{111\}_{Fe}$	0.204	0.165	19.1
$\{200\}_{AlNi} // \{111\}_{Fe}$	0.144	0.165	14.6
$\{111\}_{AlNi} // \{111\}_{Fe}$	0.166	0.165	0.6

REFERENCES

[1] G.S. Cole, "Issues that influence magnesium's use in the automotive industry", *Materials Science Forum*, 2003, vol. 419-422, pp. 43-50.

[2] H. Watarai, "Trend of Research and Development for Magnesium Alloys-Reducing the Weight of Structural Materials in Motor Vehicles", *Science & Technology Trends-Quarterly Review*, Jan. 2006, no.18, pp. 84-97.

[3] B. Bronfin and N. Moscovitch, "New magnesium alloys for transmission parts", *Metal Science and Heat Treatment*, 2006, vol. 48, no. 11, pp. 479-486.

[4] S. Jana and S. Hovanski, "Fatigue behaviour of magnesium to steel dissimilar friction stir lap joints", *Science and Technology of Welding and Joining*, 2012, vol. 17, no. 2, pp. 141-145.

[5] J. Yan, Z. Xu , Z. Li, L. Li, and S. Yang, "Microstructure characteristics and performance of dissimilar welds between magnesium alloy and aluminum formed by friction stirring", *Scripta Materialia*, 2005, vol. 53, pp. 585-589.

[6] H.K. Mao and P.M. Bell, "Equations of state of MgO and Fe under static pressure conditions", *Journal of Geophysical Research*, 1979, pp. 4533-4536.

[7] L.M. Liu and X. Zhao, "Study on the weld joint of Mg alloy and steel by laser-GTA hybrid welding", *Materials Characterization*, 2008, vol. 59, pp. 1279-1284.

[8] W. Takehiko, K. Kazuhiko, and Y.G. Ronbunshul, "Solid state welding of steel and magnesium alloy using a rotating pin", *Quaterly Journal of the Japan Welding Society*, 2006, pp. 108-115.

[9] Y. Miao, D. Han, J. Yao, and F. Li, "Microstructure and interface characteristics of laser penetration brazed magnesium alloy and steel", *Science and Technology of Welding and Joining*, 2010, vol. 15, no. 2, pp. 97-103.

[10] L. Lockwood and A.E. Shapiro, "Brazing of magnesium", In *Brazing Handbook, 5th Edition*, 2005, AWS, Miami.

[11] G. Sierra, P. Peyre, F. Deschaux Beaume, D. Stuart, and G. Fras, "Steel to aluminum braze welding by laser process with Al-12Si filler wire", *Science and Technology of Welding and Joining*, 2008, vol. 13, no. 5, pp. 430-437.

[12] M. Kreimeyer, F. Wagner, and F. Vollertsen, "Laser processing of aluminum-titanium-tailored blanks", *Optics and Lasers in Engineering*, 2005, vol. 43, pp. 1021-1035.

[13] H.E. Friedrich and B.L. Mordike, "*Magnesium technology: metallurgy, design data, applications*", 2006, Springer-Verlag Berlin Heidelberg.

[14] E.F. Emley, "*Principles of Magnesium Technology*", Ed. 1, 1966, Pergamon Press, p. 200, 231.

[15] A. Beck, "*Magnesium and its alloy*", 1939, Springer-Verlag Berlin.

[16] R.S. Busk, "*Magnesium Products Design*", 1987, Marcel Dekker Inc., New York.

[17] H. Haferkamp, M. von Alvensleben, M. Goede, and J. Niemeyer, "Fatigue strength of laser beam welded magnesium alloys", 32 ISATA, International Symposium on Automotive Technology and Automation: Advances in Automotive and Transportation Technology and Practice for the 21st Century, Vienna, Austria, 14–18 June 1999, pp. 389–397.

[18] H. Zhao, D.R. White, and T. DebRoy, "Current issues and problems in laser welding of automotive aluminum alloys", *International Materials Review*, 1999, vol. 44, no. 6, pp. 238–266.

[19] K.G. Watkins, in: H.I. Kaplan (Ed.), "Laser Welding of Magnesium Alloys, Magnesium Technology 2003", TMS Annual Meeting and Exhibition, San Diego, CA, 2–6 March 2003, pp. 153–156.

[20] Y.F. Shein, "Brazing of magnesium alloys", in Brazing Reference Book, 2nd Edition, Editors: I.E. Petrunin and S.N. Lotsmanov, Moscow, 1984, p. 320.

[21] D. Sakkinen, "Magnesium alloy metallurgy", in Automotive materials at the SAE Show, *Advanced Materials and Processes*, 1995, vol. 5, pp. 26-27.

[22] G. Foerster, "A new approach to magnesium die casting", *Advanced Materials and Processes*, 1995, vol. 10, pp. 79-81.

[23] N. Masuda, T. Ishikawa, Y. Miyadzawa, T. Ariga, and H. Matsumami, "Brazing of magnesium alloys", *DVS-Berichte*, 2001, vol. 212, pp. 353-355.

[24] P. Bakke, K. Pettersen, and D. Albright, "The influence of Sb, Si, and Sn on mechanical properties of Mg-Al alloys", *Magnesium Technology 2004*, ed. By A.A. Luo, 2005, TMS, pp. 289-296.

[25] M.M. Schwartz, "*Brazing*", 1987, ASM International, Metals Park, Ohio, pp. 4-10.

[26] T. Watanabe, S. Komatsu, and K. Oohara, “Development of Flux and Filler Metal for Brazing Magnesium Alloy AZ31B”, *Welding Journal,* 2005, vol. 84, no. 3, pp. 37-40.

[27] Y.C. Chen and K. Nakata, “Effect of tool geometry on microstructure and mechanical properties of friction stir lap welded magnesium alloy and steel”, *Materials & Design*, 2009, vol. 30, pp. 3913–3919.

[28] Y.C. Chen and K. Nakata, “Effect of surface states of steel on microstructure and mechanical properties of lap joints of magnesium alloy and steel by friction stir welding”, *Science and Technology of Welding and Joining,* 2010, vol. 15, no. 4, pp. 293-298.

[29] S. Jana, Y. Hovanski, and G.J. Grant, “Friction stir welding of magnesium alloy to steel: a preliminary investigation”, *Metallurgical and Materials Transaction A*, 2010, vol. 41(A), pp. 3173-3182.

[30] W.M. Thomas, E.D. Nicholas, J.C. Needham, M.G. Murch, P. Templesmith, and C.J. Dawes, GB Patent Application No. 9125978.8, Dec. 1991.

[31] R.K. Saha, T.I. Khan, “Microstructural developments in TLP bonds using thin interlayers based on Ni–B coatings”, *Materials Characterization,* 2009, vol. 60, pp. 1001–1007.

[32] R.K. Saha and T.I. Khan, “Effect of bonding temperature on transient liquid phase bonding behavior of a Ni-based oxide dispersion-strengthened superalloy”, *Journal of Materials Engineering and Performance,* 2006, vol. 15, pp. 722–728.

[33] W.M. Elthalabawy, T. I. Khan, “Microstructural development of diffusion-brazed austenitic stainless steel to magnesium alloy using a nickel interlayer”, *Materials Characterization*, 2010, vol. 61, pp. 703–712.

[34] L.M. Liu and X. Qi, “Effects of copper addition on microstructure and strength of the hybrid laser-TIG welded joints between magnesium alloy and mild steel”, *Journal of Materials Science,* 2009, vol. 44, pp. 5725–5731.

[35] L.M. Liu, X. Qi, and Z. Wu, “Microstructural characteristics of lap joint between magnesium alloy and mild steel with and without the addition of Sn element”, *Materials Letter*, 2010, vol. 64, pp. 89–92.

[36] X. Qi and G. Song, “Interfacial structure of the joints between magnesium alloy and mild steel with nickel as interlayer by hybrid laser-TIG welding”, *Materials & Design,* 2010, vol. 31, pp. 605–609.

[37] L. Liu and X. Qi, "Strengthening effect of nickel and copper interlayers on hybrid laser-TIG welded joints between magnesium alloy and mild steel", *Materials & Design*, 2010, vol. 31, pp. 3960–3963.

[38] M. Wahba and S. Katayama, "Laser welding of AZ31B magnesium alloy to Zn-coated steel", *Materials & Design*, 2012, vol. 35, pp. 701-706.

[39] L. Liu, L. Xiao, J.C. Feng, Y.H. Tian, S.Q. Zhou, and Y. Zhou, "The Mechanisms of Resistance Spot Welding of Magnesium to Steel", *Metallurgical and Materials Transaction A*, 2012, vol. 41(A), pp. 2651-2661.

[40] H. Fredriksson and U. Akerlind, "*Solidification and Crystallization Processing in Metals and Alloys*", 2012, John Wiley & Sons Ltd., United Kingdom, pp. 141-144, 180-184.

[41] M.C. Liu, J.C. Huang, Y.T. Fong, S.P. Ju, X.H. Du, H.J. Pei, and T.G. Nieh, "Assessing the interfacial strength of an amorphous–crystalline interface", *Acta Materialia*, 2013, vol. 61, no. 9, pp. 3304-3313.

[42] Y. Mishin, M. Asta, J. Li, "Atomistic modeling of interfaces and their impact on microstructure and properties", *Acta Materialia*, 2010, vol. 58, pp. 1117–1151.

[43] M.E. Glicksman, "*Principles of Solidification*", Springer Science+Business Media, LLC 2011, DOI: 10.1007/978-1-4419-7344-3_12, p. 294.

[44] L. Liu, L. Xiao, J. Feng, L. Li, S. Esmaeili, and Y. Zhou, "Bonding of immiscible Mg and Fe by coated nanoscale Fe_2Al_5 transition layer", *Scripta Materialia*, 2011, vol. 65, no. 11, pp. 982-985.

[45] M.X. Zhang, P.M. Kelly, M. Qian, and J.A. Taylor, "Crystallography of grain refinement in Mg-Al based alloys", *Acta Materialia*, 2005, vol. 53, pp. 3261-3270.

[46] G. Bailey and H. Watkins, "The flow of liquid metals on solid metal surfaces and its relation to soldering, brazing, and hot-dip casting", *Journal of Institute of Metals*, 1952, vol. 80, p. 57.

[47] D.R. Frear, W.B. Jones, and K.R. Kinsman, "Solder mechanics-a state of the art assessment", *ATMS Publication*, 1991, pp. 1-104.

[48] G. Kumar and K.N. Prabhu, "Review of non-reactive and reactive wetting of liquids on surfaces", *Advances in Colloid and Interface Science*, 2007, vol. 133, pp. 61-89.

[49] A. Mortensen, B. Drevet, and N. Eustathopoulos, "Kinetics of diffusion-limited spreading of sessile drops in reactive wetting", *Scripta Materialia*, 1997, vol. 36, no. 6, pp. 645–651.

[50] N. Eustathopoulos, "Dynamics of wetting in reactive metal/ceramic systems", *Acta Materialia*, 1998, vol. 46, no. 7, pp. 2319–2327.

[51] K. Landry and N. Eustathopoulos, "Dynamics of wetting in reactive metal/ceramic systems: linear spreading", *Acta Materialia*, 1996, vol. 44, no. 10, pp. 3923–3932.

[52] B. Drevet, K. Landry, P. Vikner, and N. Eustathopoulos, "Influence of substrate orientation on wetting kinetics in reactive metal/ceramic systems", *Scripta Materialia*, 1996, vol. 35, no. 11, pp. 1265–1270.

[53] N. Eustathopoulos, "Progress in understanding and modeling reactive wetting of metals on ceramics", *Current Opinion in Solid State and Materials Science*, 2005, vol. 9, no. 5, pp. 152–160.

[54] E. Saiz, C.W. Hwang, K. Suganuma, and A.P. Tomsia, "Spreading of Sn-Ag solders on FeNi alloys", *Acta Materialia*, 2003, vol. 51, no. 11, pp. 3185-3197.

[55] K.K. Wang, L. Chang, D. Gan, and H.P. Wang, "Heteroepitaxial growth of Fe_2Al_5 inhibition layer in hot-dip galvanizing of an interstitial-free steel", *Thin Solid Films*, 2010, vol. 518, pp. 1935-1942.

[56] C.W. Bale, E. Bélisle, P. Chartrand, S.A. Decterov, G. Eriksson, K. Hack, I.H. Jung, Y.B. Kang, J. Melançon, A.D. Pelton, C. Robelin, and S. Petersen, "FactSage thermochemical software and databases - recent developments", *CALPHAD*, 2009, vol. 33, pp. 295-311.

[57] N. Saunders, X. Li, A.P. Miodownik, and J.P. Schille, in: J.C. Zhao, M. Fahrmann, and T. Pollock (Eds.): *"Computer Modelling of Materials Properties", TMS, Warrendale, PA*, 2001, pp. 185-197.

[58] R.H. Davies, A.T. Dinsdale, J.A. Gisby, J.A.J. Robinson, and S.M. Martin, "Coupling of Phase Diagrams and Thermochemistry", *CALPHAD*, 2002, vol. 26, pp. 229-271.

[59] S.L. Chen, S. Daniel, F. Zhang, Y.A. Chang, X.Y. Yan, F.Y. Xie, R. Schmid Fetzer, and W.A. Oates, "The PANDAT software package and its applications", *CALPHAD*, 2002, vol. 26, pp. 175-188.

[60] L.M. Liu, *Welding and Joining of Magnesium Alloys*, Woodhead Publishing Limited, 2010, pp. 63-78.

[61] J.A. Warren, W.J. Boettinger, and A.R. Roosen, "Modeling Reactive Wetting", *Acta Materialia*, 1998, vol. 46, pp. 3247-3264.

[62] N. Eustathopoulos, M.G. Nicholas, B. Drevet, "*Wettability at High Temperatures*", Pergamon Materials Series, Oxford, 1999, 3, p. 187, 202, 399.

[63] Material Safety Data Sheet, 2003, Superior Flux & Mfg. Co, November 11, p. 1.

[64] K. Saida, W. Song, and K. Nishimoto, "Diode laser brazing of aluminum alloy to steels with aluminum filler metal", *Science and Technology of Welding and Joining*, 2005, vol. 10, no. 2, pp. 227-235.

[65] G.F. Vander Voort, "*Metallography Principles and Practice*", 1999, Materials Park. OH. ASM International.

[66] T.M. Moore, "Microscopy Today", 2005, vol. 13, no. 4, p. 40.

[67] R. Voitovitch, A. Mortensen, and N. Eustathopoulos, "Diffusion-limited reactive wetting: study of spreading kinetics of Cu–Cr alloys on carbon substrates", *Acta Materialia*, 1999, vol. 47, no. 4, pp. 1117-1128.

[68] O. Dezellus, F. Hodaj, and N. Eustathopoulos, "Chemical reaction-limited spreading: the triple line velocity versus contact angle relation", *Acta Materialia*, 2002, vol. 47, p. 4741.

[69] **A.M. Nasiri**, L. Li, S.H. Kim, Y. Zhou, D.C. Weckman, and T.C. Nguyen, "Microstructure and Properties of Laser Brazed Magnesium to Coated Steel", *Welding Journal*, 2011, vol. 11, pp. 211-219.

[70] ASM Metals Handbook, "*Properties and Selection: Nonferrous Alloys and Special Purpose Materials*", 1990, 10th ed., vol. 2, Materials Park, OH: ASM International.

[71] A.K. Dahle, Y.C. Lee, M.D. Nave, P.L. Schafer, and D.H. StJohn, "Development of the as-cast microstructure in magnesium-aluminium alloys", *Journal of Light Metals*, 2001, vol. 1, pp. 61-72.

[72] S. Barbagallo, H.I. Laukli, O. Lohne, and E. Cerri, "Divorced eutectic in a HPDC magnesium–aluminum alloy", *Journal of Alloys and Compounds*, 2004, vol. 378, pp. 226-232.

[73] A. Mathieu, S. Pontevicci, J. Viala, E. Cicala, S. Matte, and D. Grevey, "Laser brazing of a steel/aluminium assembly with hot filler wire (88% Al, 12% Si)", *Materials Science and Engineering A*, 2006, vol. 435, pp. 19-28.

[74] Y. Li, P. Ochin, A. Quivy, P. Telolahy, and B. Legendre, "Enthalpy of formation of Al-Fe-Si alloys (τ_5, τ_{10}, τ_1, τ_9)", *Journal of Alloys and Compounds*, 2000, vol. 298, pp. 198-202.

[75] T. Maitra and S.P. Gupta, "Intermetallic compound formation in Fe-Al-Si ternary system: Part II", *Materials Characterization*, 2003, vol. 49, pp. 293-311.

[76] Y. Li and B. Legendre, "Enthalpy of formation of Al-Fe-Si alloys II (τ_6, τ_2, τ_3, τ_8, τ_4)", *Journal of Alloys and Compounds*, 2000, vol. 302, pp. 187-191.

[77] Y.Y. Chang, W.J. Cheng, and C.J. Wang, "Growth and surface morphology of hot-dip Al-Si on 9Cr-1Mo steel", *Materials Characterization*, 2009, vol. 60, pp. 144-159.

[78] P. Peyre, G. Sierra, F.D. Deschaux-Beaume, D. Stuart, and G. Fras, "Generation of aluminum-steel joints with laser-induced reactive wetting", *Materials Science and Engineering A*, 2007, vol. 444, pp. 327-338.

[79] K. Bouche, F. Barbier, and A. Coulet, "Intermetallic compound layer growth between solid iron and molten aluminium", *Materials Science and Engineering A*, 1998, vol. 249, pp. 167-175.

[80] J.C. Viala, M. Peronnet, F. Barbeau, F. Bosselet, and J. Bouix, "Interface chemistry in aluminium alloy castings reinforced with iron base inserts", *Composites Part A*, 2002, vol. 33, pp. 1417-1420.

[81] M. Roulin, J.W. Luster, G. Karadeniz, and A. Mortensen, "Strength and structure of furnace-brazed joints between aluminum and stainless steel", *Welding Journal*, 1999, vol. 78, pp. 151-155.

[82] Y. Miao, D. Han, J. Yao, and F. Li, "Effect of laser offsets on joint performance of laser penetration brazing for magnesium alloy and steel", *Materials & Design*, 2010, vol. 31, pp. 3121-3126.

[83] S.B. Lin, J.L. Song, C.L. Yang, C.L. Fan, and D.W. Zhang, "Brazability of dissimilar metals tungsten inert gas butt welding-brazing between aluminum alloy and stainless steel with Al-Cu filler metal", *Materials & Design*, 2010, vol. 31, pp. 2637-2642.

[84] M.J. Rathod and M. Kutsuna, "Joining of aluminum alloy 5052 and low-carbon steel by laser roll welding", *Welding Journal*, 2004, pp. 16-26.

[85] M.X. Zhang and P.M. Kelly, "Edge-to-edge matching and its applications Part I. Application to the simple HCP/BCC system", *Acta Materialia*, 2005, vol. 53, pp. 1073-1084.

[86] M.X. Zhang and P.M. Kelly, "Edge-to-edge matching and its applications: Part II. Application to Mg–Al, Mg–Y and Mg–Mn alloys", *Acta Materialia*, 2005, vol. 53, pp. 1085-1096.

[87] **A.M. Nasiri**, P. Chartrand, D.C. Weckman, and Y. Zhou, "Thermochemical Analysis of Phases Formed at the Interface of a Mg alloy-Ni plated Steel Joint during Laser Brazing", *Metallurgical and Materials Transaction A*, 2013, vol. 44, no. 4, pp. 1937-1946.

[88] **A.M. Nasiri**, D.C. Weckman, and Y. Zhou, "Interfacial Microstructure of Diode Laser Brazed AZ31B Magnesium to Steel Sheet Using a Nickel Interlayer", *Welding Journal*, 2013, vol. 92, no. 1, pp. 1-10.

[89] D.R. Gaskell, "*Introduction to Metallurgical Thermodynamics*", 2nd ed., Hemisphere Publishing Corp., New York, 1981.

[90] N.A. Belov, D.G. Eskin, and N.N. Avxentieva, "Constituent phase diagrams of the Al-Cu-Fe-Mg-Ni-Si system and their application to the analysis of aluminum piston alloys", *Acta Materialia*, 2005, vol. 53, pp. 4709-4722.

[91] J.O. Andersson, T. Helander, L. Hogland, P. Shi, and B. Sundman, "Thermo-Calc and DICTRA, Computational Tools for Materials Science", *CALPHAD*, 2002, vol. 26, pp. 273-312.

[92] M.C. Flemings, "*Solidification Processing*", 1974, McGill-Hill Inc., p. 296.

[93] F. Weinberg and B. Chalmers, "Further observations on dendritic growth in metals", *Canadian Journal of Physics*, 1952, vol. 30, pp. 488-502.

[94] **A.M. Nasiri**, D.C. Weckman, and Y. Zhou, "The Effect of a Sn Interlayer on Brazebility of AZ31B Magnesium to Steel Sheet", Submitted to the *Metallurgical and Materials Transaction A* on June 2013.

[95] ASM Handbook, 10th ed., Vol. 3, Alloy Phase Diagrams, ASM International, Materials Park, OH, 1994.

[96] M. Potesser, T. Schoeberl, H. Antrekowitsch and J. Bruckner, "The Characterization of the Intermetallic Fe-Al Layer of Steel-Aluminum Weldings", EPD Congress, TMS (The Minerals, Metals & Materials Society), 2006.

[97] M. Kogachi and T. Haraguchi, "Quenched-in vacancies in B2-strauctured intermetallic compound FeAl", *Materials Science and Engineering A*, 1997, vol. 230, pp. 124-131.

[98] L. Li, C. Tan, Y. Chen, W. Guo, and F. Song, "Comparative study on microstructure and mechanical properties of laser welded–brazed Mg/mild steel and Mg/stainless steel joints", *Materials & Design*, 2013, vol. 43, pp. 59-65.

[99] Y.M. Kim, C.D. Yim, and B.S. You, "Grain refining mechanism in Mg-Al alloys with carbon addition", *Scripta Materialia*, vol. 57, 2007, pp. 691-694.

[100] L. Xiao, L. Liu, S. Esmaeili and Y. Zhou, "Microstructure refinement after the addition of Titanium particles in the AZ31 Magnesium alloy resistance spot welds", *Metallurgical and Materials Transaction A*, 2012, vol. 43A, no. 2, pp. 598-609.

[101] M. Salamon and H. Mehrer, "Interdiffusion, Kirkendall effect, and Al self-diffusion in iron–aluminium alloys", *Zeitschrift für Metallkunde*, 2005, vol. 96, pp. 4-16.

[102] H. Springer, A. Kostka, J.F. dos Santos, and D. Raabe, "Influence of intermetallic phases and Kirkendall-porosity on the mechanical properties of joints between steel and aluminium alloys", *Materials Science and Engineering A*, 2011, vol. 528, pp. 4630-4642.

[103] G.P. Tiwari and R.S. Mehrotra, "Kirkendall Effect and Mechanism of Self-diffusion in B2 Intermetallic Compounds", *Metallurgical and Materials Transaction A*, 2012, vol. 43A, pp. 3654-3662.

[104] R.J. Borg and G.J. Dienes, "*An Introduction to Solid State Diffusion*", Boston, Academic Press Inc., 1988.

[105] T. Li, J.W. Morris and D.C. Chrzan, "Ideal tensile strength of B2 transition-metal aluminides", *Physical Review B*, 2004, vol. 70, 054107.

[106] M.M. Avedesian and H. Bake, *"Magnesium and Magnesium Alloys"*, eds., 1999, p. 254, 263, ASM International, Materials Park, OH.

[107] L. Xiao, L. Liu, Y. Zhou and S. Esmaeili, "Resistance-Spot-Welded AZ31 Magnesium Alloys: Part I. Dependence of Fusion Zone Microstructures on Second-Phase Particles", *Metallurgical and Materials Transaction A*, 2010, vol. 41A, no. 6, pp. 1511-1522.

[108] **A.M. Nasiri**, D.C. Weckman, and Y. Zhou, "Effects of Interfacial Lattice Mismatching on Wetting of Ni-plated Steel by Magnesium", Submitted to *Acta Materialia* on July 2013.

[109] A. Gasparyan and A. Shteinberg, "Macrokinetics of reaction and thermal explosion in Ni and Al powder mixtures", *Combustion, Explosion, and Shock Waves*, 1988, vol. 24, pp. 324-330.

[110] W.B. Pearson, "*Lattice Spacings and Structures of Metals and Alloys*", Pergamon Press, New York.

[111] E. Abe, Y. Kawamura, K. Hayashi, and A. Inoue, "Long-period ordered structure in a high-strength nanocrystalline Mg-1 at% Zn-2 at% Y alloy studied by atomic-resolution Z-contrast STEM", *Acta Materialia*, 2002, vol. 50, pp. 3845–3857.

[112] B.D. Cullity, "*Elements of X-ray Diffraction*", 2nd Edition, Addison-Wesley Publishing Co. Inc., 1978, p. 501.

[113] D. Duly, "Application of the invariant line model for b.c.c./h.c.p. couples: A criterion based on surface variations", *Acta Metallurgica et Materialia*, 1993, vol. 41, p. 1559.

[114] J.H. van der Merwe, "Analytical selection of ideal epitaxial configurations and some speculations on the occurrence of epitaxy", *Philosophical Magazine A*, 1982, vol. 45, pp. 127–143, 145–157, & 159–170.

[115] P. Villars and L.D. Calvert, "*Pearsons handbook of crystallographic data for intermetallic phases*", vol. 1, Materials Park (OH): ASM International; 1991, p. 676, 932, 913.

[116] J.Y. Byun, S. Kwon, H.P. Ha, and J.K. Yoon, "*Magnesium Alloys and Their Applications*", K.U. Kainer, ed., Wiley-VCH, Weinheim, 2003, p. 713.

[117] N. Tiner, "Superheating of magnesium alloys", *AIME Technical Publication*, 1945, vol. 12, pp. 1–12.

[118] T. Laser, M.R. Nurnberg, A. Janz, Ch. Hartig, D. Letzig, R. Schmid-Fetzer, and R. Bormann, "The influence of manganese on the microstructure and mechanical properties of AZ31 gravity die cast alloys", *Acta Materialia*, 2006, vol. 54, pp. 3033-3041.

[119] D. Qiu, M.X. Zhang, J.A. Taylor, H.M. Fu, and P.M. Kelly, "A novel approach to the mechanism for the grain refining effect of melt superheating of Mg–Al alloys", *Acta Materialia*, 2007, vol. 55, pp. 1863-1871.